# NANO-BIO INTERACTIONS: CELLULAR AND MOLECULAR EFFECTS OF NANOSCALE VANADIUM PENTOXIDE ON MAMMALIAN AND MICROBIAL MODELS

A THESIS PRESENTED BY

**PARVATHY R. S.**

TO

THE SREE CHITRA TIRUNAL INSTITUTE FOR MEDICAL
SCIENCES AND TECHNOLOGY, TRIVANDRUM
THIRUVANANTHAPURAM

IN PARTIAL FULFILMENT OF THE REQUIREMENTS

FOR THE AWARD OF

**DOCTOR OF PHILOSOPHY**

2020

# CERTIFICATE

I, Parvathy R.S., hereby certify that I had personally carried out the work depicted in the thesis entitled, **“NANO-BIO INTERACTIONS: CELLULAR AND MOLECULAR EFFECTS OF NANOSCALE VANADIUM PENTOXIDE ON MAMMALIAN AND MICROBIAL MODELS”.** No part of the thesis has been submitted for the award of any other degree or diploma prior to this date except where due acknowledgment has been made in the text.

Parvathy R.S.
Reg.No:2013/PhD/15

Date: 12.08.2020

Dr. R. S. Jayasree
Division of Biophotonics and Imaging
Department of Biomaterial Sciences and Technology

This is to certify that **Ms. Parvathy R. S.**, in the Division of Biophotonics and Imaging of this Institute, has fulfilled the requirements prescribed for the Ph.D. degree of the Sree Chitra Tirunal Institute for Medical Sciences and Technology, Trivandrum.

The thesis entitled, **"NANO-BIO INTERACTIONS: CELLULAR AND MOLECULAR EFFECTS OF NANOSCALE VANADIUM PENTOXIDE ON MAMMALIAN AND MICROBIAL MODELS"** was carried out under my direct supervision. No part of the thesis was submitted for the award of any degree or diploma prior to this date.

*Clearance was obtained from the Institutional Animal Ethics Committee (IAEC) for carrying out the study. (IAEC approval # SCT/IAEC 243/August/2017/94).

Dr. R.S. Jayasree
Date: 12.08.2020

The thesis entitled

# NANO-BIO INTERACTIONS: CELLULAR AND MOLECULAR EFFECTS OF NANOSCALE VANADIUM PENTOXIDE ON MAMMALIAN AND MICROBIAL MODELS

Submitted by

**PARVATHY R. S.**

for the degree of

**Doctor of Philosophy**

of

SREE CHITRA TIRUNAL INSTITUTE FOR
MEDICAL SCIENCES AND TECHNOLOGY, TRIVANDRUM

Thiruvananthapuram

Is evaluated and approved by

| | |
|---|---|
| .......................... | .................................... |
| Name of the guide | Name of the thesis examiner |

**Dedicated to my Family…**

# ACKNOWLEDGMENTS

*I would like to express my sincere gratitude to my research guide, Dr. R. S. Jayasree, for her continuous support, valuable suggestions, and patience in mentoring during the entire course of my Ph.D. work. I am thankful to her for all the moral support and help that she has given me throughout my days in the laboratory. I owe my sincere gratitude to The Director, SCTIMST, and Head BMT Wing for providing the infrastructural facilities. I extend my thanks to Dean, Associate Dean (Ph.D. affairs), Registrar, Deputy Registrar, and all members of the academic division and Director's office for their support and help. I acknowledge the former and present Head of the Division, for their academic support in carrying out my Ph.D. work. I thank the Indian Council for Medical Research (ICMR), Govt. of India for the Junior Research Fellowship No.3/1/3/JRF-2012/HRD-148 (20037), and the Commonwealth of Australia for the Endeavour Research Fellowship – 2015. I am incredibly thankful to my doctoral advisory committee members, Dr. K Sreenivasan and Dr. Anoopkumar Thekkuveettil, for their suggestions and critical comments in improving my Ph.D. work.*

*I acknowledge Prof. Sheshnath.V.Bhosale (Royal Melbourne Institute of Technology, Australia) for mentoring me during my Endeavour fellowship period in Australia. I thank Dr. Srinivasa Reddy Telukutla, Dr. Chaitali D. Dekiwadia, and Dr. Ravi Shukla of RMIT for supporting my access to the cell culture facility and making me learn the technique of processing cells and imaging them under an electron microscope. I also acknowledge the facilities, the scientific and technical support in electron microscopy provided by Dr. Flame Burgmann, Dr. Matthew Field, and Dr. Edwin Mayes of the RMIT University's Microscopy & Microanalysis Facility, for the EM analysis. In addition, I thank the generous support from the RMIT University's Micro Nano Research Facility for the flow cytometry and confocal imaging facilities. I thank Dr. T. R Santosh Kumar, Dr. Malini Laloraya of Rajiv Gandhi Centre for Biotechnology, for extending their infrastructural facilities for carrying out experiments at their institute. I am also indebted to their team members Dr. Renjini A. Padmanabhan and Mr. Shankar Narayanan Varadarajan, for their help in the process* *of learning and experimenting with real-time PCR, cell transfection, and time-lapse fluorescence imaging. I am obligated to Dr. Srinivasa Murty Srinivasula, School of Biology, Indian Institute of Science Education and Research Thiruvananthapuram, for his wholehearted support, critical evaluation in experiments, and for the infrastructural facilities. His team members Dr. Anoop Kumar G V and Mr. Rishith Ravindran were integral components who helped me in learning and carrying out newer molecular biology techniques. I thank Dr. Masayuki Miura, University of Tokyo, Japan, for gifting the expression vector SCAT3-NLS and Tamotsu Yoshimori for pEGFP-LC3. I thank Dr. Manoj Komath, Dr. Suresh Babu, Mr. Nishad, Ms. Susan Mani, and Dr. Remya K. R of DBST for the TEM and ICP facility. I thank Dr. Roy Joseph and Mr. Willi Paul of DPMD for the Raman analysis. I sincerely thank Dr. M.R. Rekha for the academic support and critical comments that helped me to achieve the objectives of my study. I thank Dr. Maya Nandkumar, Mr. Pradeep, and all staff of DMIT for providing the spectrometer facility for my studies. I thank Dr. Anoopkumar Thekkuveettil and all staff of DMOM for their never-ending support. I sincerely acknowledge Dr. Sachin J Shenoy, Mr. Manoj, and Mr. Sunil, of DLAS for helping me in animal experiments. I am thankful to Dr. Sabareeshwaran and all lab members of Experimental pathology for the histopathology analysis.*

*I cherish every moment that I shared with my former research fellows Dr. Arya Saraswathy, Dr. Shaiju, Dr. Lakshmi, Ms. Madumole Jeevan, Ms. Aneesha Sherine, Mr. Aneesh, Mr. Jayaram, Ms. Dhanya, Ms. Nisha, and Ms. Lakshmi. I also thank all my present lab members Dr. Rekha, Ms. Resmi V Nair, Ms. Hema, Ms. Marina, Mr. Jibin, Ms. Renuka, Ms. Resmi, and Ms. Rinta, for their support in carrying out my Ph.D. work in the division. I also thank all the staff of BMT Wing, who directly or indirectly helped me in completing my Ph.D. program; thanks to the division of accounts, stores & purchase, library and the security staff for their kind support.*

*I am indebted to my loved parents and affectionate brother for their prayers, patience, and support that made my life easy and paved the way for the successful completion of my Ph.D. work. Above all, I thank God Almighty for giving me the strength to stand up and walk again during all the difficult times in my life.*

# Table of Contents

# List of Figures

# List of Tables

# List of abbreviations

| | |
|---|---|
| **ADME** | Adsorption, distribution, metabolism, excretion |
| **ALT** | Alanine transaminase |
| **AO** | Acridine orange |
| **AST** | Aspartate aminotransferase |
| **AST** | Aspartate transaminase |
| **BCA** | Bicinchoninic acid assay |
| **BSA** | Bovine serum albumin |
| **CCP** | Critical control point |
| **cDNA** | Complementary deoxyribonucleic acid |
| **CFU** | Colony forming units |
| **cm** | Centimetre |
| **CPCSEA** | Committee for the purpose of control and supervision of Experiments on Animals |
| **CPM** | Counts per minutes |
| **DAPI** | 4',6-diamidino-2-phenylindole |
| **DCFH-DA** | Dichloro-dihydro-fluorescein diacetate |
| **$dH_2O$** | Deionised water |
| **DLS** | Dynamic light scattering |
| **DMEM** | Dulbecco's modified eagle medium |
| **DMSO** | Dimethyl sulphoxide |
| **DNA** | Deoxyribonucleic acid |
| **ECFP** | Enhanced cyan fluorescent protein |
| **EDS** | Energy dispersive x-ray spectroscopy |
| **EDTA** | Ethylene diamine tetra acetic acid |
| **EU** | Endotoxin unit |
| **eV** | Electron volt |
| **EYFP** | Enhanced yellow fluorescent protein |
| **FACS** | Fluorescence activated cell sorting |
| **FBS** | Foetal Bovine Serum |

| | |
|---|---|
| **FRET** | Fluorescence resonance energy transfer, |
| **FSC** | Forward scatter |
| **FTIR** | Fourier-transform infrared |
| **g** | Gram |
| **GAPDH** | Glyceraldehyde 3-phosphate dehydrogenase |
| **GFP** | Green fluorescence protein |
| **h** | Hour |
| **H & E** | Haematoxylin and eosin |
| **$H_2O_2$** | Hydrogen peroxide |
| **HBSS** | Hanks balanced salt solution |
| **HCT** | Haematocrit |
| **HGB** | Haemoglobin |
| **HR-TEM** | High resolution transmission electron microscope |
| **i.v.** | Intravenous |
| **IAEC** | Institutional Animal Ethics Committee |
| **ICDD** | International centre for diffraction data |
| **ICP-OES** | Inductively coupled plasma optical emission Spectroscopy |
| **IL** | Interleukin |
| **JC10** | 5,5′,6,6′-tetrachloro-1,1′,3,3′-tetraethylbenzimidazolylcarbocyanineiodide |
| **kDa** | Kilo Dalton |
| **kg** | Kilogram |
| **kV** | Kilovolt |
| **LC3** | Microtubule-associated protein 1 light chain 3 |
| **LC50** | Lethal concentration 50 % |
| **LMP** | Lysosomal membrane permeabilisation |
| **M** | Molar |
| **mg** | Milligram |
| **mg/g** | Milligram/gram |
| **min** | Minutes |
| **ml** | Millilitre |

| | |
|---|---|
| **mm** | Millimetre |
| **mM** | Millimolar |
| **MMP** | Mitochondrial membrane potential |
| **MRI** | Magnetic resonance imaging |
| **MTT** | 3-(4,5-Dimethylthiazol-2-yl)-2,5-diphenyltetrazolium bromide |
| **NF-κB** | Nuclear Factor – κB |
| **NLS** | Nuclear localisation signal |
| **NM** | Nanomaterials |
| **nm** | Nanometre |
| **NOAEL** | No observed adverse effect level |
| **$^{o}$C** | Celsius |
| **p53** | Tumor suppression protein p53 |
| **PBS** | Phosphate buffered saline |
| **PDF** | Powder diffraction files |
| **PDI** | Polydispersity index |
| **PFA** | Paraformaldehyde |
| **PI** | Propidium Iodide |
| **PLT** | Platelet |
| **PMSF** | Phenyl methane sulfonyl fluoride |
| **PS** | Phosphatidyl serine |
| **PVDF** | Polyvinylidene difluoride |
| **qPCR** | Quantitative polymerase chain reaction |
| **RBC** | Red blood cell |
| **Rh-phalloidin** | Rhodamine phalloidin |
| **RNA** | Ribonucleic acid |
| **ROI** | Region of interest |
| **ROS** | Reactive oxygen species |
| **Rpm** | Revolutions per minutes |
| **s** | Second |
| **SCAT** | Sensor for activated caspases |
| **SD** | Standard deviation |

| | |
|---|---|
| **SDS** | Sodium dodecyl sulphate |
| **SEM** | Scanning electron microscopy |
| **SOD** | Superoxide dismutase |
| **SSC** | Sideward scatter |
| **TBST** | Tris-Buffered Saline, Tween20 |
| **TEMED** | Tetramethyl ethylenediamine |
| **TGA** | Thermogravimetric analysis |
| **TNF-α** | Tumour necrosis factor-α |
| **UT** | Untreated |
| **V** | Volt |
| **v/v** | Volume/Volume |
| **Vn** | Nano-vanadium |
| **VnNp** | Vanadium pentoxide nanoplate |
| **VnNs** | Vanadium pentoxide nanosphere |
| **WBC** | White blood cells |
| **XPS** | X-ray photoelectron spectroscopy |
| **XRD** | X-Ray Diffraction |
| **µg** | Microgram |
| **µl** | Microliter |
| **µM** | Micromolar |

# Synopsis

Nanotechnology is a comparatively new and fast-growing branch of science that finds wide application in almost all industrial areas. The discrete energy levels and specific high band gap in these nanoparticles make them stand different from their bulk counterparts. This difference in the energy levels largely contributes towards their physical and chemical properties such as size, morphology, surface area, surface charge, surface reactivity, crystallinity, purity, and oxidation state. Among the various metallic nanoparticles, our focus is on vanadium pentoxide nanomaterials (Vn). Though applied in various fields like electronics, energy storage devices, solar cells, paint industries, etc., their full effects on the biological system are still not apparent.

Natural dietary sources of vanadium include a variety of sea fish, sea cucumbers, and mushrooms. The body absorbs only 1 % of the total dietary vanadium. This element act as a cofactor in various enzymes. At the same time, the exact molecular mechanism of action in biochemical pathways needs further detailed evaluation. In the clinical scenario, vanadium elicits significant role in nutritional cancer chemoprevention, as reported in a preclinical study conducted in 2012, involving breast cancer women and healthy control women subjects. The study found that those subjects whose urine samples contained a substantial amount of vanadium had a lower risk of developing breast cancer at later stages of their life. Pertaining to the structural similarity of vanadium pentoxide with that of the phosphate molecule, they mimic the phosphate molecule and modulate the non-specific activation or shut down of various biomolecular pathways. Even then, the exact mode of action of vanadium pentoxide nanoparticles on cellular systems is not clear. Due to the lack of full proof *in vitro* and *in vivo* studies based on Vn, the present study made efforts to evaluate the microbial interaction, human cancer cell interactions, and *in vivo* clinical interactions of nanoforms of vanadium pentoxide. Since the shape of the nano vanadium plays a significant role in eliciting different properties, very less information is available on the effect of other shapes of this nanomaterial other than nanowires. This study focuses on the sphere (VnNs) and plate-like (VnNp) morphology of vanadium and their antioxidant and pro-oxidant properties *in vitro* and *in vivo*.

The primary objectives of the study are:

I. To synthesize nano vanadium with different morphology and their characterization
II. To understand the difference in the biological activity of nano vanadium on different microbial systems
III. To evaluate the potential of nano vanadium to inhibit breast cancer cell growth *in vitro*
IV. To explore the fundamental interactions of nano vanadium *in vivo*

The objectives are well achieved and explained within six chapters of the thesis.

The **first chapter**, on the introduction, gives the significance and background of the study with a focus on different kinds of nanomaterials and their various biomedical applications. An overview of numerous vanadium-based NMs is also addressed, pointing their advantages over bulk counterparts. This chapter also explains the need for nano-bio interaction studies.

The **second chapter** describes an extensive survey on the available literature reviews on the uses of vanadium as a natural element, its nanoscale synthesis processes, properties of nanoscale vanadium, and its various applications. This chapter also describes articles on various shapes of vanadium, its oxidation state, properties, and cellular interactions of nano vanadium.

The **third chapter** focuses on the materials and methods used for conducting various studies for the completion of the thesis. It includes materials used for the nanomaterial synthesis, methods adopted in characterizing the nanomaterial, and the instrument details used for each of the studies. The hydrothermal preparation of Vn utilized vanadium oxychloride and benzoyl alcohol following calcination steps.

The first subsection of the third chapter deals with the product characterization for its size, shape, sample purity, oxidation state, and surface charge. Material characterization adopted various techniques such as thermogravimetry, differential thermal analysis, transmission electron microscopy (TEM), field emission scanning electron microscopy (FE-SEM), electron dispersive x-ray analysis (EDX), selected area electron diffraction (SAED), X-ray photoelectron spectroscopy (XPS), x-ray diffraction (XRD), Fourier transformation analysis (FT-IR) and Raman analysis.

The second subsection explains the protocol and methodologies adopted for the nanomaterial - microbial interaction studies using representative gram-positive *staphylococcus aureus* and gram-negative *E. coli* bacteria and their details. Minimum inhibitory concentration (MIC) of Vn required to cause 50 % cell death was quantified using spectrophotometry. Changes in surface morphology were studied using FE-SEM analysis. Characteristic peak position and peak shift in the case of biological markers like DNA and proteins were analyzed using Raman spectral mapping.

The third sub-section deals with the cellular interaction studies carried out in normal L929 and a breast cancer cell line MDA-MB-231. As an initial phase, cellular interaction studies, including cell viability and cytotoxicity evaluation, were done using MTT assay. Nanomaterial uptake was confirmed through flow cytometry and TEM analysis of treated cells. Autophagy induction was confirmed through LC3 puncta experiment with a fluorescent microscope at different times. This was reconfirmed with the protein expression studies with western blot analysis. Mitochondrial and lysosomal uptake of VnNs was proved with TEM. Organelle functions were tested using fluorescent dyes like JC-10, Lysotracker red, and acridine orange was used for mitochondrial and lysosomal membrane integrity, respectively. Oxidative damage upon exposure to Vn was also accounted through fluorescence microscopy and spectrophotometrically using DCF-DA assay. The role of Vn to act as an antioxidant and a pro-oxidant in *in vitro* conditions was checked using a pyrogallol auto-oxidation assay. The amount of $H_2O_2$ produced in cells at different time points of Vn treatment was evaluated using an amplex red assay, and the relative mRNA levels of stress response genes were estimated using RT-PCR assay. The mechanism of cell death in cancer cells was established using Annexin V/ PI staining through flow cytometry. Caspase sensor sensitive plasmid transfected cells were used for fluorescence microscopy and observed for caspase activation in Vn treated cells *in vitro*. SEM analysis of cells also proved the membrane blebs, which are characteristic of apoptotic cells.

The last section of this chapter deals with the experimental details of nano-bio interaction studies of Vn on healthy *swiss* albino mice models. The animals were divided into test and control groups. And a single dose (1mg/kg) body weight of Vn in sterile saline was administered through a tail vein, which acted as a test, and *i.v* injection with saline alone was considered as control. Each experimental group had six animals per group and were sacrificed towards day 1, day 3, and day 21 of post-exposure. Blood samples were collected at the time of euthanasia and were subjected to various hematology and biochemical assays. Urine samples collected at specific time points were subjected to Raman spectral analysis for detecting the presence of vanadium in the urine. The study also included details on the organ accumulation and real-time mRNA levels of various stress response markers in organs like liver, kidney, and spleen. The tissue samples were also subjected to histopathology evaluation for pathology observations.

The **fourth and fifth chapters** deal with the results and discussion of all the experiments in the thesis. The first sub-section of this chapter covers detailed results and interpretations of nanomaterial synthesis and characterization. The synthesis method followed a hydrothermal route, which yielded two different shapes of vanadium named as Vanadium nanospheres (VnNs) and vanadium nanoplates (VnNp). These particles were subsequently characterized for their size, shape, oxidation state, sample purity, surface charge, etc. The VnNs, with spherical morphology, showed an average particle size of 50 nm while VnNp with plate-like morphology showed a 1 nm thick compactly packed layered morphology. Both the Vn materials showed high crystallinity with a sherabennite structure correlating well with the PDF 00-041-1426 values. The essential metal-oxygen stretching and bending vibrations in both the Vn samples were clearly observed in the FT-IR and Raman spectral analysis. The surface charge of VnNs was found to be -13 MeV and -21 MeV for VnNp. The initial cytotoxicity studies for optimizing the concentration of Vn materials were evaluated using MTT assay with immortalized triple-negative breast cancer MDA-MB-231 cell lines and healthy mouse fibroblast cell line L929.

The second sub-section focus on details of the nanomaterial - microbial interactions using representative gram-positive *staphylococcus aureus* and gram-negative *E. coli* bacteria. A comparative study analyzing the MIC values of VnNp and VnNs denoted an increased antimicrobial activity of VnNp towards *E. coli* bacteria. The surface morphology evaluation revealed surface depressions on the *E. coli* bacteria when subjected to VnNp treatment, while the treatment with VnNs on *S. aureus* didn't elicit such morphological alterations. The alterations in molecular markers like protein and DNA were evaluated using Raman spectral mapping of live bacterial cells. The mechanism of cell death in VnNp treated cells were assessed with reactive oxygen species (ROS) specific DCF assay. The experiment proved that the antimicrobial activity of VnNp is mediated through ROS generation in *E. coli* biofilms.

The third sub-section cover details on various *in vitro* nano-bio interaction studies using healthy mice fibroblast cell line L929 and breast cancer cell line MDA-MB-231 with VnNs. It was found that the VnNs didn't cause damage to the L929 cells, while at the same time, a 50μM VnNs treatment on cancer cells resulted in 50 % cell death towards 48 h of treatment. Hence, the nano-bio interaction studies of VnNs were completed with MDA-MB-231 cells to know more about the cell death pathway and the mechanism behind it. Efficient VnNs uptake was proven with flow cytometry, Raman cell mapping, and electron microscopy. The VnNs were non-fluorescent in nature, and hence electron microscopy was extensively used throughout the study to validate the presence of Vn at different time points of nanomaterial incubation. Nano-bio interaction studies proved autophagy induction at 4 h and found that a 2 fold increase in LC3 II proteins with VnNs treatment. Electron microscopy also depicted autophagy specific autophagosome formation and lysosomal maturation. Also, it found that VnNs treatment-induced changes in mitochondrial membrane potential and induced mitochondrial and lysosomal uptake. VnNs were also found to efficiently quench the intrinsic ROS levels towards 4h of nanomaterial incubation and were later found to reverse this phenomenon by activating ROS formation in MDA-MB-231 cells. The singlet oxygen quenching activity was also confirmed with the inhibition of the pyrogallol auto-oxidation experiment *in vitro*. The real-time mRNA levels of superoxide dismutase (SOD) and catalase were found to have a reasonable correlation with the ROS levels at various time points, which gave a clear indication that VnNs along with the cellular machinery were actively involved in causing cancer cell death, which was evident in the MTT assay. The VnNs treatment also resulted in cell cycle arrest, inhibited cell migration, activated caspase-mediated cell death in cancer cells.

The fourth sub-section deals with the fate of these nanomaterials on standard swiss albino mice models. The single-shot tail vein injected VnNs were found to get eliminated through urine, which was analyzed at different time points via Raman spectral analysis. The spectra identified the specific peak of V-O at 994cm$^{-1}$ in the urine samples until 72 h of post-exposure, denoting the elimination pattern of VnNs. The study on traces of elemental vanadium in the excretory organs like liver, kidney, and spleen denoted that the material was cleared off from the kidney while traces were present in the spleen after 21days of post-exposure. Various blood parameters evaluated indicated normal levels of urea, creatinine, ALT, AST, while lowered the cholesterol levels significantly towards 21-day post-exposure. Various hematology parameters were also found to be healthy other than an increase in WBC levels observed, which could possibly be due to the organ accumulation of VnNs in the spleen. The real-time mRNA levels of various antioxidant genes showed an initial increase in the SOD1,2,3 and catalase in the kidney, while the levels significantly dropped back to normal by the end of 21 days. In the case of liver and spleen, the levels of SOD and catalase mRNA were found considerably high towards day three and day 21 of post-exposure. The histology observation denoted typical pathology in the spleen and kidney. However, the liver samples were found to have mild lesions and cellulitis. Hence, the overall interaction of VnNs on mice models was studied to have a preliminary idea about the behavior of these nanomaterials on a multicellular mammalian live system.

**The sixth chapter** deal with the summary and conclusion of the work. Successfully synthesized two different nano-formulations of vanadium with different morphologies. The VnNs and VnNp were characterized to study their bio-nano interactions *in vitro* and *in vivo*. The current study marks an important finding that a nanomaterial could elicit two entirely different properties *in vitro,* depending on the concentration and period of exposure. Here, VnNs exhibited antioxidant property and autophagy induction in MDA-MB-231 cells during the initial points of incubation. While further, nanomaterial exposure resulted in oxidative damage inside the cells by inducing damage to mitochondrial membrane potential and subsequent caspase-mediated apoptotic cell death towards later time points. The study focussed on evaluating the significant role of antioxidant genes, both *in vitro* and *in vivo* conditions. In addition to that, the study also focused on the development of *in vivo* risk assessment with the minute quantitates of the nanomaterial, as a majority of the previously reported work focus on the extreme dose toxicity profiles. While the actual human exposure limit could lie far below that limit, overall, this study focused on the *in vitro* and *in vivo* interactions of nanoscale vanadium pentoxide by utilizing different approaches to achieve the objectives.

# CHAPTER - 1

# 1 INTRODUCTION

This chapter presents an overview of the classification, applications, and importance of nanomaterials and various interactions of nanomaterials at the biological interface.

## 1.1. Introduction to Nanomaterials

Materials with any one dimension less than 100 nanometers (nm) are considered as Nanomaterials (NMs). Nanoscale materials can have a natural origin, as they are abundant in fossil remains of seashells, skeletons, etc. and believed to result as primitive meteorite impact on the earth's crust. However, due to the advancements in the scientific world, nowadays, chemically synthesized NMs are also and in a plethora of fields. The importance of miniaturization of materials gained significant attention after the famous lecture by the Nobel laureate **Richard Feynman** delivering his speech about “There's Plenty of Room at the Bottom,” in the Annual Meeting of American Physical Society at the California Institute of Technology, on the 29th of December 1959. This talk, paved the way for the emergence of different branches of science, that involved studies with atoms, molecules, structures, and materials in the “nm” scale, termed as “Nanoscience.” Soon after, nanotechnology has evolved dealing with manipulating materials at the atomic level to solve many of the existing scientific problems in various fields. The studies also grew as electron microscopy techniques developed simultaneously, which enabled researchers to characterize and monitor the size and shape of the synthesized nanomaterials. Due to the high-end research performed in the field through advanced engineering skills, the NMs are termed as engineered nanomaterials (ENMs). Pertaining to their size, surface area to volume ratio, exceptional optic, electric, magnetic, and catalytic properties, the NMs are used for various specific intended applications such as electronics, medicine, biosensing, artificial energy resourcing, etc. Their tiny size makes them stand apart from their bulk counterparts as they possess higher chemical reactivity, adding to their significant commercial influence in the range and nature of functionalities, which positively increase their demand in the future. Commercially available products contain various

NMs covering a wide range from electronic and optical devices to various medicines, thereby gaining essential roles in our day-to-day lives. The Project on Emerging Nanotechnologies (PEN) under the Consumer Product Inventory (CPI) in 2006 reported around 54 products manufactured with a nanotechnology approach. Interestingly the number of products grew up to more than 1600 products by 2015 as per reports of (Vance *et al.*, 2015).

## 1.2. Classification of Nanomaterials

Classification of NMs is based on different aspects such as dimension, size, or nature of the composition. According to classification under dimensions, they are classified as zero-dimensional (0-D), one-dimensional (1-D), two-dimensional (2-D) or three-dimensional (3-D) materials. In the case of 0-D materials, all the three dimensions (x,y,z) fall in the nanoscale range with no significant difference between the longest and the shortest axes and most commonly these 0-D NMs are referred to as "nanoparticles." While in the case of 1-D materials, they have one of their dimensions above the nanoscale such that there is crystal growth at any of the x, y, z-axis. Most of the 1-D materials possess shapes such as nanotubes, nanorods, nanowires, etc. The 2-D NMs exhibit a plate-like morphology, as any two of their dimensions fall above the nanoscale, which could include shapes such as nano-layers, nano-films, and nano-coatings. While the 3-D NMs have none of their dimensions confined to the nanoscale, and they have significantly large random dimensions above 100 nm. They hold dispersions most typically in diverse orientations such as bundles of nanowires, nanotubes as well as multiple nanolayers of nanocrystalline structures. Based on the crystallinity, they are classified as either amorphous or mono/ polycrystalline structures. NMs could also be composed of single or multiple elements in various forms, shapes and be semiconductor-based, metallic, ceramic, or polymeric in nature. Based on the composition of metallic NMs, they can be of carbon origin such as in fullerenes, diamonds, graphite, graphene, or of other metallic origins like quantum dots, nanogold, nanosilver and nano oxide forms of the iron, copper, zinc, titanium, vanadium, etc.

## 1.3. General applications of Nanomaterials

NMs, owing to the larger surface area to volume ratio, quantum effects, and uninfluenced gravity, possesses novel intrinsic mechanical, electrical, thermal, magnetic, catalytic, and optical properties. These materials also find their way into highly demanding commercial fields such as military, medicine, cosmetics, and even in pollution control in the environmental sector. Chemically inert NMs are considered as suitable candidates as packing material in the food industry. Semiconductor-based nanoparticles below 10 nm or even less such as silicon (Si), silicon-germanium(Si-Ge), zinc selenide (ZnSe), zinc sulfide (ZnS), cadmium sulfide (CdS), cadmium selenide (CdSe), etc., showcase excellent electronic and optical properties pertaining to the quantum confinement which make them promising towards applications such as laser technology, solar cells, nanoscale electronic devices, light-emitting nanodevices, and biosensors. Both quantum dots and quantum wires are promising NMs for use in lasers and light-emitting diodes (LED) for future optoelectronic applications. Carbon nanotubes with one electron wave mode are involved in the transport of electrical current hence used for electrical conductivity applications and in microbial fuel cells. Silica nanoplates, carbon nanorods, and carbon nanotubes are used to improve the mechanical strength of polymeric materials significantly. Aluminum nanoparticles pertaining to their high reactivity are utilized as solid-fuel propulsion to send heavy payloads in rockets. Nanocrystalline structures such as the ZnS, ZnSe, CaS, and PbTe are used for developing high definition computer and television screens. The size of these materials in the nanometer range (‘phosphors’) attributes to the high pixel intensity and resultant high-quality pictures in the display monitors. Transparent NMs such as Zinc oxide ($ZnO_2$) and titanium dioxide ($TiO_2$) nanoparticles are used in sunscreens, paint, paper, cosmetics, and also in the food industry. These NMs do not penetrate the skin layers; they do their job by sitting on the skin surface and are essential for excellent UV protection applications. NMs such as carbon nanotubes, gold, quantum dots, etc. are used for microbial sensing and as test material in the food industry.

## 1.4. Biomedical applications of Nanomaterials

Global Cancer Observatory (GCO), in collaboration with the world health organization (WHO), is an interactive web-based platform that provides information on global cancer statistics, predictions, and control measures for the future. According to their global cancer statistics, the incidence of new breast cancer accounts for 11.6 % of the total cancer incidences. Moreover, the overall death reports associated with breast cancer contributes to 6.6 %. Currently, there are many kinds of available anticancer drug preparations with target specificity. Despite the fact, lack of timely diagnosis, poor bioavailability, and adverse side effects of treatment strategy contribute towards high mortality.

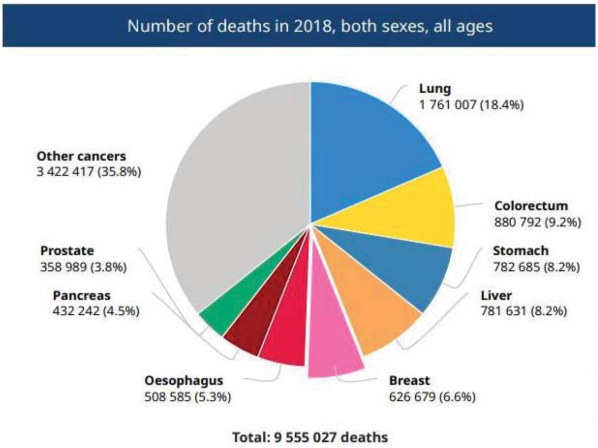

**Figure 1.1 Statistics on total deaths due to cancer.** Adopted from the online Global Cancer Observatory database

This scenario has paved the way for the emergence of nanomedicine with a focus on controlled and targeted drug release to increase the efficacy and reduce side effects associated with conventional anti-cancer molecules. In addition, nanomedicine has contributed immensely to various biomedical applications such as bioimaging, biosensing, tissue engineering, drug delivery, developing minimally invasive implantable devices, etc. (Choi and Sun, 2011; Bao, Mitragotri and Tong, 2013).

One such application in bioimaging involves the development of high contrast imaging agents for optical and MRI applications. The superparamagnetic property of ultra-small sized iron oxide Nps (SPIONS) makes them suitable candidates for use in magnetic resonance imaging (MRI) as efficient MRI contrast agents (Saraswathy *et al.*, 2014), magnetic separation of biological samples (Nimi *et al.*, 2018), bioimaging (Zheng *et al.*, 2013), targeted drug delivery (Ansari *et al.*, 2014; Nair *et al.*, 2017) and also in magnetic hyperthermia (Beeran *et al.*, 2015) mediated cancer therapy.

Gold nanoparticles are widely used for biosensing applications pertaining to the ease of NM synthesis and unique physicochemical, optical, and excellent biocompatibility properties (Wan *et al.*, 2015). Owing to their strong absorbance maxima, excellent photostability, and efficient heat transfer, they are used in photothermal therapy for cancer management (Huang *et al.*, 2006).

Nanoparticles also achieved the targeted delivery of chemotherapeutic drugs such as paclitaxel, doxorubicin, methotrexate, 5-Fluorouracil, etc. by conjugation with specific tagging antibodies (Zolata, Abbasi Davani and Afarideh, 2015). In recent times, nanorobots developed with atherosclerotic plaque specific antibody- complexed - nanoparticle, have been used to clear blocked arteries in atherosclerotic patients (Moghimi, Hunter and Murray, 2005). In theranostics, microscopic, sensitive, and reliable target detection agents are applied for imaging as well as therapy.

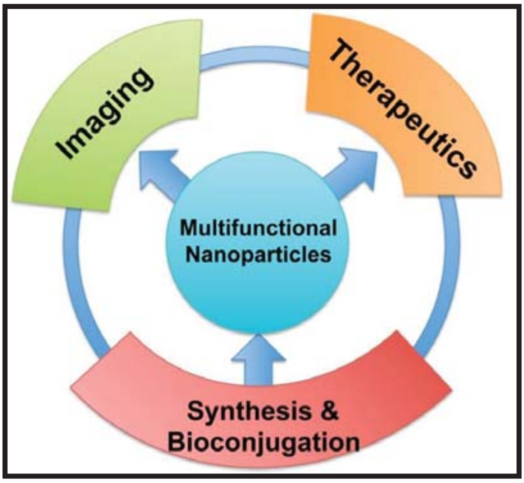

**Figure 1.2 Biomedical applications of nanoparticles.** Adapted from (Choi and Sun, 2011)

For gene delivery applications with improved therapeutic performance, redox responsive polymeric nanocarriers with sensitive disulfide (S-S) links are used (Bao, Mitragotri and Tong, 2013).

Another area where nanotechnology comes in is the biomimetic and intelligent biomaterials for *in-situ* tissue regeneration applications (Das *et al.*, 2007). The graphene nanosheet patterned surface controls the growth and differentiation of stem cells and stimulates stem cell regeneration in damaged vascular tissue (Lee *et al.*, 2011). Bacterial contamination and biofilm formation are important nosocomial factors that are dealt with various NMs. Surface coating of medical devices and implants with silver nanoparticles inhibit surface adhesion of bacteria and prevent biofilm formation (Slavin *et al.*, 2017). In addition, enhanced cell adhesion and bone resorption within the implanted material are achieved through incorporating ceramic and metal-based NM coating. Some other NMs possessing the antibacterial property and intrinsic anti/pro-oxidant properties are oxides of zinc, manganese, copper, gold, and vanadium nanoparticles (Mu *et al.*, 2016).

## 1.5. Need for Nano-bio interaction studies

Detailed studies on understanding interaction between nanomaterials and living system are essential, as it plays a crucial role in developing NMs for bio-medical applications with particular attention to their safety aspects.

### 1.5.1. *In vitro* response to Nanomaterials

Cell lines are widely used for the first stage evaluation of nanomaterial biological interaction and hazard analysis. They offer better reproducibility while trying to make out interlaboratory comparisons. Also, a great job is to be done while selecting the appropriate cell lines for the indented research under investigation. Primary cell culture systems and even co-culture models are often preferred over cell line studies to achieve a better understanding of the typical cell interaction scenario, as hybridoma technology utilizes cell fusion with a cancer cell, in order to impart immortality to the developed cells lines. While primary cells need fresh cultivates from the explants, which make the whole process to consume more time and is laborious. Nanomaterial interaction with the biological system involves a complex process, which needs to be substantially reproducible inter-laboratory results without failure. In the case of a primary cell culture system where the results depend primarily on the isolation and handling procedure, results might sometimes fail to exhibit reproducibility between laboratories. Owing to these reasons, cell lines are mainly preferred to study the nanomaterial biological interactions.

The cellular response to NM treatment much depends on their intracellular delivery, persistence, and distribution within. Many of the NM possess fluorescent properties, which make them easily trackable inside the cells, while non-fluorescent NM trafficking is done through non-fluorescent techniques, including the Transmission electron microscopy technique. Uptake of small-sized NM is through the process of endocytosis, and even much smaller particles directly interact with the membrane system and enter the cells bypassing the endocytic mechanism. Once inside the cells, NM interacts directly with many of the cellular organelles, such as lysosomes, mitochondria, and nucleus. Such interactions could also alter mRNA and protein synthesis affecting mitochondrial electron transport chain, oxidative imbalance, and altered cell cycle, which activate downstream cell death signaling mechanisms.

Adding to cell studies in detail, cell viability experiments such as MTT and MTS assays considered as first step assays to achieve before proceeding to any other cell-based studies. These assays involve the proper setting of positive and negative controls to eliminate any chances of false positive or negative results. They are the (a) "NM-only" control which takes care of any possible interferences from the optical reader, (b) "NM + assay reagents" to eliminate any interferences with the reagents, (c) "absolute positive/negative controls" to reduce chances of a defective biological system. Even after strictly following the above-mentioned parameters, the results might show variances that attribute towards the individual differences in cell handling. Factors such as NM preparation and cell treatment affect the comparability of results, hence considered these aspects also in the assays. Even though there is no correlation between the highest *in vitro* concentrations with that of the *in vivo* test concentrations, often, the former assist in developing strategies for designing the latter, which is performed for practical efficacy testing, using rodent models.

### 1.5.2. Safety and Toxicity of Nanomaterials

NMs are widely used in various fields as discussed above, yet complete safety evaluation is still in its infant stages. Nanoparticles being extremely tiny in nature, show far different properties in comparison with their bulk counterparts. This property makes NMs freely diffusible through the skin or through mere inhalation or via ingestion. Most importantly, nanomaterial inhalation affects the lungs resulting in inflammation and tissue damage, which further progress towards fibrosis and tumor generation. Pertaining to the antimicrobial properties of NMs, they have also been used by the food packaging industry, while the risk assessment regarding the use of these

NMs is also very essential. Water purification systems with nano-membranes developed from carbon nanotubes (CNT) are in reports while the same nanomaterial also possesses to have some health risks and challenges in mice models. Once the CNTs reach the circulatory system, they could persist inside the body, which might elicit toxicity profiles. Accumulation of such NMs in the tissues eventually results in tissue dysfunction, damaging the entire biological system of the organism. The National Institute for Occupational Safety and Health (NIOSH) stated that any occupational exposure via inhalation of nanoscale $TiO_2$ particles is regarded as a potential occupational carcinogen.

Therefore, it is essential to create standard protocols for risk assessment in the handling and usage of NMs for future applications. Usage of workstations equipped with high-efficiency particulate air (HEPA) filters and personal protective equipment (PPE) can significantly reduce any possible chances of exposure to NMs.

### 1.5.3. *In vivo* response to Nanomaterials

Commonly used animal models for biomedical research include mice (conventionally bred or transgenic), rats, rabbits, pigs, sheep, goats, dogs, hamsters, guinea pigs, and Drosophila models. They are used extensively in fields such as gene delivery, tissue engineering, and regenerative medicine to improve the biocompatibility and functionality of artificially regenerated tissues such as bones, cartilage, skin, neurons, or even soft tissues. It also plays a vital role in understanding the toxicological profiles of artificially synthesized NMs. Animal models serve as an excellent tool for validating the targeted use of NMs as contrast agents in various optical and MRI applications. Most of the *in vivo* interaction studies are carried out with extremely high NM concentrations in order to determine the influence of treatment. Though, the valuation for possible health effects of NMs in humans requires concentration based on real situation human exposure quantities either dermal, oral or respiratory route as with any NM manufacturing industry or other similar scenarios. However, limited information is available in this range for many of the NMs; hence, dose estimates are designed built on the worst-case models (Costa, 1997). There are many studies that describe the effect of acute exposure of high concentration NMs, while only a few reports are available on low concentration long-term studies, which attracts attention that needs to be addressed (Rojas *et al.*, 1999). The *in vivo* NM interaction studies provide sufficient data on the absorption, distribution, metabolism, excretion, and toxicity (ADME Tox) of nanomaterials. Booth et al. suggested the use of lower and higher bounds for conducting animal studies (Booth, Laye and Spangenburg, 2010). *In vivo* toxicity evaluation, studies investigated different routes of administration such as dermal, inhalation, injection, or ingestion, which mimick the real chances of ways of exposure. Usually, related factors in the toxicity of nanomaterials are to their size, shape, surface charge, stability, solubility, crystalline forms, and composition. Correctly, the size of the NM plays an essential role in the cellular uptake mechanism and, thus, their distribution and elimination from the body. Small-sized nanomaterials have a greater tendency to accumulate specifically in specific tissues due to the predominance of phagocytic cells in the reticuloendothelial system of the spleen, liver, and kidneys, organs involved in NM excretion. The *in vivo* interaction of transition metal-based NMs induce oxidative stress through free radical generation in such a way that it overpasses the anti-oxidant machinery operating under normal conditions. The generated free radicals trigger subsequent mitochondrial and genomic DNA damage, imparting chromosomal damage and activate cell death machinery.

*In vivo* interaction studies defining nanoparticle fate, effect, and induced response are essential factors to be addressed in the practical design of drug delivery carriers for therapeutic applications for future applications. For efficacy evaluation, the most significant problem in testing methods with animal models is that the ways in which humans and laboratory animals behave towards the same nanomaterial will be different and significantly prevent extrapolation of the results. In addition, people working with the synthesis and characterization of NM might not necessarily think about their biocompatibility and toxic aspects to the life forms. Hence, it is in high demand to bring together people from both the areas to work together for mutual interest to address some of the generic challenges in its application.

## 1.6. Background of the study

Evaluating the biological interaction profile of vanadium pentoxide nanomaterials (VnNMs) is an excellent endeavor in the emerging era of nanomaterials in order to ensure its safety aspects. Since nanoparticles have their physical, chemical, and biological properties entirely different from their bulk counterparts, extensive studies are essential in understanding the exact mechanism of action with nanoformulations. People working in industries dealing with commercial-scale production of nanomaterials are at high risk of exposure. Even though VnNMs are used in various fields such as electronics, energy storage devices, solar cells, paint industries, etc., their effects and biological interaction studies are still not up to the mark. Exposure to a deficient concentration of VnNMs may not have a visible impact on humans, but there is limited evidence on their long-run effect. Pertaining to the lack of full proof *in vitro* and *in vivo* studies on VnNMs, made efforts to evaluate their interactions on human cancer cells, microbial systems and on Swiss albino mice models. Even though the exact mode of action of VnNMs on cells is not understood, they are believed to mimic phosphate molecules pertaining to their structural similarity and are also thought to affect various biomolecular pathways. Since phosphate molecules act as critical players in the activation and shut down of many molecular events in the cells, it is worth attempting to have a study on various biological interaction pathways at the molecular level.

## 1.7. Objectives

Attributed to the various noted applications of VnNMs in many fields, there emerge commercial-scale production of these NMs, which creates a situation where more people are exposed, and there appears the importance of understanding the biological interaction and evaluates the safety aspects of these nanoparticles. Many biological interaction studies have been reported with the bulk and complex forms of vanadium even from the early 80’s, but still, there is a few understanding on the way of their action when brought in the nanoformulations. In addition, naturally found vanadium sources include a variety of sea fish, sea cucumbers, and mushrooms, which exhibit essential roles in muscle mass development. In addition, some preclinical studies conducted on women subjects found that a substantial amount of vanadium in urine samples had a lower risk of developing breast cancer at later stages of life. There are also reports showing the toxic effects of vanadium, being said that, it is important to optimize the concentration of nanomaterials to be used for such biological studies. The vanadium nanowires mediated antioxidant studies on microbial systems have been demonstrated earlier, and they proved that Vn elicits an antioxidant potential in cell culture environments by exhibiting a nanozyme like activity. Even though many of these experiments are conducted with vanadium nanowires, very less information is available on the effect of other shapes of this nanomaterial. Adding to that, the biological interaction of nanoparticles depends heavily on its size, morphology, surface charge, crystallinity, purity, and oxidation state we have planned our study to monitor the cellular, microbial and *in vivo* animal model interaction studies with the sublethal concentrations of two different morphologies of VnNMs.

Hence, the present study hypothesizes that similar to the bulk and other forms of vanadium oxides, “Nano vanadium pentoxides” could also serve similar antimicrobial and anti-cancerous properties. Here, in this study, the focus is on understanding the underlying biological interactions of VnNMs on microbial models, triple-negative breast cancer cells, and *in vivo* small animal models, The present study has three primary objectives to achieve the hypothesis.

The objectives are;

**Objective I**: Synthesis and characterization of VnNMs

**Objective II**: *In vitro* nano-bio interaction studies

Phase 1: Microbial interaction studies of VnNMs with bacterial systems

Phase 2: Cell line interaction studies of VnNMs on normal healthy cells and triple-negative breast cancer cells

**Objective III**: *In vivo* acute toxicity studies using Swiss albino mice. Organ-specific accumulation, corresponding toxicity, elemental analysis, blood and urine analysis, tissue-specific gene expression analysis, and histopathology evaluation are explained under the scope of this study.

## 1.8. Thesis outline

Divided the whole thesis into six chapters.

The **first chapter**, on the introduction, gives an idea of different kinds of nanomaterials and their various applications. An overview of vanadium-based NMs and their advantages over bulk counterparts are integrated. It also includes a brief description of the work done, cellular responses, and an outline of the *in vivo* study.

The **second chapter** describes some of the available literature reviews on the uses of vanadium as a natural element, its nanoscale synthesis processes, properties of nanoscale vanadia, and its various current applications.

The **third chapter** focuses on describing all the materials and methods used for conducting various studies in the thesis. It includes materials used for the hydrothermal preparation of VnNMs; multiple methods adopted for characterizing the nanomaterial, including instrument details used for each of the studies. Details on cellular interaction studies carried out in normal cell L929, cancer cell line MDA-MB-231, representative gram-positive and gram-negative bacteria's are also described in this chapter. The last section of this chapter deals with the nano-bio interaction studies on *Swiss albino* mice model detailing with the biodistribution, organ accumulation, blood parameters, urine analysis, quantitative mRNA levels, and histopathology.

The **fourth chapter** deals with the results of all the experiments. The first sub-session of this chapter covers detailed results and interpretations of nanomaterial characterization. The second sub-session includes details of various *in vitro* nano-bio interaction studies using cell lines.

The third sub-session focuses on the microbial interaction studies, and the fourth sub-session deals with the fate of these nanomaterials *in vivo* covering the biodistribution, organ accumulation, blood analysis, quantitative mRNA levels, and histopathology.

The **fifth chapter** gives a detailed interpretation and discusses all minute details on the results. The first subsection deals with the discussion on results obtained for the synthesis and its corresponding characterization. This followed descriptions of various cellular and molecular events obtained through many *in vitro* assays in cell lines and bacterial systems. The last subsection discusses *in vivo* findings involving organ distribution, blood parameter evaluation, quantitative mRNA levels, and histopathology.

The **sixth chapter** deals with the summary and conclusion of the work. The current study makes an important finding that a nanomaterial could elicit two entirely different properties with *in vitro* conditions depending on the concentration and period of exposure. Here, VnNs exhibited antioxidant property in MDA-MB-231 cells during the initial points of incubation, while upon further nanomaterial exposure, it resulted in oxidative damage inside the cells. We have focussed on evaluating the significant role of antioxidant genes in both *in vitro* and *in vivo* conditions. In addition to that, we also focused on the *in vivo* risk assessment with a minute quantity of the nanomaterial as the majority of the previously reported work focus on the extreme dose and toxicity profiles. Often the actual human dose exposure could lie far below that limit.

# CHAPTER - 2

# 2 REVIEW OF LITERATURE

## 2.1. Introduction to vanadium

**Vanadium** is a transition element with atomic number 23, represented through the symbol "V." Naturally, the element is rarely found on the earth crust, which rapidly forms oxide layers over its surface to prevent oxidation, while they are also chemically synthesized into many other forms like sodium orthovanadate ($Na_3VO_4$), vanadyl sulfate ($VOSO_4.xH_2O$), sodium metavanadate ($NaVO_3$), vanadium pentoxide ($V_2O_5$), etc. (Korbecki *et al.*, 2012).

Vanadium is present in most of the food items consumed. Among which the rich sources of dietary vanadium include rice, soybean, mushroom, and black pepper. In addition, several kinds of seafood, such as shellfish and sea cucumbers, also contain enough dietary vanadium (Badmaev, Prakash and Majeed, 1999; Bishayee *et al.*, 2010). The human body contains roughly 0.3 μM of vanadium concentration, which shows slight variations between people based on their diet (Byrne and Kosta, 1978). However, the actual role of this element is still an area of debate between adversity and benefit ability (French and Jones, 1993). There are many studies reporting both of these effects, which is further attributed to many other supporting factors. Vanadium compounds have effects on the manifestation of some of the human diseases while they also play a role in maintaining various natural body functions. (Clarkson and Rawson, 1999). This trace element in the human body play essential roles in the normal functioning of the thyroid gland, (Badmaev, Prakash and Majeed, 1999; Wang *et al.*, 2016) maintain calcium homeostasis, (Ehring *et al.*, 2000) manage glycemic balance, (Badmaev, Prakash and Majeed, 1999; Pereira *et al.*, 2009) and also helps in fat metabolism (French and Jones, 1993). Vanadium sulfate is found to elicit insulin-mimetic activity (Mukherjee *et al.*, 2004). Vanadate has a higher affinity towards bone structures and shows similarities to phosphate molecule and gets accumulated in the hydroxyapatite components in bone structures (Pessoa, Etcheverry and Gambino, 2015). Adipose tissue act as a storage pool for vanadate (Rehder, 2012) and are is also used as a nutritional supplement in building muscle mass by the athletes.

## 2.2. Methods of nano vanadium synthesis

Various vanadium pentoxide $V_2O_5$ nanostructures such as nanobelts, nanotubes, nanofibers, nanorods, nanowires, and mesoporous structures have already been synthesized by a variety of methods, including sol-gel process, reverse-micelle technique, hydrothermal treatment, sonochemical treatment, and physical vapor deposition.

Zhou *et al*. prepared elliptical $V_2O_5$ macro-plates using water/ethanol media. They found that the final shape of the $V_2O_5$ plates had a strong relation to the ethanol/water ratio and the reaction time (Zhou *et al.*, 2007). This method produced vanadium pentoxide macro-plates with highly anisotropic structure and efficient electrical and optical properties pertaining to its orthorhombic structure. A reflux precipitation reaction with ammonium vanadate when thermally decomposed, yielded nanosized vanadium oxides (Reddy *et al.*, 2008). In the sol-gel method, a precursor solution is converted into the sol and later converted to gel through a hydrolysis and condensation reaction. This follows an aging, dehydration, and temperature treatment to yield vanadium doped thin films over various substrates (Osmolovskaya *et al.*, 2014). In hydrothermal treatment, the pH and temperature of the reaction condition greatly influence the morphology of vanadium pentoxide based nanostructures. Heating $V_2O_5$ with TMAOH at different pH yields layered compounds (pH 14), nanoplates (pH 6), and nanoribbons (pH 3) (Livage, 2010). In all these different shapes, the structure showed the orthorhombic $V_2O_5$ phase. A reverse micelle technique is adopted to synthesize divanadium pentoxide nanorods and nanowires by controlling the reaction time in the micellar solution (Pinna *et al.*, 2003). This method yielded high uniformity and distinct surface morphology to the nanomaterial system with high crystallinity. Thin films are usually synthesized using physical vapor deposition (PVD) techniques, such as pulsed laser deposition, sputter coatings, and evaporation decomposition. Here, reaction conditions are closely monitored to achieve specific film quality to be applied for smart window applications (Vu *et al.*, 2019).

## 2.3. Industrial applications of nano vanadium pentoxide

Nanomaterials possess novel properties as compared to their bulk and complex forms with specific attributes to its organized morphology and are of high interest to materials scientists all over the world. In fact, it has been demonstrated that the physical properties such as electrical, optical, and magnetic properties are strongly related to the specific physicochemical characteristics of these nanoparticles. The oxidation state, crystal structure, size, and shape of the material dramatically contribute towards this. Attributed to the large surface area to volume ratio, they find a suitable application for use in building materials. Such as vanadium dioxides used in creating smart windows that control infrared (IR) radiation falling on the building, thereby modulating the room temperature based on the received illumination (Hao *et al.*, 2018).

### 2.3.1. Catalysis

Vanadium pentoxide has been widely known as the catalyst for producing sulphuric acid by utilizing the oxidation property for years. Another widely used application of the oxidation property is to produce maleic anhydride (Fumagalli *et al.*, 1994) and phthalic anhydride (Dias, Portela and Bond, 1997). Gimeno et al. systematically studied the $V_2O_5$ mediated catalytic oxidation process of o-xylene to phthalic anhydride (Gimeno *et al.*, 2008). Mainly the V=O bond in nano $V_2O_5$ acts as the catalytic center in oxidation reactions. Vanadium phosphate is used as a catalyst in converting butane to maleic anhydride (Song *et al.*, 2006). The catalytic performance of vanadium oxide is dependent on its nanostructure, which is improved by tightly controlling various synthesis parameters. Taufiq *et al*. synthesized catalytic $V_2O_5$ nanorods via sonochemical treatment, with highly efficient n-butane conversion properties.

### 2.3.2. Gas sensing

$V_2O_5$ nanostructures have been used as components in gas-sensing materials pertaining to their size, shape, crystallinity, high surface-area-to-volume ratio, etc.

Selectivity and sensitivity are the two crucial aspects regarding gas sensing, where Liu et al., reported hydrothermally synthesized vanadium pentoxide nanobelts with high sensitivity towards ethanol (Liu *et al.*, 2005). Further, vanadium pentoxide nanoribbons are utilized for ethanol, hydrogen gas, and organic amine detection with higher sensitivity (Biette *et al.*, 2005). Also, spindle-like $V_2O_5$ nanowire bundles synthesized using a sonochemical method is applied for concentration-dependent detection of serum albumin levels (Mao *et al.*, 2006)

### 2.3.3. Lithium batteries

Different morphologies of nano $V_2O_5$ is reported to be applied as a cathode material in lithium-ion batteries (LIBs) like thin films, (Jin *et al.*, 2008) nanowires, (Zhai *et al.*, 2010), nanorods, etc. The layered morphology and crystallinity in vanadium nanorods are beneficially utilized for making cathode electrodes using their van der Waals forces and applied in LIBs. Also, vanadium nanorods from self-assembled $V_2O_5$ hollow microspheres are applied in LIBs (Cao *et al.*, 2005). Spray-pyrolysis is a widely used technique that is adopted for the synthesis of nanoporous $V_2O_5$ structures for LIBs (Feng *et al.*, 2008). Nano-porous vanadium pentoxide spherical particles possess excellent electrochemical properties to be utilized for various applications (Feng *et al.*, 2008). Reverse micelle technique is adopted for the synthesis of phase pure $V_2O_5$ nanorods (Liu *et al.*, 2018). Cyclability is a significant concern in taking nano vanadium for electrode preparation. Various reports state that the property is improved if conjugated with conductive polymers such as polyaniline (Li *et al.*, 2009) and polyethylene oxides (Subba Reddy *et al.*, 2008), etc.

## 2.4. The biological relevance of vanadium compounds

Most of the nanomaterials exhibit concentration-dependent structural and functional alterations in various biomolecules like lipids, carbohydrates, proteins, DNA (Hussain *et al.*, 2012), and even affect cellular organelles. Once inside the human body, vanadium, as such, or their by-products interact with the cellular machinery and cause various adverse intracellular effects such as reactive oxygen species (Kohen and Nyska, 2002), (Singh *et al.*, 2015). The uptake of vanadate is often affected by the presence of chelators, and it increases the chances of urinary and fecal excretion of vanadate in experimental rats (Hansen, Aaseth and Alexander, 1982).

However, detailed studies on the exact fate of nanomaterials within the cells and its nano-bio interaction studies are still lagging. Being said that, the precise molecular mechanism behind the anticancer, antilipidemic, and anti-diabetic properties of vanadium compounds and its overall influence on subcellular organelles, cells, tissues, and organisms is not yet fully understood. Due to the lack of such in-depth knowledge, Nanomedicine has not yet matured from its infancy even after a research history of many decades. These reactions impart great biological significance and open new avenues of research.

### 2.4.1. Enzyme activation and deactivation

Vanadate has a structural similarity with that of the phosphate molecule that enables competition for the physicochemical properties of the later (Fouani *et al.*, 2017). Act as functional mimics in cells and influence various enzymatic pathways such as nonspecific phosphatases, ATPases, and kinases (Mukherjee *et al.*, 2004). Vanadate with trigonal bipyramidal geometry, establish a stable transition state with the enzyme and inhibits more potent activity than those with any other coordination. The enzyme activation by vanadium in cells trails a secondary mechanism. Here, vanadium trigger enzyme activity by forming ligand complexes that show close resemblance with their physiological substrates. Many of the enzymes possess tyrosine residues at their active sites, which get esterified and mimick phosphorylation under the influence of vanadate molecules. An example is the activation of glucose- 6-phosphate dehydrogenase by the vandalization of tyrosine residues (Crans, 2015). Vanadium also stimulates the activity of PI3-K enzyme, which plays a crucial role in insulin metabolism and also takes part in the mitogenic activity of cells (Kawabe *et al.*, 2006).

### 2.4.2. Insulin mimetic activity

Kinases involved in the insulin receptors exhibit a constant balance between the phosphorylation–dephosphorylation processes and impart extreme significance in managing their functions (Korbecki *et al.*, 2012). Its been proven through *in vitro* experiments that vanadium compounds enhance insulin-mimetic activity by protein phosphorylation in the Tyrosine residues. Vanadium administration in streptozotocin-induced diabetic rats models showed a reversal in insulin resistance (Koyuturk *et al.*, 2005). The treatment established high levels of hexose activity in muscles and liver stimulating glycogen synthesis even in non-diabetic rat models (Scior *et al.*, 2010). Overall, vanadium supplementation enhanced the cellular sensitivity to insulin, glycolysis, and stimulated glycogen synthesis (Buglyo *et al.*, 2005).

### 2.4.3. Anticancer activity

Cancer cells rapidly undergo mutations such that they develop resistance to the conventional anti-cancer drug molecules, which emerge as a severe problem of concern in cancer management. Developing nanomedicine through the rational design of nanomaterials could address this issue. Vanadate is reported to modulate several essential genes involved in cell division, such as p53, tumor necrosis factor-alpha (TNF-α), nuclear factor-κB (Chen *et al.*, 1999), etc. Vanadate showed a dose-dependent effect on the protein and mRNA expression levels of TNF-α production in Raw264.7 cells (Ye *et al.*, 1999). Considering the results of vanadate in modulating the genes involved in cell division, its potential for development as a future for nutritional chemoprevention is underway (Ray *et al.*, 2007). The influence of vanadium pentoxides in inflammation and the immune response is studied through genome-wide analysis using human lung fibroblasts that identified potential therapeutic gene targets (Ingram *et al.*, 2007). In addition, vanadium compounds also exhibit antitumor activity in cell culture models (Evangelou, 2002). Vanadate has proven to have a higher affinity towards adipose tissue (Kawabe *et al.*, 2006) and hence exploited to understand the possibility of using the same for breast cancer management. It has been proven in a case-controlled human clinical trial that women who had significant amounts of vanadium in their urine were less prone to develop breast cancer towards later stages of their life (Tang *et al.*, 2012). Industrial level exposure to vanadium is reported to cause carcinogenic effects in people working in such environments (Byrne and Kosta, 1978). However, the influence of any material on the body is a resultant of the concentration of the active substance reaching the site. Moreover, many chemotherapeutic agents are cytotoxic in nature; a toxic substance in minimal quantity is often used as a treatment modality against various physiological conditions.

### 2.4.4. Antimicrobial potential of nano vanadium pentoxide

The prevalence of nosocomial infections in patients undergoing surgical processes in hospitals is a severe problem of concern to humans. Improper catheter sterilization increases the chances of spreading infections among patients. These infections, over time, result in biofilm formation with a consortium of multi-drug resistant bacteria, which make the problem very difficult to handle. In recent years engineered Nanoparticles (NP's) with progressive antibacterial efficacy, used to tackle various bio-medical issues and used as efficient coating agents over prosthetic surgical instruments, bone, and dental implants (Wagner *et al.*, 2006) to prevent the risk of implant-associated infections. These nanostructures over the implant surfaces reduce the possibility of bacterial adhesion and lower the chances of microbial contamination by generating ROS inside the bacteria. Many researchers discovered nanomaterials like silver nanofibers, titanium nanotubes, graphene sheets, zinc oxide, copper oxide, selenium nanoparticles to be used as efficient implant coatings against biofilm formation in prosthetic implants (Dizaj *et al.*, 2014). Reports state the efficacy of silver as a component in wound dressing materials to prevent ectopic bacterial infections. In addition to the above said medical applications, the NP's are used as components in antibacterial paints and tiles. Reports also state the activity of vanadium nanowires, with an antifouling activity, attributed to their intrinsic brominase and haloperoxidase like activity (André *et al.*, 2011). The vanadium nanowires reported inhibiting microbial growth over the surface of water-submerged parts in ships by coating with vanadium paints by generating ROS (Natalio *et al.*, 2012). In general, nanowires and other nanostructures with sharp edges are likely to be more destructive, attributed to their shape, that allows them to pierce the bacterial membranes to elicit productive antibacterial activity (Slomberg *et al.*, 2013).

# CHAPTER-3

# 3 MATERIALS AND METHODS

This chapter details various materials and methods used for the synthesis, characterization, and the biological interaction of vanadium nanoparticles. The details on the synthesis of Vanadium pentoxide nanoparticles (Vn) and methodology used to elucidate the structural property such as size, shape, surface charge, functional groups, oxidation state, and sample purity are described. The biological interactions of Vn through various *in vitro* and *in vivo* models are also presented in this chapter.

## 3.1. Chemicals and reagents

Vanadium oxy-chloride, benzoyl alcohol, sodium hydroxide, pyrogallol, Trizma base, Tris - HCl of analytical grade were purchased from Merck, India. Cell culture grade reagents such as DMEM high glucose, phenol-red free DMEM, fetal bovine serum (FBS), 0.25 % trypsin-EDTA, MTT reagent, antibiotic/antimycotic solution, trypan blue, phosphate-buffered saline, and staining dyes - propidium iodide, DAPI, ethidium bromide, Hematoxylin & eosin were obtained from Himedia, India. LysoTracker Red™ and TMRM dyes were from Invitrogen, USA. $H_2$DCFDA reagent from Invitrogen cat # C6827). JC-10 dye, Annexin - V-FITC assay kit, and actin stains were from Thermo Fischer Scientific (USA). Rhodamine - phalloidin (cat. numb: R415) and Alexa Fluor 488 (cat. numb: A12379). Hoechst dye 33242 were from (Invitrogen, USA). cDNA kit from Fisher Scientific and Power SYBR® Green PCR Master Mix from Life Technologies, CA. Western blot reagents such as acrylamide, sodium dodecyl sulfate (SDS), bis acrylamide, Tris-Cl, NaCl, EDTA, TEMED, Triton X-100, Phenyl Methane Sulfonyl Fluoride (PMSF P7626) and protease inhibitor cocktail (P8340) were from Sigma. BCA Protein Assay kit from Thermo Scientific (23225). PVDF membrane from Merck, Millipore. LC3B rabbit primary antibody (Cell Signalling Technology 2775s), HRP conjugated Goat anti-rabbit secondary antibody (Invitrogen 65-6120), and GAPDH anti-mouse antibody raised in Rabbit (Abgenex 10-10011) and secondary antibody (Invitrogen 61-6520). The Enhanced

Chemiluminescence reagent (ECL) was purchased from Millipore (WBKLS0500). Obtained Lipofectamine LTX from Invitrogen, (#15338-100), and G418-Geneticin® from Invitrogen, (#11811-031).

## 3.2. Methods Adopted

### 3.2.1. Synthesis of Vanadium Pentoxide nanoparticles (Vn)

The synthesis followed a hydrothermal method utilizing Vanadium oxychloride ($VOCl_3$) as a precursor and benzoyl alcohol as a solvent in a 1:40 (v/v) ratio, premixed in a round bottom flask for 20 min at room temperature. Transferred the flask into an oil bath with a pre-set temperature between 110 to 120 °C and reflexed with continuous condensation and constant stirring for four days. The reaction stopped once a thick dark grey precipitate obtained. Washed the precipitate three times with absolute alcohol and subsequently with ultrapure water. Dried the precipitate overnight in an oven, pre-set at 60-70 ºC. Subsequently, ground into a fine powder and finally, calcined at different temperatures in the range 350, 570 and 650 ± 10 ºC for 2 h with a ramping rate between 0.5 to 1.5 ºC $min^{-1}$. The calcination temperature was optimized as 375 ºC and 572 ºC to yield vanadium nanoparticles (Vn) as a fine yellow powder and was termed as vanadium nanospheres (VnNs) and vanadium nanoplates (VnNp) respectively.

### 3.2.2. Physico-chemical characterization of Vn

The synthesized VnNs and VnNp were characterized for their size, shape, oxidation state, surface charge, and phase purity using the following methods and techniques.

#### *3.2.2.1. Thermogravimetry and differential scanning calorimetry*

The thermal characteristics, including phase transition temperature and the rate of decomposition of compounds present in the samples, were studied by performing simultaneous thermogravimetry-differential scanning calorimetry analysis.

10mg of the synthesized dark grey, intermediate product placed in aluminum pans were used for the study. Then, samples were heated from 37ºC to 1200ºC at a ramp rate of 10ºC/min. The instrument used was SDT-Q600 (Simultaneous DTA-DSC), TA Instruments Inc.

#### *3.2.2.2. Transmission electron microscopy (TEM)*

Determined the particle size using a High-resolution TEM, JEOL 2100significantlyworking with 200 kV. The diffraction mode determined the Selected Area Electron Diffraction (SAED) pattern. The image acquisition and processing were made by Gatan US1000 charge-coupled device (CCD) camera and Gatan and Inc. Digital Micrograph software. 1 mg/ml ethanol dispersed vanadium samples, dropped and dried onto copper TEM grids, and subsequently imaged.

#### *3.2.2.3. X-ray diffraction (XRD)*

Supported the sample phase analysis with a D8 Advance model machine (Bruker AXS, Germany) using radiation of Cu Kα. Operated at 40 kV and 30 mA, and 4º/ min scan speed. The peaks at the specified intensity represent the diffraction pattern of x-rays from different planes of the sample. The International center for diffraction data (ICDD) database has all the patterns of crystalline samples with the standard data documentation values given as Powder diffraction files (PDF).

#### *3.2.2.4. X-ray photoelectron spectroscopy (XPS)*

Binding energies of vanadium and oxygen in vanadium pentoxide analyzed with Auger, X-Ray source in a MULTILAB 2000 Base system, Thermo Scientific. Works with Mg/Al (300/400 W), electron Gun with spot size < 50 mm diameter and CRR (Constant Retard Ratio), and CAE (Constant Analyser Energy) detectors.

### *3.2.2.5. Fourier-transform infrared (FTIR) spectroscopy*

Performed the functional group characterization in the samples using the KBr method. The spectra between 400–4000 cm$^{-1}$ were recorded using Cary 600 from Agilent Technologies operating in the transmittance mode. In this technique, the incident IR rays allowed transmit through the sample towards a mirror and the transmitted rays collected and measured at the detector. Each functional group denotes a characteristic peak corresponding to specific wavelengths.

### *3.2.2.6. Raman spectroscopy*

The structural characterization of the samples was performed using Confocal Raman spectroscopy. Raman analysis was done with a WITec Alpha 300R (Germany) Confocal Raman spectrometer with a 532 nm laser source.

### *3.2.2.7. Energy dispersive x-ray spectroscopy (EDS)*

Elemental composition was analyzed with an EDS analyser (AMETAK, EDAX, USA) coupled to an FEI- Quanta 200, Scanning electron microscope, Netherlands).

### *3.2.2.8. Zeta potential (ζ) analysis*

Surface charge of vanadium-based Np's measured with Zetasizer Nano ZS (Malvern USA), Zeta potential analyzer, with V4.2 software from DTS Nano. 1 mg/ml stock solution of NPs dispersed in water, from which 100 µl diluted to 3ml and used for the test.

## 3.2.3. Methods adopted for biological characterization

### *3.2.3.1. Endotoxin detection*

The presence of any possibility of endotoxin content in the synthesized vanadium NPs assessed using an Endosafe kit (PTS, Charles River, USA). Any endotoxin in the sample will react with Limulus amebocyte lysate present in the kit to form a firm gel clot, which directly indicated the amount of endotoxin present. The assay used endotoxin-free water to make a stock solution of 100 μg/ml of Vn. We have analyzed 25 μl of the sample with a PTS portable spectrophotometric reader. Readings were expressed as EU/ml.

## 3.2.4. *In vitro* interactions of 'Vn' with bacterial systems

### *3.2.4.1. Bacterial culture maintenance and vanadium treatment*

Gram-negative (*E. coli)* and Gram-positive *(S. Aureus*) bacteria cultured in Luria-Bertani broth (LB) were used as a model bacterial system. The cultures were maintained in an incubator shaker at 37 °C. Overnight grown cells were treated with appropriate concentrations of VnNs and VnNp, harvested the cells via centrifugation at their exponential phase. The cells were washed twice in sterile 1X PBS solution and removed residual culture media by centrifugation and suspended the pellet in PBS. Quantified the bacterial growth by optical density measurements at 600 nm in a UV 1601 Visible Spectrophotometer (Shimadzu, Japan, Lambda 25, PerkinElmer, Singapore). The bacterial seed suspension contained $1\times10^7$ colony forming units (CFUs).

### *3.2.4.2. Scanning electron microscopy*

Bacterial cells at their exponential phase of growth treated with Vn (100 mg/ml) and incubated, 37 °C for 24 h. Fixed the cells in 4 % paraformaldehyde (PFA) for 30 min in ice and subsequently washed in a series of ethanol gradients from 10 % to 100 %. Finally resuspended in 100 % ethanol solution and a drop of bacterial suspension were placed over clean glass coverslips, air dried, and mounted on a metallic stub using double-sided carbon tape, sputter-coated with gold for 1 min (Hitachi E1010, Japan). They were examined under an FEI Nova nano SEM-450, operating at an accelerating voltage in the range of 0.5-30 kV.

#### *3.2.4.3. Raman Spectroscopy*

Raman signals from the bacteria were recorded using a WITec Alpha 300R (Germany) Confocal Raman Spectrometer with a 532 nm laser source. For which, ten μL of the fresh bacterial pellet from VnNs and VnNp treated and untreated cells placed on tin-coated glass slides, instantaneously air-dried and analyzed. The samples kept at the pre-set focal point with a laser beam of 10 mW and 0.3 nm vertical resolution by the manufacturer. The Raman spectra from the samples obtained in the 400 – 2,000 $cm^{-1}$ range. Ten spectra collected from each sample with an integration time of 20 s for each spectral acquisition averaged to obtain the final spectra.

### 3.4.3 Cell Culture maintenance and vanadium treatment

MDA-MB-231 cells and L929 cells were kind gifts from RGCB, Trivandrum. Culture maintained in DMEM appended with 10 % FBS with anti-anti A solution in a humidified 5 % $CO_2$ incubator set at 37 °C. Replaced the cell culture medium on every alternate day and subcultured on reaching 80 % confluence, with 0.25 % trypsin-EDTA. All reagents for cell culture maintenance procured from Himedia unless otherwise stated. Biosafety cabinet with laminar airflow from Mark Air particulars, India. $CO_2$ incubator and refrigerated centrifuge from Eppendorf, USA.

A stock solution of 1 mg/ml vanadium Np's in sterile PBS sonicated for 10 min and prepared fresh before each experiment to ensure uniform distribution in the cell culture media. The cells exposed to working solutions of 100, 50, 25, 12.5, and 6.125 μM of VnNs for different times of 4, 24, and 48 h.

### 3.2.5. *In vitro* Nano-bio interaction studies on cells

Cell interaction studies like cellular uptake, cell viability, mitochondrial activity, mitochondrial membrane potential, free radical production, lysosomal activity, lysosomal membrane stability, autophagy induction, inhibition on cell cycle progression, cell migration, colony formation, mechanism of cell death in MB-231 and antimicrobial activities on representative microorganisms were studied with VnNp and VnNs.

#### ***3.2.5.1. Cell viability assay***

MTT assay evaluated the percentage of cell viability with various concentrations of VnNs. Seeded MB-231 and L929 cells at 1 X $10^4$ cells per well density in a 96 well culture plate and maintained for 24 h at 37 $^{\circ}$C and 5 % $CO_2$ (ambient conditions). Used 1 mg/ml VnNs dispersed in PBS, pH at 7.4 as a stock solution of 0.5 mM. The healthy cells maintained under similar conditions served as the control, and 100 μL of a particular concentration of VnNs in media served as the treatment group. Maintained for 24/48 h under similar conditions and then followed standard instructions from Invitrogen. Treated with 0.5 mg/ml MTT solution, incubated in the dark for four h, removed the reagent, and dissolved the formazan crystals in DMSO. Synergy H1 hybrid microplate reader from Bio-Tek with absorbance measured at 570 nm was Used. The percentage relative cell viability was calculated and normalized to control values.

#### ***3.2.5.2. Particle uptake by flow cytometry***

Uptake of vanadium NPs by the cells were analyzed using flow cytometry, by monitoring the relative cell population in the forward scatter (FSC) and side scatter regions (SSC). Light scattering through the SSC pattern indicates the size of the cells, and the FSC pattern indicates the granularity of cells. Normally, cells uptake nanoparticles and result in increased granularity and a corresponding increase in SSC. The experiment used one × $10^6$ cells/well on six-well plates. Overnight incubation and on the subsequent day exposed to 50 μM of VnNs for 4 h. Cells centrifuged at 1200 rpm and suspended in 500μl PBS and analyzed instantly in a BD - C6 accuri flow cytometer with 10,000 events counted per each experimental group.

#### *3.2.5.3. Cell processing for transmission Electron Microscopy (TEM)*

All solvents and chemicals in cell processing for TEM analysis purchased from ProSciTech, Australia, unless otherwise mentioned. Cells treated with VnNs pelleted by centrifugation at 1500 rpm and transferred to sterile PCR tubes. Followed by 0.1 M cacodylate buffer (pH 7.4) washes and fixated in 2 % PFA in the buffer and 2.5 % glutaraldehyde for 2 h. Fixed in 1 % osmium tetroxide for 2 h at 37 °C and washed. Samples were dehydrated in a sequence of ethanol concentrations (from 50 to 100 %) for 10 min intervals and finally in absolute acetone for 30 minutes. Infiltrated through a series of increasing concentrations of acetone: Spurr's resin overnight and finally infiltrated twice through 100 % fresh Spurr's resin and allowed to polymerize in an oven pre-set at 70 °C for 48 h to obtain resin-embedded cell blocks. The blocks sectioned using a diamond knife fitted to an ultra-microtome (Leica) into 70-90 nm thick sections and transferred into copper grids. TEM analysis performed using JEOL-JEM 1010 at a working voltage of 80 kV with magnifications from 15-30,000 X.

#### *3.2.5.4. Expression vectors and yielding stable cells*

Dr. Masayuki Miura gifted a sensor for activated caspase 3 with nuclear localization signal (SCAT3-NLS) vector, Tokyo University, Japan. Dr. Tamotsu Yoshimori gifted the pEGFP-LC3 plasmids (Addgene plasmid # 21073). Used Lipofectamine LTX for all the cellular transfections (Invitrogen, #15338-100) and followed the protocol and instructions from the manufacturer. Stable cells expressing the transgene were selected by 500 μg/ml of the antibiotic G418-Geneticin® (Invitrogen, #11811-031) for three to four weeks. Cells with homogeneous transgene expression sorted and expanded using Aria III FACS from BD Biosciences.

### *3.2.5.5. Imaging EGFP-LC3 and TMRM*

Cells stably expressing EGFP-LC3 were grown on 96-well optical bottom culture plates and stained with 100 nM TMRM prior to VnNs treatment. Prepared VnNs in phenol-red free DMEM with 5 % FBS at appropriate concentrations supplemented with 20 nM TMRM. HBSS supplemented with 20 nM TMRM served as a positive control. Sequentially scanned the cells using a Leica Confocal laser microscope (TCS SP8 WLL, Wetzlar, Germany). Used excitations of 488 nm and emission at 500-550 nm using GaAsP detectors for imaging EGFP-LC3. In addition, for TMRM imaging, an excitation of 561 nm, and an emission of 600 ± 25 nm was used. Used an inbuilt Leica Microsystems incubation chamber with optimal humidity, 37 °C and 5 % $CO_2$ to maintain live cells during imaging.

### *3.2.5.6. Protein extraction and western blot analysis*

VnNs pretreated MDA-MB-231 cells were harvested in ice-cold PBS and pelletized at 6500 rpm for 3 min at 4 °C. The lysis buffer contained 50mM Tris-Cl, 1mM EDTA, 1 % (v/v) Triton X-100, 150 mM NaCl, 1mM Phenylmethanesulfonyl fluoride (PMSF P7626) and protease inhibitor cocktail (Sigma P8340) and used to incubate cells in ice for 30 min followed by 10 min centrifugation at 10,000 rpm, 4 °C. Collected sample supernatants and determined protein concentrations through the BCA Protein Assay kit (Thermo Scientific 23225). Briefly, 25 µl of Bovine Serum Albumin (BSA-Sigma) in the range of to 0 -1 µg/ml concentration used as protein standards. The sample protein solutions diluted in a 1:20 ratio with water and incubated with BCA reagent for 30 min at 37 °C. The absorbance at 570 nm taken to plot the standard graph. The concentration of the unknown protein samples calculated from the standard graph by using 10 µl of the diluted samples from each treatment condition. Equal amounts of boiled, cooled protein samples at a concentration of 30 µg/well in Laemmli buffer were loaded onto 12 % SDS - polyacrylamide gel run for 2 h (initial 30 min at 60 V followed by 110 V for 1.30 h) and transferred into methanol activated polyvinylidene difluoride (PVDF) membrane by following the standard protocol as per manufacturer's instructions.

Used 5 % skimmed milk for blocking the protein-blotted membranes for 1h at 37 °C, and followed PBST buffer washes for 3 times (0.1 % PBS-Tween 20) at 5 min intervals. Used primary antibodies that were diluted 1:1000 and secondary antibodies 1:5000 for western blotting (WB). Probed overnight at 4 °C with primary rabbit antibody, LC3B (Cell Signalling Technology 2775s), and the membrane was washed 3 times in TBST. Subsequently incubated with 1:500 diluted HRP conjugated Goat anti-rabbit secondary antibody (Invitrogen 65-6120) for 1hr at room temperature, and washed in TBST (three times). GAPDH anti-mouse antibody raised in Rabbit (Abgenex 10-10011) and secondary antibody (Invitrogen 61-6520) served as the loading control. The bands were developed using ECL reagent (Millipore WBKLS0500) and observed under the chemiluminescence mode in a BIO-RAD ChemiDoc XRS instrument. The protein bands were quantified using Quantity One software.

### *3.2.5.7. Lysosomal staining with LysoTracker Red™*

MB-231 cells seeded onto sterile coverslips at an initial seeding density of 1X10$^5$ cells and allowed to grow overnight. Treated with VnNs at appropriate concentrations and stained with lysosome specific LysoTracker Red™ dye (Invitrogen, USA). The cells without any nanomaterial treatment served as the untreated controls. The average maximum intensity from each field was obtained from the z-stack of 8 slices by selecting average mean fluorescence intensity from at least ten different regions of interest (ROI) at a constant laser exposure of 300 ms on both control and treatment groups. The imaging was carried out using a 540-550 nm BP excitation and 575-625 nm BP emission filter with a 570 nm dichromatic mirror using an IX83, Fluorescence Microscope by Olympus, Japan. Contained an inbuilt metal halide lamp (X-Cite, series 120PCQ) and a cooled CCD camera (XM10, monochrome, Olympus). Image analysis performed using CellSens Imaging software (Olympus).

### *3.2.5.8. Lysosomal membrane integrity by Acridine orange*

Lysosomal destabilization in the presence of VnNs was analyzed using a lipophilic, cationic fluorochrome acridine orange (AO). The dye is capable of permeating cells and lysosomal membrane structure, which differentially stains cytoplasm and acid vesicles upon excitation with blue light. Lysosomal acidic vesicles have a high concentration of $H^+$ ions allowing the protonation of dye within and emit orange fluorescence, whereas the dye in the cytoplasm emits green fluorescence. For the experiments, cells seeded at an initial density of $1x10^5$ cells/coverslip and allowed to incubate and attach overnight. On a subsequent day, cells exposed to VnNs at 50 and 25 μM for 24 and 48 h. Post incubation, the cells stained with 1 ml AO solution (2μg / ml in PBS) for 15 min at 37 °C and washed with PBS. Micro graphed with an IX83 Olympus Fluorescence Microscope modified with a personalized blue excitation (470-495 nm), red emission (575-625 nm) BP filters, and 570 nm dichromatic mirror.

### *3.2.5.9. Mitochondrial Membrane potential (MMP) assay with JC-10*

A qualitative analysis on the mitochondrial health by analyzing its membrane potential was achieved through fluorescence microscopy with a lipophilic JC-10 (5, 5′, 6, 6′-tetrachloro-1,1′,3,3′-tetraethylbenz-imidazolyl-carbocyanine-iodide) dye, (ENZ-52305) from Enzo Life Sciences. The dye aggregates within intact mitochondria and emits red fluorescence, and it remains as monomers in the cytoplasm and gives out green fluorescence from cells with altered mitochondrial membrane potential. Briefly, initially seeded the cells at a concentration of $1X10^5$ cells/well and upon 70 % confluence; the cells exposed to 50 & 25 μM of VnNs for 24 h. Subsequently, added 1μM JC-10 to every well, towards the end of the exposure, and kept undisturbed at 37 °C for 20 min. Washed in PBS and the red fluorescence intensity from treated cells were visualized using a personalized microscope, modified the excitation-emission with a blue excitation (470-495 nm) and red emission (575-625 nm) BP filters with a 570 nm dichromatic mirror, equipped in an Olympus Fluorescence Microscope (IX83, Tokyo, Japan).

### 3.2.5.10. *MMP assay with JC-10 through flow cytometry*

Cells seeded into six-well plates at an initial seeding density of 1 x $10^6$ cells/ml. Treated with specific concentrations of VnNs and subsequently trypsinized, recovered, and resuspended in 500 µL of 1X JC-10 (ENZ-52305) dye-loading solution kept at room temperature and allowed to incubate in dark room temperature for 20 minutes. Cells were directly analyzed with a BD Aria III, FACS with FL1 channel for green fluorescence, and FL2 channel for orange to red fluorescence.

### 3.2.5.11. *In vitro antioxidant activity using pyrogallol assay*

Pyrogallol (Merck 06931), a redox-sensitive dye, undergo rapid decomposition in Tris- HCl buffer solution to give its product purpurogallin and highly reactive superoxide radicals. The *in vitro* rate of inhibition on Pyrogallol auto-oxidation in the presence of VnNs performed through kinetic studies on a UV-Vis spectrophotometer, UV-1800 Shimadzu in Tris – HCl buffer system. Adopted the protocol from the pyrogallol assay experiment (Marklund and Marklund, 1974; Li, 2012).

### 3.2.5.12. *A cellular antioxidant activity using DCFH-DA assay*

Reactive oxygen species (ROS) generated in cells subsequent to VnNs exposure was measured using 2′7′-dichlorofluorescein diacetate DCFH-DA reagent (Invitrogen cat # C6827). Generally, cell membranes are permeable to the esterified forms of the dye, and they undergo deacetylation by the activity of intracellular esterase. Dye within the cells gets oxidized with intracellular ROS, converting the dye into 2′,7′-dichlorofluorescein (DCF), which possess green fluorescence. The signals were detected using spectrofluorimetry as well as fluorescence microscopy. For the experiment, seeded 2x$10^4$ cells / well of MB-231 cells on 96 well culture plates and allowed to grow overnight. The VnNs treatment followed similar treatment concentrations as that used for the MTT assay, and 10µM $H_2O_2$ treatment for 20 minutes served as a positive control. The assay accomplished with the manufacturer's instructions. The ROS levels from untreated cells maintained under ambient conditions taken into account in order to normalize the treatment values and readings from wells with all the said reagents and vanadium except cells obtained to minimize the background interference and to normalize the readings. The fluorescence intensity was analyzed in a Synergy H1 96 well microplate reader from Bio-Tek at excitation-emission wavelengths of 492 and 527 nm. Captured cellular fluorescence images with an IX83, Olympus Fluorescence Microscope (Tokyo, Japan).

### *3.2.5.13. Amplex® Red assay for $H_2O_2$ detection*

Amplex® Red (10-acetyl-3, 7-dihydroxyphenoxazine), Invitrogen (Cat # A22188), is a highly sensitive dye that measures the presence of $H_2O_2$ in VnNs treated cells. The amount of $H_2O_2$ present in the treatment condition deducted from the red-fluorescence obtained from the product, resorufin. Quantified with a Synergy H1, microplate reader from Bio-Tek with a fluorescence excitation at 571 nm and emission at 585 nm. Strictly followed procedure for cell treatment and fluorescence acquisition as per the manufacturer's instructions.

### *3.2.5.14. Cell cycle analysis*

Cell concentration at $1x10^6$ cells per well was plated in six-well plates and allowed to attach overnight. The cells treated with 25 and 50µM of VnNs subsequently incubated for 24, 36, and 48 h and recovered the cells following centrifugation at 1000 rpm for 5 min to obtain a cell pellet. Fixed in ethanol and stained in buffer with 200mg propidium iodide PI (Sigma), 2 mg DNAse-free RNAse-A (Sigma), 0.1 % (v/v) Triton X-100, containing PBS for 15 min at 37 °C. Further, analyzed instantly and measured variations in DNA content from the differences in fluorescence of PI. Flow analysis counted 10,000 events in a C6 Accuri™ flow cytometer.

### *3.2.5.15. Assay for cellular apoptosis*

Measured the levels of cells at various stages of cell death upon treatment with VnNs were quantified using Invitrogen™ eBioscience™ Annexin V Apoptosis Detection Kit. Here, Annexin V, a cell impermeable 35-36 kDa protein having a high affinity for phosphatidylserine, used to stain early apoptotic cells, and Propidium Iodide dye is used on the other hand to stain only cells with permeable and ruptured membranes. For the assay, seeded the cells at 1 X $10^6$ cells / per well density onto six-well plates and overnight grown. Subsequently, treated the cells with appropriate concentrations of VnNs and retained for 24 and 48 h. Stained the recovered cells and with Annexin V and PI by following the manufacturer's instructions. Analyzed with BD FACS Aria III (BD Biosciences) with an excitation of 488 nm laser to detect FITC labeled cells in the FL-1 channel with a 525/30 BP filter. The PI labeled cells were detected in the FL-2 channel with a 575/30 BP filter. Performed standard gating with single-stained and unstained cells and counted 10,000 events on each set of experiments. Data analysis was done using FlowJo software (Tree Star Inc.).

### *3.2.5.16. Actin staining for cytoskeletal morphology*

Actin filaments play essential roles in maintaining the cytoskeletal architecture of cells. Phalloidin, a peptide toxin isolated from Amanita phalloides, has high affinity and selectivity for cytoskeletal F-actin and is hence, used to tag fluorescent rhodamine molecules to visualize the architecture of actin arrangements. Cells at an initial seeding density of 1x$10^6$ cells / well cultured over sterile coverslips (Blue star 10 mm) and exposed to 50 & 25 µM of VnNs for 48 h. Fixed the cells for 15 min in 3.7 % PFA and permeabilized with 100 % methanol for 15 min at −20 °C. Stained nuclei with DAPI, washed three times in sterile PBS and followed membrane blocking with 10 % BSA in PBS for 30 min at 37 °C. Subsequently stained with Rhodamine–phalloidin (Thermo Fisher, Cat. # R415) or Alexa Fluor 488 phalloidin (Thermo Fisher cat. # A12379) for 15 minutes at a dilution of 1:100 in sterile PBS. Observed the cells with an N-STORM super-resolution confocal microscope using a TRITC filter.

### *3.2.5.17. Nuclear morphology staining with DAPI*

Analyzed the chromosomal condensation, as an indicator of apoptosis using DAPI stain. Fixed the cells incubated with 48 h of 50 µM VnNs in 4 % PFA and subsequently stained with 1µg/ml DAPI (Invitrogen Cat. # D1306, USA). Incubated for 5 min and followed the manufacturer's instructions. Washed in PBS, observed under an N-STORM super-resolution confocal microscope using a DAPI filter.

### *3.2.5.18. Preparing cells for scanning electron microscopy*

The surface morphology of VnNs treated cells were evaluated using SEM analysis. Here, the cells were grown over adherent glass coverslips (Blue Star, India) exposed to 50 µM of VnNs, maintained for 48 h at ambient conditions. Fixed the cells in 1 % glutaraldehyde solution for 2 h and PBS washed. They were dehydrated in a series of ethanol concentrations from 30 % to absolute 100 % alcohol. Further, treated in iso-amyl acetate and dried in a critical control point (CCP) Hitachi drier. Lastly, mounted the samples on metallic stub with carbon tape and sputter-coated with gold for 1 min (Hitachi E1010, Japan) to view under SEM (FEI, Quanta 200, instrument Netherlands).

### *3.2.5.19. High-throughput screening for caspase activation*

MB-231 cells expressing SCAT3-NLS were maintained in 96 well BD black culture plates with a clear optical bottom (Becton Dickinson, Biosciences, cat # 353219) at ambient conditions. They were treated with working concentrations of VnNs in phenol-red free complete medium. Micrographed with BD Pathway™ 435 Bio imager (Biosciences, USA). Used a combination of 438 ± 24 excitations, 458 Long Pass (LP) dichroic mirror, and 483 ± 32 emission filters for Enhanced cyan fluorescent protein (ECFP) fluorescence resonance energy transfer (FRET). In addition, an enhanced yellow fluorescent protein (EYFP) used 438 ± 24 excitations, 458 LP dichroic mirrors, and 542 ± 27 emission filters. They were imaged using a 20X objective with 0.75 NA.

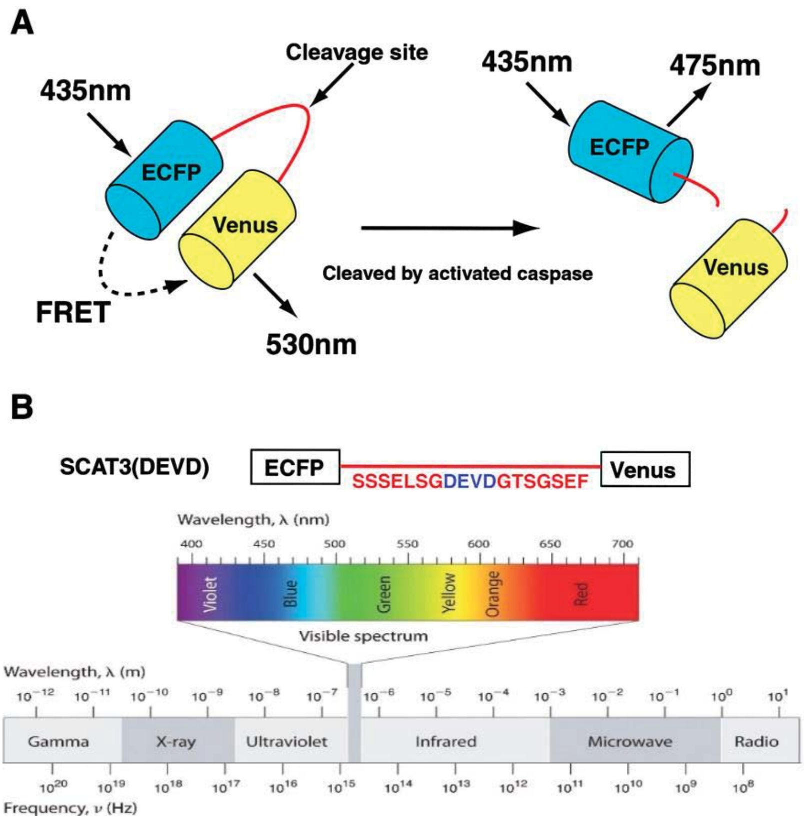

**Figure 3.1 Sequence of SCAT3- DEVD**. Adopted from (Takemoto *et al.*, 2003)

### *3.2.5.20. In vitro cell migration assay*

MB-231 cells at 5 X $10^5$ cells per well concentration were maintained in 30 mm dishes to attain confluence for 24 h. Carefully scraped the cells from one side to the end, having a constant width. Washed to remove floating cells, treated with different concentrations of VnNs, and kept undisturbed at ambient conditions for various time points. Further, cell migration across the inflicted wound area imaged with a phase-contrast microscope (Nikon) at five or more randomly selected fields.

### *3.2.5.21. Colony formation assay on MDA-MB-231 cells*

Further confirmed the anti-proliferative activity of VnNs through a colony formation assay. A colony is formed from a single cell, and the assay measures the ability of a cell to form a colony. MDA-MB-231 cells growing in their exponential phase, plated at a concentration of 500 cells/well into six-well plates. Following overnight incubation, treated with various concentrations of VnNs and maintained for 24 h. Switched the medium with a new culture medium and further incubated at ambient conditions for 14 more days. Washed the cells in PBS, followed by post-fixation in 4 % PFA, and subsequently stained in 0.5 % methylene blue for 30 min. Thoroughly washed the cells with distilled water and removed all the excess unbound dye. The plates were dried upside down and snapped with a digital camera.

## 3.2.6. *In vivo* biological interactions of VnNs

### *3.2.6.1. Animal ethics*

Carried out all the animal experiments in compliance with the Institutional Animal Ethics Committee. (IAEC approval # SCT/IAEC 243/August/2017/94). The management of all the animals and animal experiments obeyed the regulations of the Committee for the Purpose of Control and Supervision of Experiments on Animals (CPCSEA, Govt. of India).

### *3.2.6.2. Animal housing and welfare*

The Division of Laboratory Animal Sciences, of our institute, provided the animal housing and maintenance facility. Used healthy female Swiss albino mice weighing (22±3 g) for the *in vivo* VnNs interaction studies. Mice groomed in ventilated cages kept at 12 h dark and light cycles with the temperature maintained between 22 ± 2 °C and 30-70 % relative humidity. They were sustained on a pellet diet with water supplied in ad libitum. Randomly grouped the animals into six animals per experimental trial and were picric acid marked to identify individual animals within groups. Furthermore, we labeled each cage with the name of the experiment and experiment number along with the date of commencement and end date of the experiment. The female mice were acclimated and allowed to synchronize their estrous cycles, 10 days prior to the start of experiments. Routinely monitored the animals for physiological activity by cage observation. Animal handling was done humanitarian by making sure of no discomfort or suffering owing to their welfare and care.

#### ***3.2.6.3. Experimental Design and analysis***

Mice were randomly divided as vehicle control (saline) and VnNs in saline (1mg/kg body weight) injected groups of 6 animals per group. Post injection, the animals were maintained for one day, 3 days, and 21-days. The body weights of all the animals were monitored at regular intervals. Anesthetized the animals on indented days with $CO_2$ and euthanized by cervical dislocation. The blood samples were collected from the orbital sinus of all the experimental animals in BD Vacutainer® Blood collection tubes.

#### ***3.2.6.4. Analysis with blood parameters***

Blood samples analyzed for various hematology parameters such as white blood cell (WBC), hemoglobin (HGB), red blood cell (RBC), hematocrit (HCT), platelet (PLT), etc., measured using a fully automated Beckman coulter hematology analyzer DxH 500, USA. Serum samples analyzed for various biochemical parameters such as urea, creatinine, total cholesterol, alanine transaminase (ALT), aspartate aminotransferase (AST), etc., and analyzed using fully automated Beckman coulter biochemical analyzer AU 480, USA.

#### ***3.2.6.5. Urine analysis for vanadium elimination***

Collected the urine samples from the animals at all the possible time intervals until the end of the observation period. The presence of vanadium in urine samples was analyzed using a WITec Inc. Confocal Raman microscope (alpha 300R, Germany). The assembly maintains a laser beam always concentrated on the sample with a 60X immersion objective (NA = 1.0). Used a 532 nm excitation laser with a 1cm$^{-1}$ resolution. Obtained the spectra among 400 - 4000 cm$^{-1}$. Carried out measurements on samples placed over tin-coated glass slides by using WITec (v 2.1) software. Compared to the spectra between trials from the same mice before and after VnNs administration (n=6).

#### *3.2.6.6. Inductive coupled plasma - optical emission spectroscopy (ICP-OES)*

The technique utilizes high-temperature heating of samples in plasma, and the particles are ionized and excited to their higher energy levels. These particles emit this energy at a different wavelength and come back to the ground state. This excitation and emission profiles, depending on the property of electrons from specific elements and attributed to the characteristic of each atomic orbital. Each element emits energy corresponding to different wavelengths, and the assay enables the user to choose the best wavelength for a given element. The intensity of energy at a particular wavelength is directly related to the quantity of elements present within the sample analyzed.

Quantified the persistence of any trace levels of vanadium in the liver, kidney, and spleen by elemental analysis via ICP-OES on samples collected at different time points of post-injection. Weighed the tissue samples and acid digested for ICP analysis. Briefly, 100 mg of samples were pre-digested in 5.0 ml concentrated nitric acid ($HNO_3$, ICP grade, Sigma) followed by complete acid digestion in dilute 2 % $HNO_3$ with heating at 150 °C. Standard solutions were prepared by serial dilution of 1000 ppm Vanadium (ICP standard, Sigma) to plot the calibration curve. The analysis was carried out at three different wavelengths of 290 nm, 309, and 310 nm using ICP-OES (Perkin Elmer 5300DV, USA). Assessed the vanadium content in the organs as a measure of the spectral wavelength at 290 nm, corresponding to the presence of vanadium. Compared the results with the organ samples from the saline-injected control group to understand variances among particle distribution within organs involved in the excretion process.

### *3.2.6.7. Real-time PCR analysis on the mRNA levels of antioxidants*

The freshly collected tissue samples from the animals at different points of the study were immediately transferred into the Trizol reagent for RNA isolation. Isolated the total RNA, using TRIzol reagent (Invitrogen cat # 15596-026), quantified using Nanodrop, and around 2μg RNA was converted into complementary DNA (cDNA) using Superscript VILO cDNA kit (Thermo Fisher Scientific). Standard protocols followed for the quantitative real-time PCR (qPCR) experiments. Designed the Oligonucleotides for primers using NCBI pick primers and purchased the primers from Ocimum Biosolutions. Performed the qPCR amplification with Power SYBR® Green PCR Master Mix (Life Technologies, CA). Calculated the relative mRNA levels using ΔΔCT method with endogenous control as 18S rRNA. Achieved the reaction on a Fast Real-Time PCR instrument from CA-7900 HT, Applied Biosystems, operating with typical cycling conditions. The melting curve analysis ensured the product specificity. The primers used for the experiment are listed in Table 1.

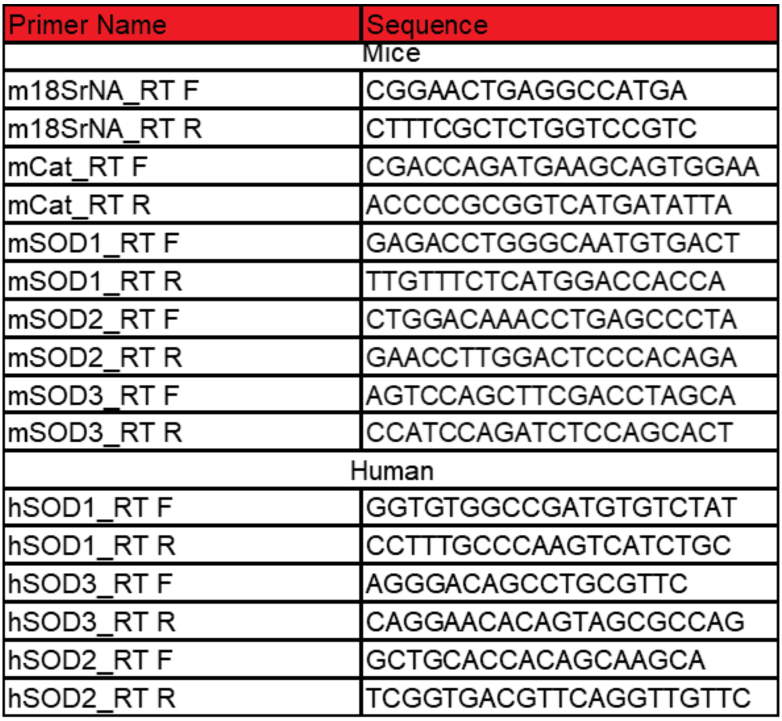

| Primer Name | Sequence |
|---|---|
| Mice | |
| m18SrNA_RT F | CGGAACTGAGGCCATGA |
| m18SrNA_RT R | CTTTCGCTCTGGTCCGTC |
| mCat_RT F | CGACCAGATGAAGCAGTGGAA |
| mCat_RT R | ACCCCGCGGTCATGATATTA |
| mSOD1_RT F | GAGACCTGGGCAATGTGACT |
| mSOD1_RT R | TTGTTTCTCATGGACCACCA |
| mSOD2_RT F | CTGGACAAACCTGAGCCCTA |
| mSOD2_RT R | GAACCTTGGACTCCCACAGA |
| mSOD3_RT F | AGTCCAGCTTCGACCTAGCA |
| mSOD3_RT R | CCATCCAGATCTCCAGCACT |
| Human | |
| hSOD1_RT F | GGTGTGGCCGATGTGTCTAT |
| hSOD1_RT R | CCTTTGCCCAAGTCATCTGC |
| hSOD3_RT F | AGGGACAGCCTGCGTTC |
| hSOD3_RT R | CAGGAACACAGTAGCGCCAG |
| hSOD2_RT F | GCTGCACCACAGCAAGCA |
| hSOD2_RT R | TCGGTGACGTTCAGGTTGTTC |

**Table 3.1. List of qPCR primers used for real-time mRNA quantification.**

### *3.2.6.8. Histopathology analysis*

The histopathology evaluation was performed on the liver, kidney, and spleen collected from different treatment and control groups. The tissue samples obtained from mice post euthanasia washed several times in normal saline and immediately transferred into 10 % neutral buffered formaldehyde (10 % NBF) to prevent tissue degradation. The NBF processed samples cut into small pieces, kept in tissue cassettes, and dehydrated in a series of isopropanol and xylene. Subsequently impregnated in molten paraffin and allowed to cool in order to obtain tissue embedded paraffin blocks. Thin tissue sections of 5 µM thickness were cut with a microtome (Leica RM 2125 RT). Drifted the sections into warm water and picked on clean poly-l-lysine pre-coated microscopic glass slides. The sections were stained with Hematoxylin (Cat # GRM236), partially de-stained with acid- alcohol and counterstained with Eosin dye (Cat # S007), named as H&E staining followed as per standard protocol. Mounted the slides in DPX to provide better optical transparency observed under a light microscope

(Olympus CX31) with Qcapture ProTM 6 software.

### 3.2.7. Statistical analysis

Carried out all the experiments in a minimum of triplicate or more, as per statements given in individual experiments, and the significance values are expressed as mean ± SD. Statistical comparison was done in the experimental test with appropriate control and was analyzed using student's - *t*-test and ANOVA multiple comparisons. In the results, 'p' values <0.05 are considered significant, and the extent of significance is shown through star notation.

# CHAPTER - 4

# 4 RESULTS

This chapter describes the overall results obtained from the present study in five sections. The first section presents details on the technique adopted for the synthesis of vanadium pentoxide nanoparticles in spherical (VnNs) and plate-like (VnNp) morphology. The second section deals with the characterization of the synthesized nanoparticles. The next section compares the antimicrobial activity of these two different forms of vanadium pentoxide nanoparticles in representative bacterial species. The third section describes various *in vitro* biological interaction studies of VnNs on triple-negative breast cancer cells. In addition, the final subsection portrays the interactions of nano vanadium in Swiss albino mice models.

## 4.1. Synthesis of nano vanadium pentoxide

Vanadium pentoxide nanoparticles (Vn) were synthesized from vanadium oxychloride and benzoyl alcohol using a hydrothermal method to obtain an intermediate product, which upon calcination gave the final products. A bright yellow colored product obtained by the end of calcination resulted in nano-sized vanadium pentoxide particles in either spherical morphology (VnNs) or plate-like morphology (VnNp). Both these particles remained stable and were highly water dispersible when subjected to ultra-sonication.

## 4.2. Physico-chemical characterization nano vanadium pentoxide

Details on the physicochemical characterization of the synthesized nano vanadium using different techniques are given.

### 4.2.1. Thermal gravimetric analysis (TGA)

TGA measures the actual mass of the sample, over different temperatures and depend on the degradation temperature of constituent components present in the initial material. The reaction intermediate, obtained from the hydrothermal reaction subjected to TGA thermal analysis, showed 97 %, 50 %, and 25 % weight reduction at 233 °C, 350 °C, and 367 °C, respectively. The decline in weight corresponds to the loss of adsorbed moieties such as water and reactant benzoyl alcohol **Figure 4. 1.**

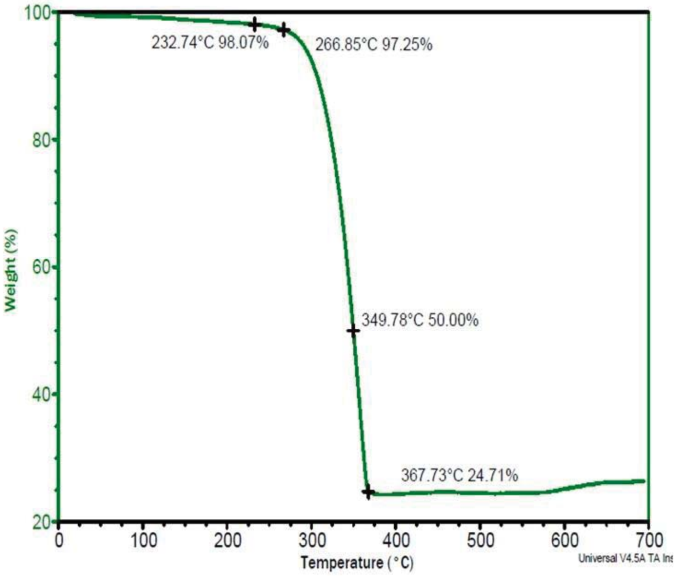

**Figure 4.1. Thermal study with TGA analysis**

### 4.2.2. Differential Scanning Calorimetry Analysis (DSC)

DSC determines the caloric values of materials, including the heat of fusion, crystallization, and glass transition. The result showed an exotherm peak at 376 °C and an endothermal peak at 572 °C and an exothermal peak at 672 °C **Figure 4.2.**

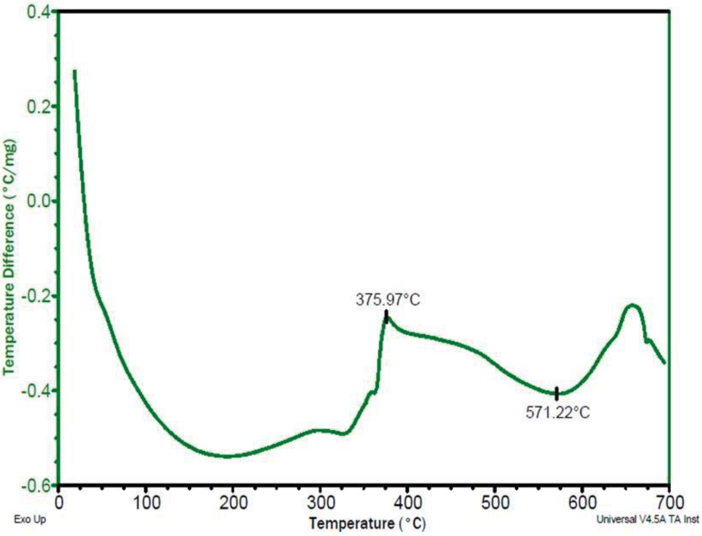

**Figure 4.2. Thermal study with DSC analysis**

## 4.2.3. Transmission Electron Microscopy (TEM)

The Size analysis of Vn using TEM revealed, VnNs with a broad size distribution range with an average size of 50 nm (**Figure 4.3 a)**. VnNp exhibited stacked plate-like morphology distribution with length ranging to several µm, while the thickness of each layer was found to be 1 nm in size (**Figure 4.3 b)**. The Selected Area Electron Diffraction (SAED) pattern in VnNs, exhibited concentric ring pattern with diffuse diffraction spots **(Figure 4.3 c)**. While VnNp showed multiple sharp spots observed as distorted rings **(Figure 4.3 d).**

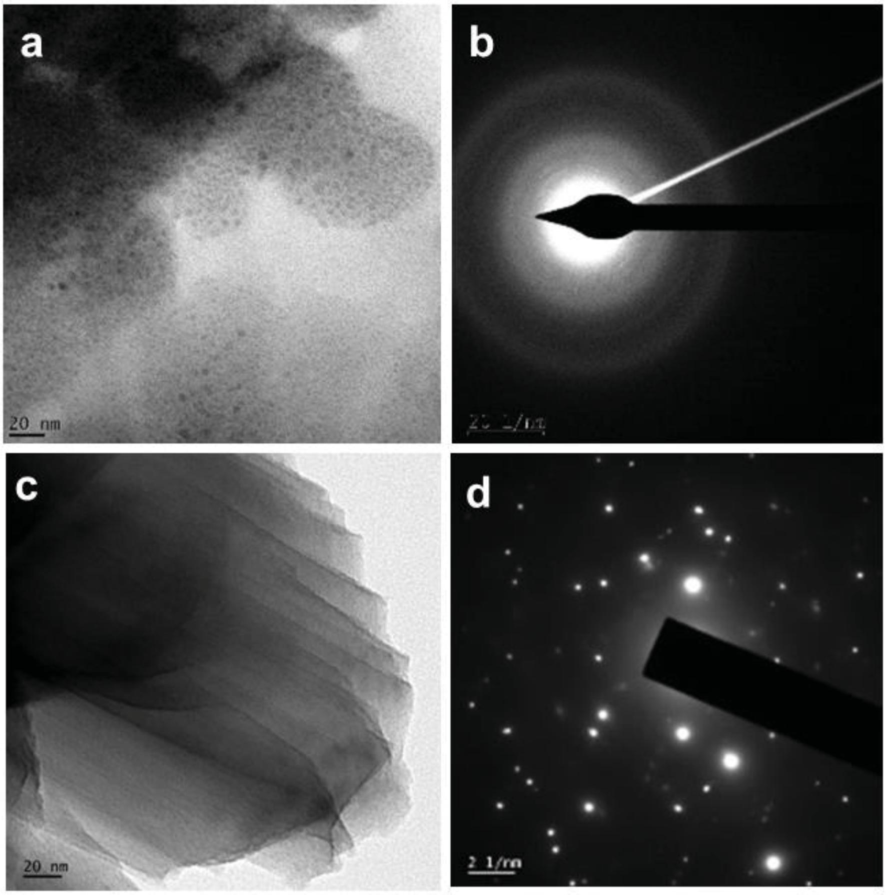

**Figure 4.3. TEM images and their corresponding SAED patterns: (a & b) VnNs and (c & d) VnNp.**

## 4.2.4. Energy Dispersive X-ray analysis EDX

The elemental analysis by EDX showed the peaks that correspond to vanadium and oxygen alone, indicating high sample purity **(Figure 4.4).**

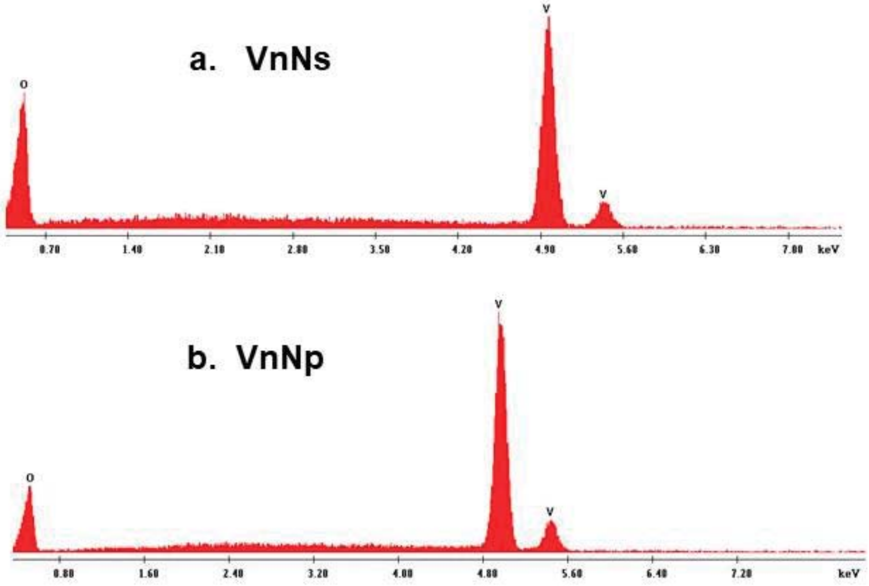

**Figure 4.4.** EDX analysis indicates sample purity in VnNs and VnNp.

### 4.2.5. X-Ray Diffraction (XRD)

Elucidated the crystal structure of VnNs and VnNp to understand the crystallographic pattern of samples through XRD. In addition, the pattern confirmed the monocrystalline, orthorhombic, sherrebanite structure for both VnNs and VnNp, and were in accordance with the PDF 00-041-1426 data. There were two predominant peaks observed at 2θ corresponding to 20 and 26 degrees, which are attributed to the preferred orientation along 001 and 110 plane, which account for the main difference in the crystal growth between the two samples **Figure 4.5**.

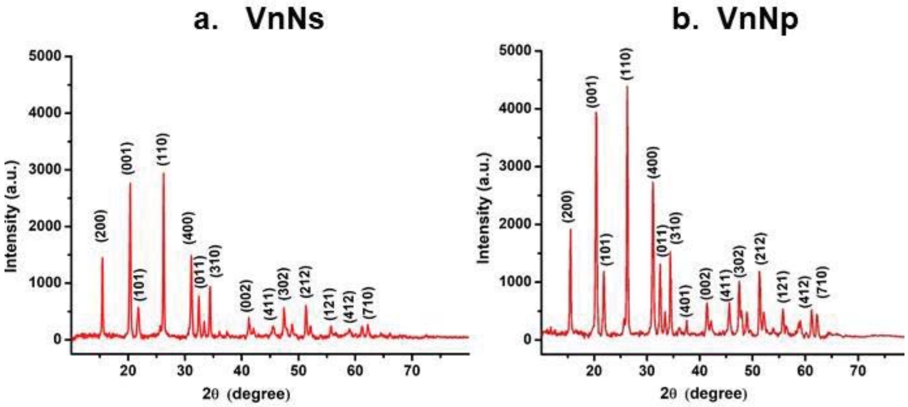

**Figure 4.5. The XRD pattern of the Vn products corresponds to the reference PDF-00-041-1426.**

### 4.2.6. X-ray photoelectron spectroscopy (XPS)

The XPS analysis gives an impression on the purity of the synthesized samples as a function of binding energy (BE), which correspond to specific functional groups. Peaks were charge corrected with C1s at 284.8 eV. BE of vanadium and oxygen analyzed from the spectra correspond to 517 eV, 524 eV, and 530 eV, demonstrating the $V2p_{3/2}$, $V2p_{1/2}$, and O1s bonds respectively. These BE agree to the +5 oxidation state of vanadium oxide **Figure 4.6.**

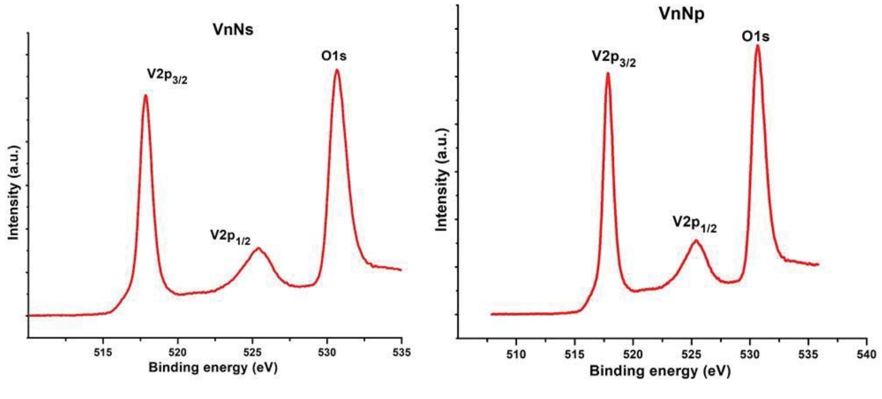

**Figure 4.6. The XPS spectra of VnNs and VnNp.**

### 4.2.7. Fourier-transform infrared spectroscopy (FTIR)

FTIR spectroscopy analysis revealed characteristic metal-oxygen stretching and bending modes. Peaks observed at 1020, 840, 678, and 536 cm$^{-1}$ matches to the V=O stretching, O–(V) vibrations, asymmetric and symmetric stretching in V–O–V bridging respectively **Figure 4.7.**

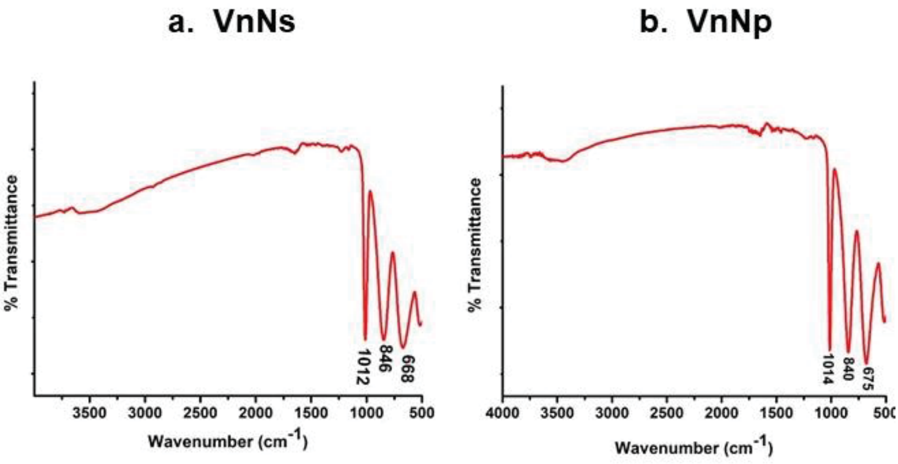
a. VnNs

b. VnNp

**Figure 4.7. The FT-IR spectra denote the typical bond formation in VnNs and VnNp.**

### 4.2.8. Raman Spectroscopy

Raman scattering elucidates the chemical structure, molecular interactions, and presence of impurities. Raman spectra shown in **Figure 4.8**, depicts characteristic crystalline vanadium-oxygen peaks at 143, 282, 406cm$^{-1}$ correspond to the bending vibrations of $O_3$–V=O, 692 cm$^{-1}$ indicating the stretching vibrations of doubly coordinated oxygen in ($V_2$–O) and 992 cm$^{-1}$ is characteristic of the stretching vibration in V=O involving the terminal unshared oxygen atom.

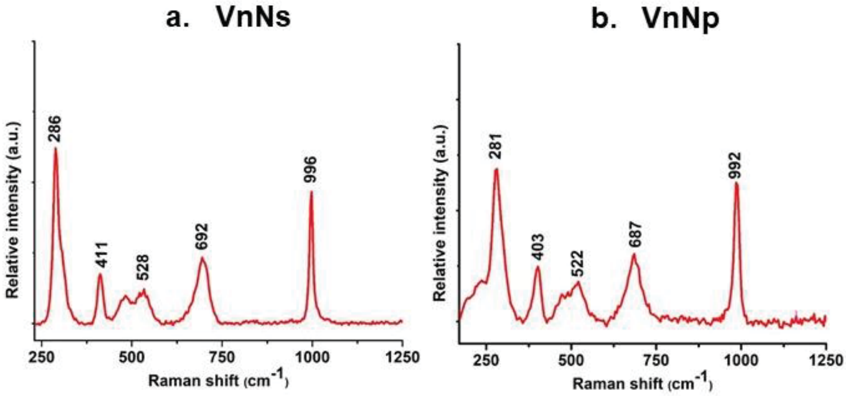

**Figure 4.8. The Raman spectra from VnNs and VnNp.**

## 4.2.9. Zeta potential analysis

The surface charges of VnNs and VnNp were obtained by using a zeta potential analyzer. The Zeta potential of samples was -13 and -21 MeV, respectively, at the physiological pH. **Figure 4.9**.

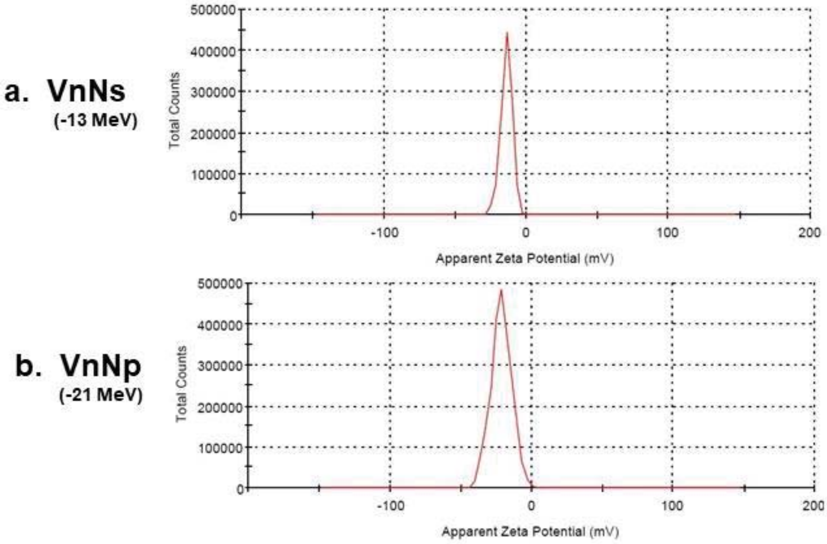

**Figure 4.9**. Images show the Zeta potential of VnNs and VnNp.

## 4.3. Preliminary screening on the *in vitro* biological interaction studies with vanadium pentoxide nanoparticles

### 4.3.1. Endotoxin detection

Endotoxin contamination in the nanomaterial could have an influence on its toxicity profile. Hence, the study estimated the levels of endotoxins in the nanovanadium samples through the Charles River Endosafe PTS kit PTS method and found to be <0.1 EU/ml for both VnNp and VnNs, which is lower than the USP (United States Pharmacopeia) recommended levels. This test indicates that the samples were free from bacterial endotoxin contamination.

### 4.3.2. Particle size in aqueous and cell culture media

The 1 mg/ml stock solution was prepared in sterile water. Working solutions of VnNs dispersed in water, and complete Dulbecco's Modified Eagle Medium (DMEM) were analyzed with a DLS particle size analyzer. The VnNs in water revealed an average size of 56±24 nm, and the size of VnNs in DMEM was 126±89 nm.

### 4.3.3. *In vitro* cell viability studies through MTT assay

Assayed the cell viability and proliferation as a function of mitochondrial metabolic activity in L929 fibroblast cells and MB-231 breast cancer cells upon treatment with VnNs and VnNp using an MTT assay. Cell viability was above 70 %, with all the treatment concentrations in L929 cells treated with VnNs for 24 h and 48 h. While the cell viability in VnNp treated L929 cells drastically declined below 50 % even with 12.5 µM treatment **Figure 4.10 a & b**.

At the same time in MB - 231 breast cancer cells, VnNs treatment showed a statistically significant 50 % loss in cell viability with 50 µM treatment, and the cell viability further reduced towards 48 h of VnNs treatment Figure 4.10. Further, the MB-231 cells showed a tremendous decline in the cell viability below 25 % with treatment concentrations from 12.5 to 100 µM for 24 h and 48 h **Figure 4.10 c & d**.

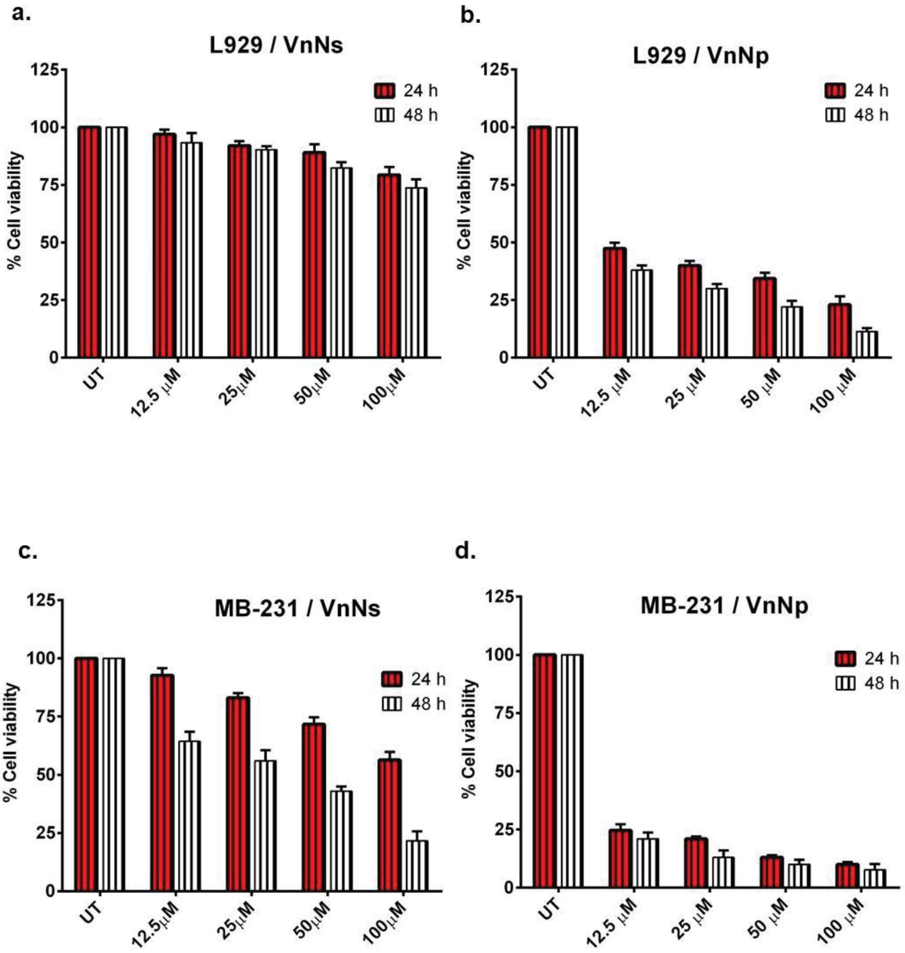

**Figure 4.10. MTT assay for cell viability in Vn treated L929 and MB-231 cells.** (a & b) L929 cells treated with VnNs & VnNp on for 24 and 48 h. (c & d) MB-231 cells treated with VnNs & VnNp for 24 h and 48 h.

Based on these results, a comparative analysis of the microbial interactions of VnNs and VnNp was evaluated using representative bacterial populations. Moreover, VnNs was chosen to understand the depths of cellular interactions on MB - 231 cells. Also, lately, evaluated to understand the *in vivo* biological interactions of VnNs using Swiss albino mice models.

## 4.4. The *in vitro* biological interactions of vanadium pentoxide nanoparticles on microbial models

The overall emphasis of the current work is to understand the microbial interactions of two different shapes of vanadium-based nanomaterials on two diverse, representative bacterial species. Several approaches have been made to achieve the same. The antimicrobial property of the vanadium-based nanomaterials was evaluated using representative gram-positive (G+) and gram-negative (G-) bacteria. The current study involved a brief understanding of various mechanisms by which Vn elicit its antibacterial efficacy on bacterial species with unique attributes to the nanomaterial shape and size. Here, the antibacterial efficacy of (VnNp) and (VnNs) at different nanomaterial concentrations were determined using Staphylococcus aureus (*S. aureus*) and Escherichia coli (*E. coli*) as representative (G+) and (G-) model organisms.

### 4.4.1. Minimum Inhibitory Concentration using liquid broth assay

The Minimum Inhibitory Concentration (MIC) is the minimum concentration of nanomaterial, which caused 50 % bacterial death. The MIC of Vanadium based nanomaterials were evaluated using liquid dynamic culture. Here, the MIC of VnNp found to be 0.613 mM for *E. coli* and 0.856 mM for *S. aureus*, which was compared with their respective untreated control bacterial suspension. In addition, the MIC of VnNs on *E. coli* was found to be 0.654 mM, and 0.937 mM for *S. aureus*. **Table 4.1.**

**Percentage growth inhibition = (OD of control - OD of test) / (OD of control) × 100%**

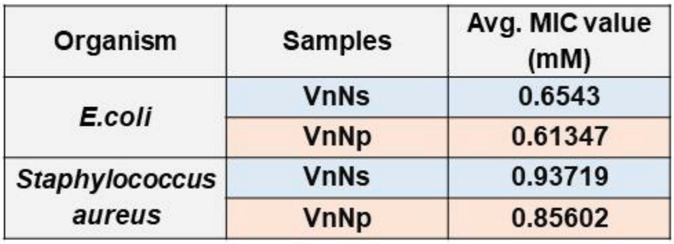

| Organism | Samples | Avg. MIC value (mM) |
|---|---|---|
| *E.coli* | VnNs | 0.6543 |
| | VnNp | 0.61347 |
| *Staphylococcus aureus* | VnNs | 0.93719 |
| | VnNp | 0.85602 |

**Table. 4.1. The MIC of VnNs and VnNp in *E. coli* & *S. aureus.***

## 4.4.2. Disc diffusion assay

Since we found that *E. coli* was more susceptible to nano vanadium treatment, both VnNp and VnNs were, were utilized in an agar disc diffusion assay. There was no observable bacterial zone of inhibition seen in the culture plates treated with neither VnNs nor VnNp with *E. coli*. It was surprising to observe no clear zones of bacterial inhibition on the agar plates spread with *E. coli* bacteria **Figure 4.11**.

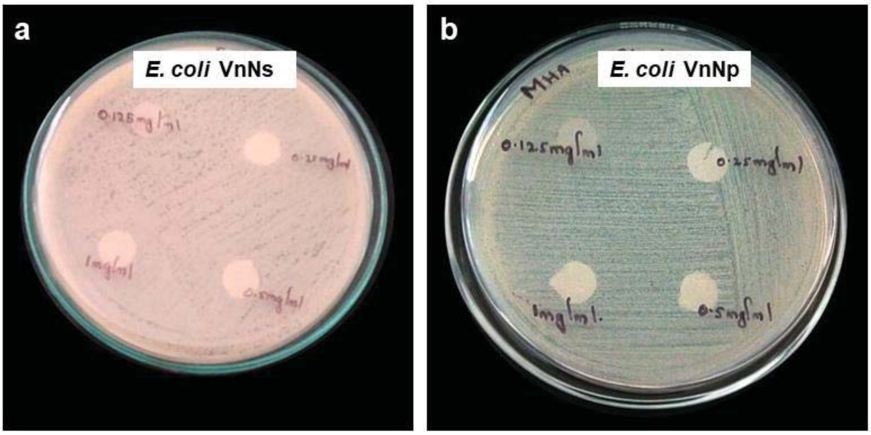

**Figure 4.11. Disc diffusion assay with *E. coli* cells** (a) VnNs and (b) VnNp.

Even though the disc diffusion assay failed to show an effective clear bacterial zone of inhibition, the liquid broth assay revealed a significant reduction in bacterial viability. Hence, in order to understand the changes that are taking place in the bacteria upon Vn treatment, carried out a Field emission scanning electron microscopy (FE-SEM) analysis. The electron microscopy technique was adopted to have a detailed understanding of the bacterial surface morphology with two different concentrations of Vn that are above and below the MIC values.

### 4.4.3. Bacterial surface morphology

Analyzed alterations in the bacterial morphology on samples treated with nano vanadium. The. *E.* coli samples upon treatment with 0.125 mM VnNs did not show any morphological alterations, while 1 mM VnNs treatment leads to the formation of slight depressions on the bacterial surface **Figure 4.12 a**.  Interestingly there was visible cell membrane damage and large depressions created on the surface of *E. coli* samples upon treatment with 0.125 mM and 1 mM VnNp **Figure 4.12 b**. This clearly indicated that *E. coli* was more susceptible to morphology disturbances with VnNp treatment rather than VnNs treatment.

While neither of the treatment, concentrations of VnNs caused morphological alterations in *S. aureus* bacterial samples. **Figure 4.12 c**. Further, 0.125 mM, VnNp treatment did not result in any morphological changes in *S. aureus.* In addition, 1 mM VnNp treated *S. aureus* bacteria were found to have a clumsy nature,  together with VnNp trapped between the bacterial cells, found attached over the surface of bacterial membranes **Figure 4.12 d** even after repeated washes with the buffer solution. This indicates that the high concentration of VnNp has a higher affinity for interacting with the membrane structures of gram-positive bacteria.

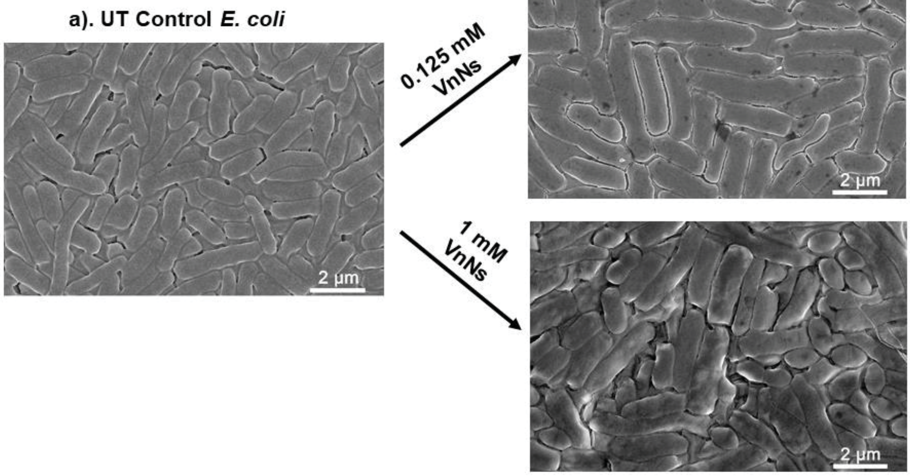
a). UT Control E. coli
0.125 mM VnNs
1 mM VnNs
2 µm
2 µm
2 µm

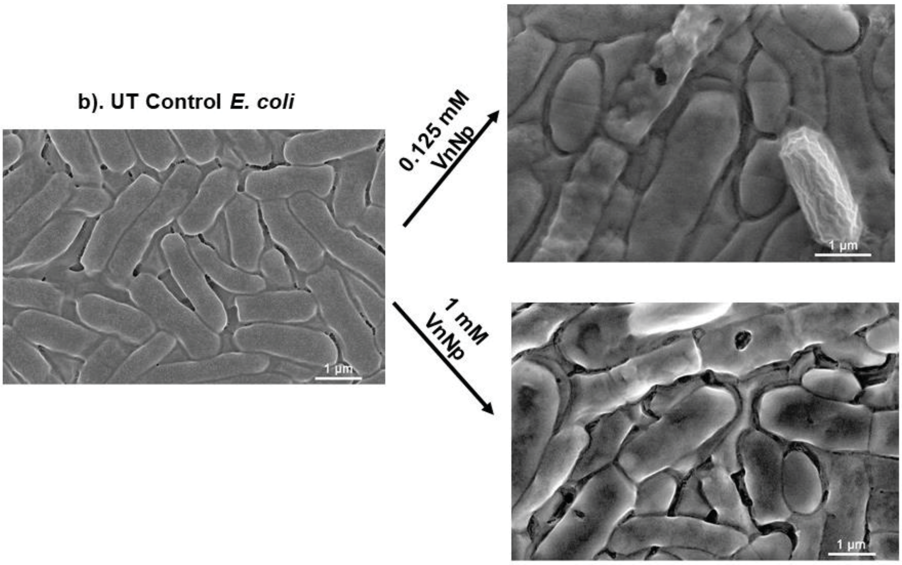
b). UT Control E. coli
0.125 mM VnNp
1 mM VnNp
1 µm
1 µm
1 µm

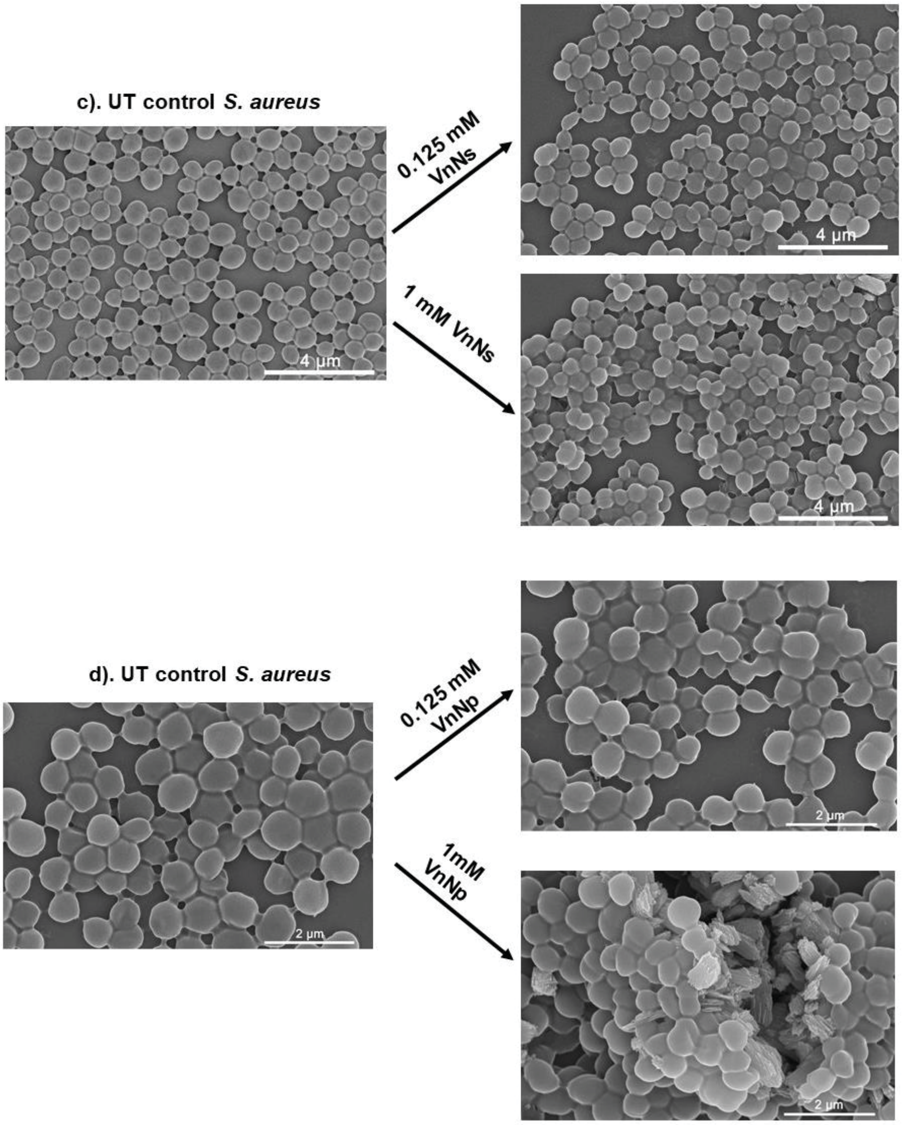

**Figure 4.12. Scanning electron micrographs on nano vanadium treated bacteria.** (**a**) Morphology observation on *E. coli,* treated with 0.125 mM and 1 mM of VnNs. (**b**) Morphology observation on *E. coli,* treated with 0.125 mM and 1 mM of VnNp. (**c**) Morphology observation on *S. aureus,* upon treatment with 0.125 mM and 1mM of VnNs. (**d**) Morphology observation on *S. aureus,* treated with 0.125 mM and 1 mM of VnNp.

Each bio-molecule has specific characteristic Raman spectra and corresponding Raman vibrations. In the current study, the Confocal Raman spectroscopy technique was utilized to understand various changes in the spectral pattern of bacteria treated with two different concentrations of Vn just above and below the MIC value.

### 4.4.4. Raman spectral signal analysis

The typical Raman signals arising from the DNA and proteins of the bacterial cells were studied using Raman spectral mapping technique. The spectra recorded from the bacterial samples were analyzed for various changes in the bacterial signals, that were altered upon treatment with nanoscale vanadium pentoxide. Compared the signals from 0.125 mM and 1 mM VnNp and VnNs treated *E. coli* and *S. aureus*.

The *E. coli* bacterial cells showed evident alterations in the spectral patterns upon VnNp and VnNs treatment, in comparison with their untreated controls. Interestingly, the peak at 1095 cm$^{-1}$ corresponding to the DNA phosphate backbone showed a drastic decrease in the Raman peak intensity upon 1 mM VnNp, and 1 mM VnNs treatment in *E. coli* cells **Figure 4.13 (a & b)**. However, the peak at 1095 cm$^{-1}$ was found to be unaltered with 0.125 mM VnNs treatment, whereas the same concentration of VnNp treatment resulted in a significant reduction in the peak intensity of *E. coli* cells.

The *S. aureus*, a representative gram-positive bacteria, did not change the bacterial spectral pattern with 0.125 mM or 1 mM VnNs treatment in comparison with their untreated control cells **Figure 4.13 (c)**. Further, 0.125 mM VnNp treatment also showed a similar spectral pattern as that of their untreated controls, indicating the absence of visible alterations in the spectral pattern in *S. aureus*. However, 1mM VnNp treatment resulted in the emergence of additional peaks at 993 and 697 cm$^{-1}$, which are the characteristic Raman peaks of nano vanadium pentoxide. **Figure 4.13 (d).**

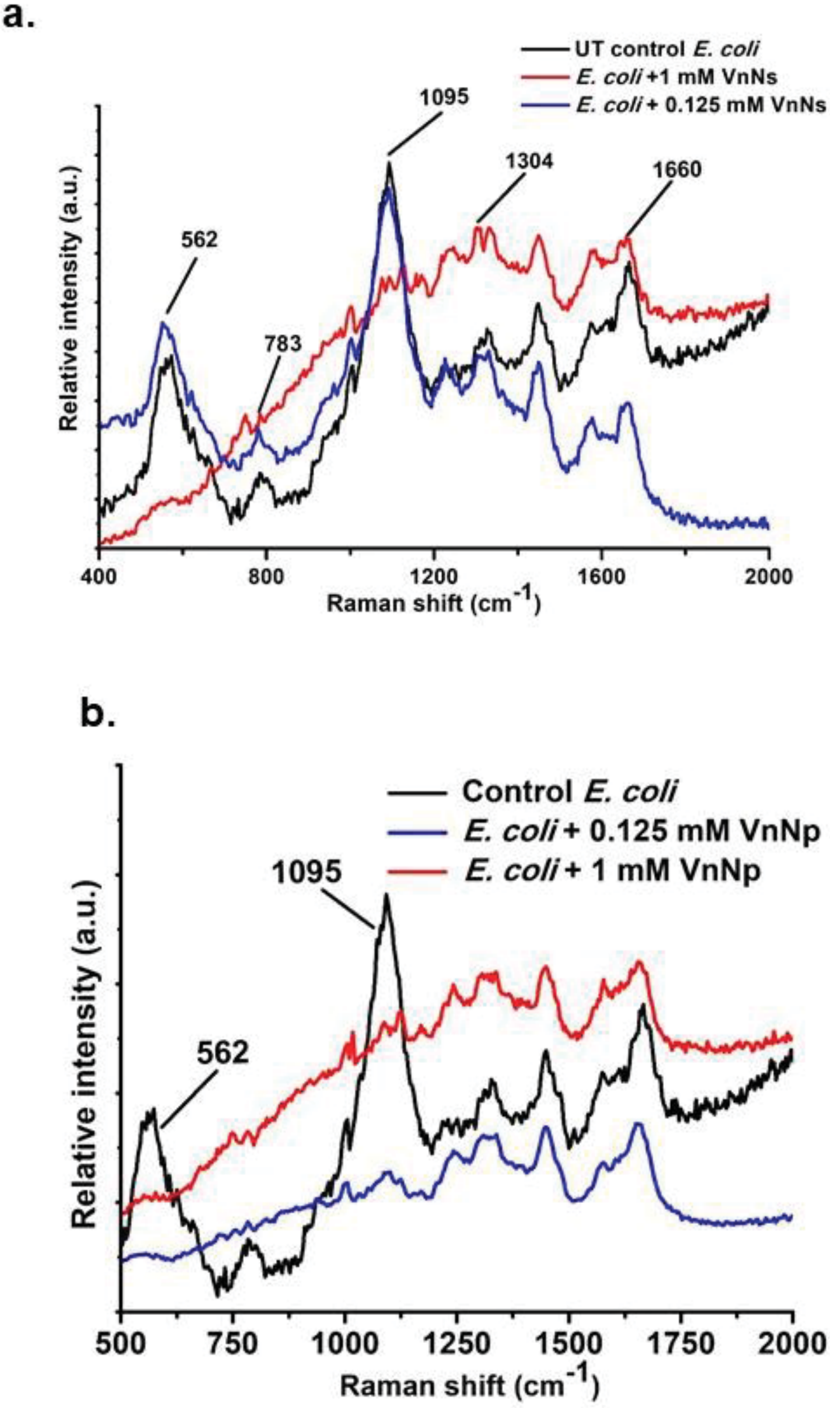
a.
UT control E. coli
E. coli +1 mM VnNs
E. coli + 0.125 mM VnNs
1095
1304
1660
562
783
Relative intensity (a.u.)
400
800
1200
1600
2000
Raman shift (cm-1)
b.
Control E. coli
E. coli + 0.125 mM VnNp
E. coli + 1 mM VnNp
1095
562
Relative intensity (a.u.)
500
750
1000
1250
1500
1750
2000
Raman shift (cm-1)

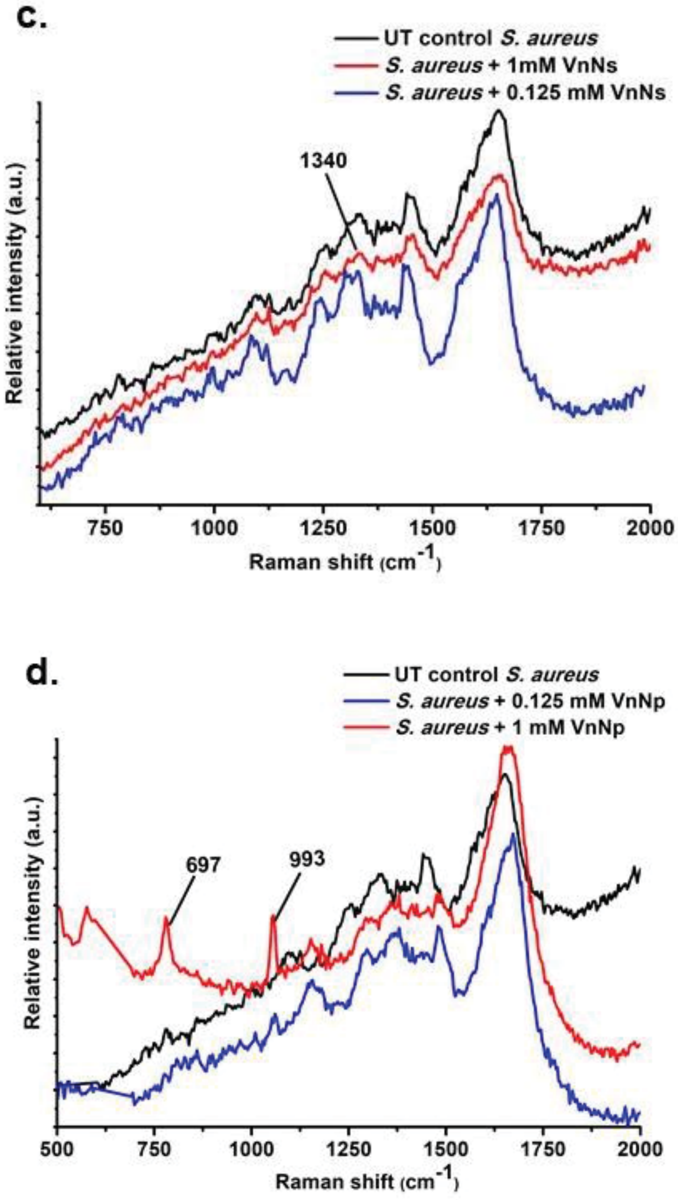

**Figure 4.13. Raman spectral mapping on bacteria.** (a) Spectra from VnNs treated *E. coli*. (b) Spectra from VnNp treated *E. coli*. (c) Spectra from VnNs treated *S. aureus*. (d) Spectra from VnNp treated *S. aureus*.

### 4.4.5. ROS detection in VnNp treated bacteria

Since we found that *E. coli* bacteria were more prone to VnNp and VnNs treatment, through the above results, we anticipated that this could possibly be due to ROS generation. In addition, ROS is considered an indicator of stress responses. Hence, the levels of ROS evoked in *E. coli* bacterial biofilms were monitored using DCFDA assay upon treatment with VnNs and VnNp. The fluorescence measurements revealed a 5-fold increase in green fluorescence intensity with VnNs treatment. And the green fluorescence intensity increased to 6-fold with VnNp treatment **Figure 4.14.**

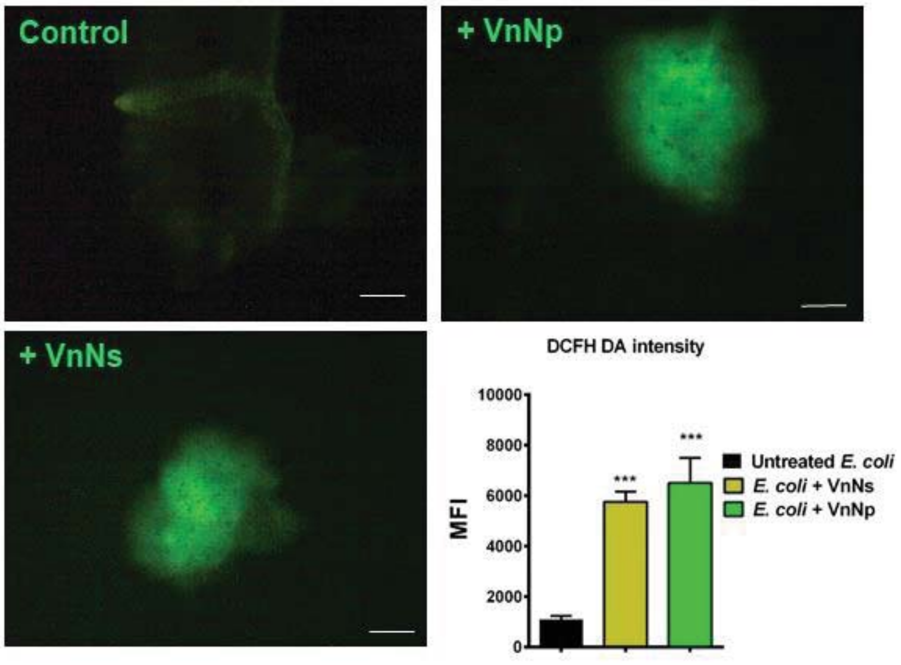

**Figure 4.14. ROS generation in *E. coli* biofilms.** Comparison of the fluorescent intensities of VnNs and VnNp treated *E. coli* biofilms with that of untreated control *E. coli* biofilms. Quantification of the fluorescence intensity is a measure of ROS. Data represent error bar shows S.D, where n=3, ***P < 0.001.

Based on the initial results on the cell viability assay with MB-231 and L929 cells, which gave an indication of the anticancer property of VnNs on the cancer cells. A series of detailed studies were carried out to understand the mechanism of VnNs action by which the dose and time-dependent activity of this material worked on MB-231 breast cancer cells.

## 4.5. *In vitro* cellular interactions of VnNs

### 4.5.1. Cellular uptake studies

For any nonmaterial interaction study, it is of most importance to validate the initial nanomaterial uptake by the cells. For which, flow cytometry was utilized to check for the change in scatter pattern in cells after exposure to VnNs. Attributed to the high electron density of VnNs, Raman spectroscopy, and electron microscopy on VnNs treated cells further served as efficient techniques to validate nanomaterial uptake.

#### *4.5.1.1. Cellular uptake by flow cytometry*

Assessed a comparison study on the cellular uptake of VnNs between healthy fibroblast L929 and human triple-negative breast cancer cell line MB-231 with flow cytometry. The nanomaterial uptake was studied in the cells by associating changes in the cell population between the Forward and Side scatter (FSC/SSC) region. The population of L929 cells in the P2 area between the untreated controls and 50 µM VnNs treated cell population did not served a drastic difference in the scatter plots. The results were not showing any statistically significant changes in SSC pattern **Figure 4.15 a**. The untreated control MB-231 cells exhibited a typical pattern of SSC, while the treatment groups indicated an increase in the SSC pattern of cells without much alteration in the FSC pattern. The 50 µM VnNs treated sample exhibited a statistically significant increase in the population of cells towards the SSC region from 76 % to 86 % in MB-231 cells **Figure 4.15 b**. The change in SSC is associated with the increased granularity attributed to efficient nanomaterial uptake in MB-231 cells when compared to the L929 cells.

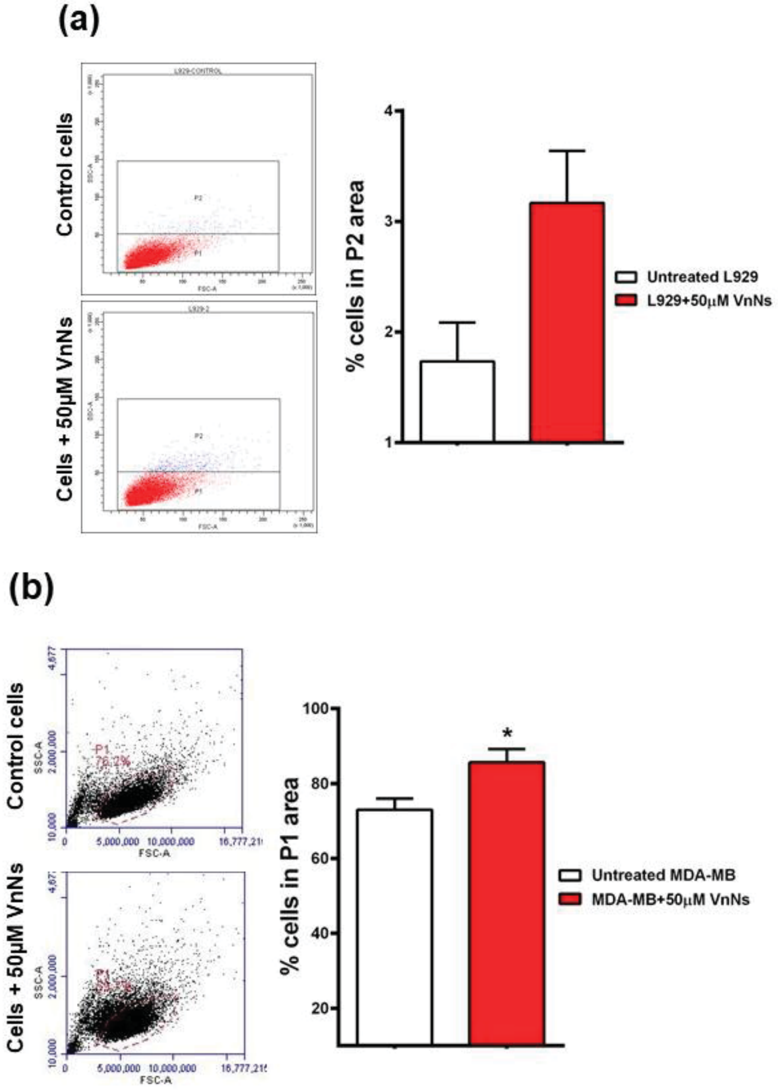

**Figure 4.15. Flow cytometry analysis showing changes in the side scatter pattern on L929 cells and MB-231 cells upon VnNs treatment.** a) VnNs treated L929 cells with no significant increase in SSC (represented data with S.D, n=4 & P value non-significant). b) MB-321 cells treated with VnNs showing increased cell population towards the SSC region due to an increase in cellular granularity because of VnNs uptake (represented data with S.D, n=3, & *P=0.009).

### *4.5.1.2. Cellular uptake studies through Raman spectroscopy*

Live MB-231 cells subjected to Raman spectral mapping with or without 50 µM VnNs pre-treatment, depicted a characteristic peak of vanadium oxygen bond at 996 cm$^{-1}$ **Figure 4.16**. This observation indicates the efficiency of nanomaterial uptake by the cells at 4h of VnNs incubation.

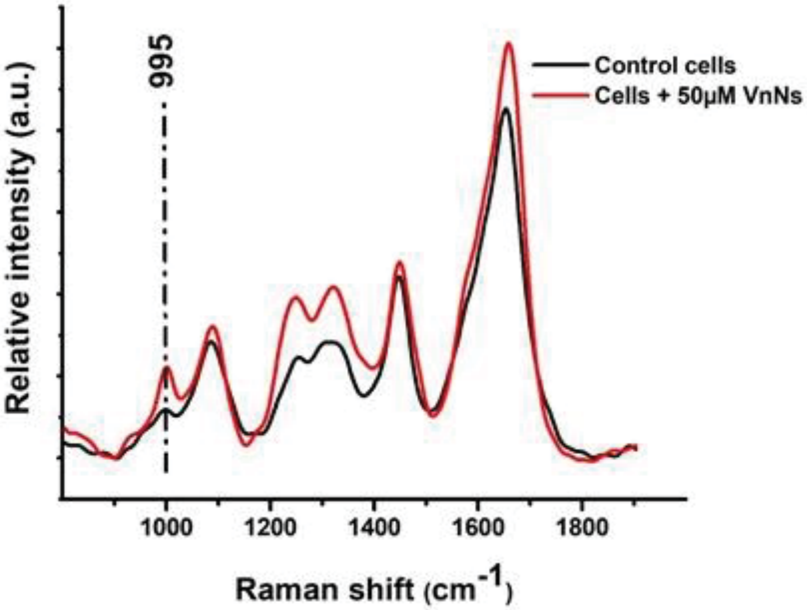

**Figure 4.16. Raman spectra of the untreated and VnNs treated MB-231 cells.** 50 µM VnNs treated cells depict characteristic peak at 995 (cm$^{-1}$), which correspond to the vanadium oxygen stretching vibration within 4h of nanomaterial incubation.

Electron microscopy serves an excellent tool that enables one to have a detailed understanding of the ultrastructural components within the cells. Pertaining to the high electron density of VnNs, they allow direct visualization of its intracellular positioning within the cells. In addition, cellular processing for EM further allows us to have a detailed understanding of the various cellular organelles, nucleus, membrane ultrastructure, etc.

### *4.5.1.3. Cellular uptake studies through TEM analysis*

The high electron density of the VnNs makes them easily trackable within the cytoplasm of cells using a TEM. The electron micrographs obtained from the ultra-thin cross-sections of untreated and VnNs treated MB-231 cells are shown in **Figure 4. 17**. Untreated cells show intact cellular morphology and organelle architecture, and cells exposed to VnNs treatment for 4 h depict efficient nanomaterial uptake by the cells without any characteristic alterations in the cellular morphology. TEM analysis revealed the cytoplasmic distribution of VnNs, as distinct small aggregates within intracellular vesicles (indicated through red arrows).

In addition to the VnNs uptake, certain areas of the cells evidently showed vesicle formation with compartmentalized cytoplasmic extensions containing organelles such as mitochondria **Figure 4.17**. The treatment induced the formation of membrane-bound intracellular structures called the “phagosomes,” which signified the onset of Autophagy (red asterisk). In addition, the micrographs displayed fusion between autophagosomes and lysosomes within the initial 4 h of VnNs treatment in cells (blue asterisk). Hence, further, the study focused on adopting various techniques to analyze the extent of autophagy induction in VnNs treated MB-231 cells at various time points.

Autophagy induction is considered as a cell’s own rescue mechanism to over-come any unfavorable environmental conditions. The process involves entrapping cellular organelles in autophagosomes and digesting them in lysosomes to meet the energy requirements of the cells. Here, the electron micrographs clearly indicate the presence of these membrane-bound vesicles in the 4 h VnNs treated cells. Autophagy is a transient process and happens as an immediate stress response. Further, it evaluated the extent of autophagy induction in VnNs treated cells using the identification of specific marker proteins in autophagy.

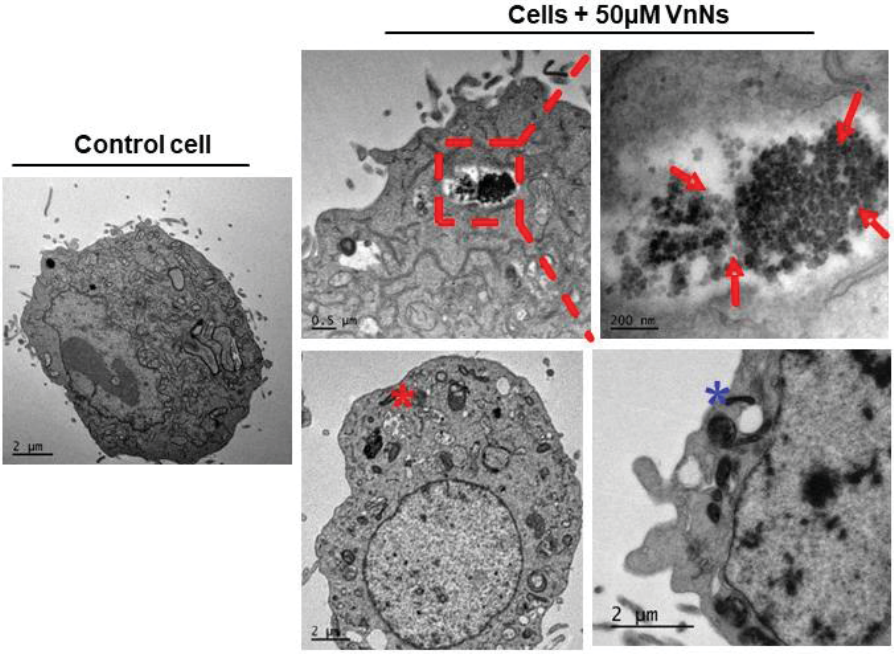

**Figure 4.17. Transmission electron micrographs of cells.** The ultra-structural details of control cells and 4 h VnNs treated MB- 231 cells. Red arrows indicate the intracellular localization of VnNs in aggregates. The red star indicates autophagosomes with entrapped organelles. Blue star denotes fusion between phagosome and lysosome in VnNs treated cells.

## 4.5.2. Autophagy induction in VnNs treated MB-231 cells

### *4.5.2.1. Electron microscopy for autophagy induction*

Electron microscopy analysis on 4 h VnNs treated cells, depicted the presence of cytoplasmic organelles inside membrane-bound vesicles called auto-phagosomes (red arrows), considered as a hallmark of autophagy **Figure 4.18**. The auto-phagosomes carried dark stained VnNs along with cytoplasmic organelles, observed both dark and lightly stained vesicles with organelles trapped inside. The lysosomes appeared as dark rounded organelles and presented stages of acidification in them. In addition, the micrographs also depicted typical auto-phagosome fusion with the darkly stained lysosomes (blue arrow) **Figure 4.18,** clearly indicate autophagy induction.

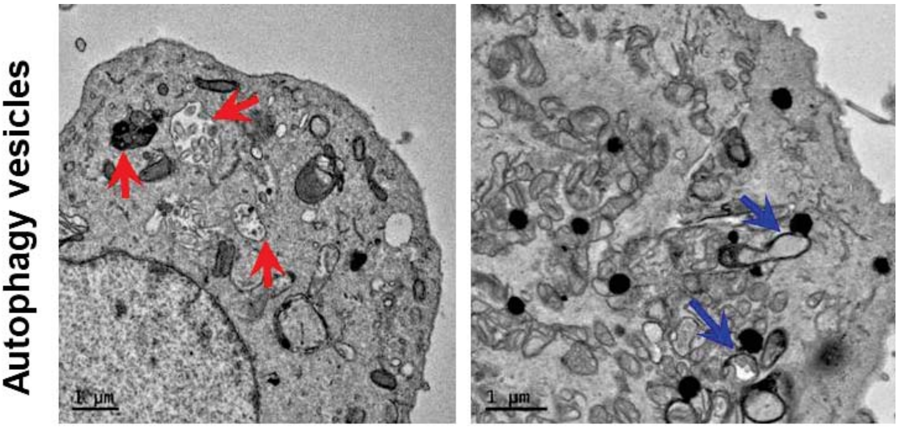

**Figure 4.18. EM showing autophagosome formation during autophagy induction with VnNs treatment.** Autophagosomes interact with dark stained acidic compartments called the lysosome to form autolysosomes. Scale bar 1 µm.

Further, gained the visual evidence on autophagy induction from fluorescence microscopy on MB-231 cells stably expressing plasmids for microtubule-associated protein 1 light chain 3 (LC3) conjugated to green fluorescence protein (GFP-LC3). The two different forms of LC3 protein named LC3-I and II were further quantitatively measured to understand the extent of autophagy induction in VnNs treated MB-231 cells, using a flux assay. The assay measured the protein levels of LC3-II and I with an initial 4 h of VnNs treatment.

#### *4.5.2.2. Autophagy studies through fluorescence microscopy imaging*

Typical autophagy induction in VnNs treated cells examined the intracellular localization of LC3 proteins in GFP-LC3 expressing transformed MB-231 cells. The untreated cells exhibited faint, diffuse green signals from the cytoplasm, which represented an average basal level of autophagy in the control cell population. Whereas the VnNs treated cells showed evident sharp spots of green, punctuate fluorescence pattern, which is characteristic of LC3 accumulation in autophagosomes during autophagy induction. The 50 µM VnNs treated cells showed around 6 to 18 punctuates per cell immediately after 4 h of treatment, which indicated significant autophagy induction **Figure 4.19**. Almost every cell in the microscopy field exhibited sharp green spots in the 4 h treatment 50 µM VnNs treatment, which shows the efficiency of VnNs in eliciting autophagy in transformed cell clones.

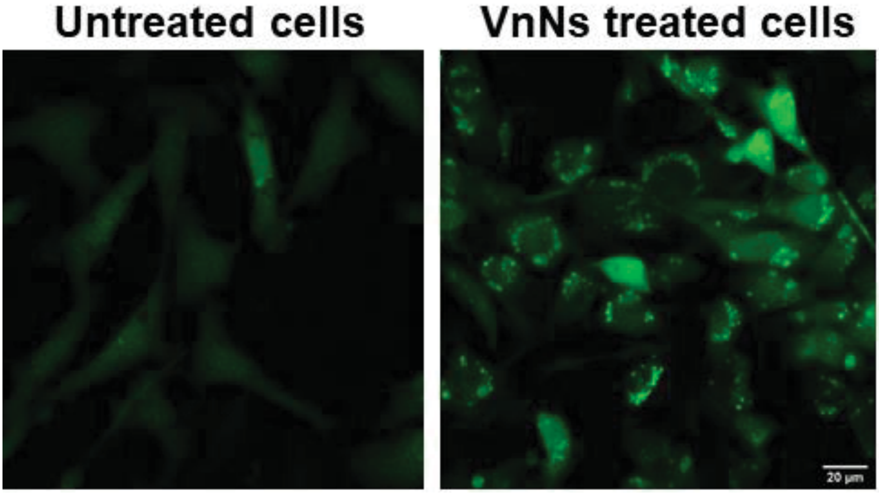

**Figure 4.19. MB-231 cells with GFP-LC3 plasmids showing LC3 puncta formation upon VnNs treatment.** Untreated cells show very week green fluorescence, and VnNs treated cells show LC3 puncta formation in GFP-LC3 expressing cells. Scale bar 20 µm.

### *4.5.2.3. Western blot analysis for LC3 protein*

Western blot analysis gives a quantitative measure of the levels of LC3 proteins. A flux assay studied the transient shift in the level of LC3 - II proteins & I, using 4 h VnNs treated cell population. Simultaneously, treated the cells with chloroquine for analyzing the levels of LC3 flux, to block the phago-lysosomal fusion. The blots revealed a visual increase in the LC3-II levels upon VnNs treatment **Figure 4.20 a**. Quantification of the protein levels using Quantity1 software observed a two-fold increase in LC3-II protein levels in the vanadium-chloroquine co-treatment group in comparison with the VnNs alone treated group of cells, which denoted autophagy induction after 4h of vanadium treatment **Figure 4.20 b**. Further analyzed to see the expression levels of LC3 protein from MB-231 cell samples when treated with VnNs for different time points. The blots indicated a visual increase in LC3 protein levels at all the VnNs treatment time points as related to the 24 h untreated and starvation control group of cells **Figure 4.20 c.**

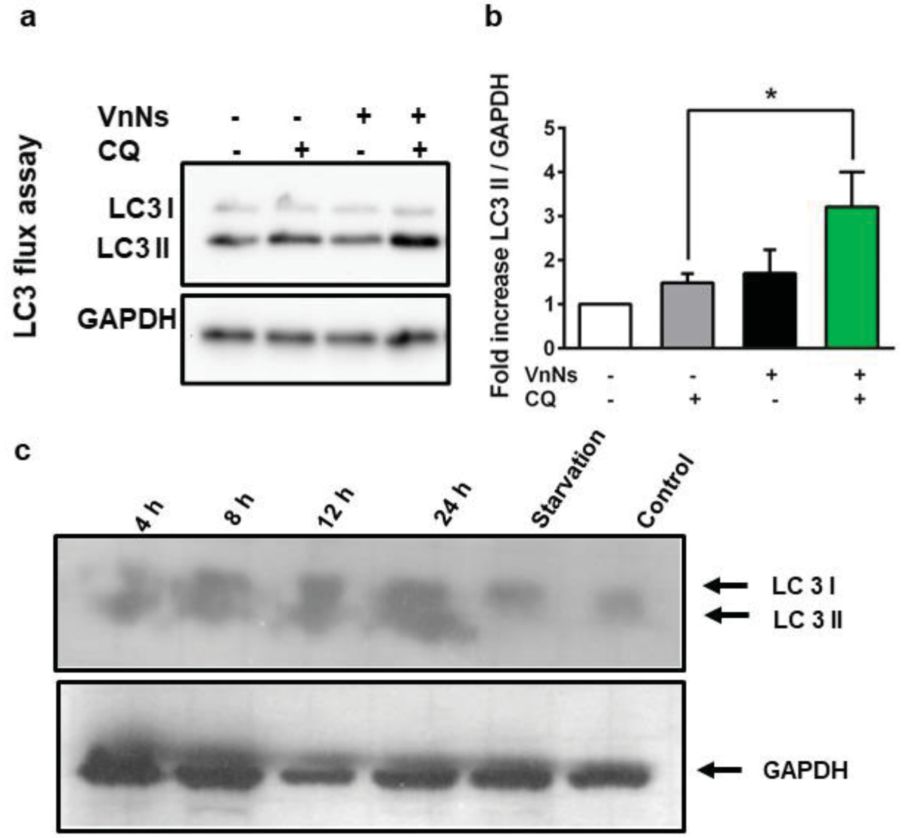

**Figure 4.20. Protein analysis showing LC3 expression in VnNs treated MB-231 cells.** (a) Western blots show visual observation on the levels of LC3 II protein in a flux assay. GAPDH depicts loading control. (b) Quantification of the protein levels with S.D, n=4, *P < 0.05. (c) Western blots were elucidating the LC3 expression at different time points. The image shows a visual increase in the LC3 levels for all the time points in the study when compared with the untreated and starvation controls.

As the process of autophagy, marked a progressive accumulation of mitochondria in autophagosomes and involved in the digestion of mitochondria within the membrane-bound organelles, an experiment to understand the simultaneous evaluation of the mitochondrial health with TMRM staining and autophagy induction in GFP-LC3 puncta forming cells were followed using fluorescence microscopy.

## 4.5.3. Intracellular interactions of VnNs on mitochondria

### *4.5.3.1. Mitochondrial activity studies using live-cell time-lapse fluorescence imaging*

Monitored autophagy induction and related mitochondrial health simultaneously using GF-LC3 transformed cell clones. Autophagy induction, marked by the increase in LC3 puncta formation in 25 & 50 µM VnNs treated cells over 24 h period. In addition, the results also indicated a gradual decline in the red fluorescence intensity pattern corresponding to the indicator dye TMRM in cells treated with 25 & 50 µM of VnNs, by 24 h of pre-treatment **Figure 4. 21**. These results proved the loss of mitochondrial membrane potential in MB-231 cells subsequent to VnNs treatment. The comparison is made with HBSS treated cells and untreated control cells. The results indicated an increased puncta formation and decreased red fluorescence intensity in the case of vanadium treated cells than HBSS treatment. The untreated healthy cells in the time-lapse live-cell fluorescence microscopy indicated an intact red fluorescence intensity pattern even in the 24 h sample, indicating that the external environmental conditions were favorable for the cells during live-cell imaging over the course of the experiment. Hence, the results clearly show that the loss of red fluorescence intensity due to loss of mitochondrial membrane potential is linked to the GFP-LC3 puncta formation and autophagy induction upon interaction with VnNs.

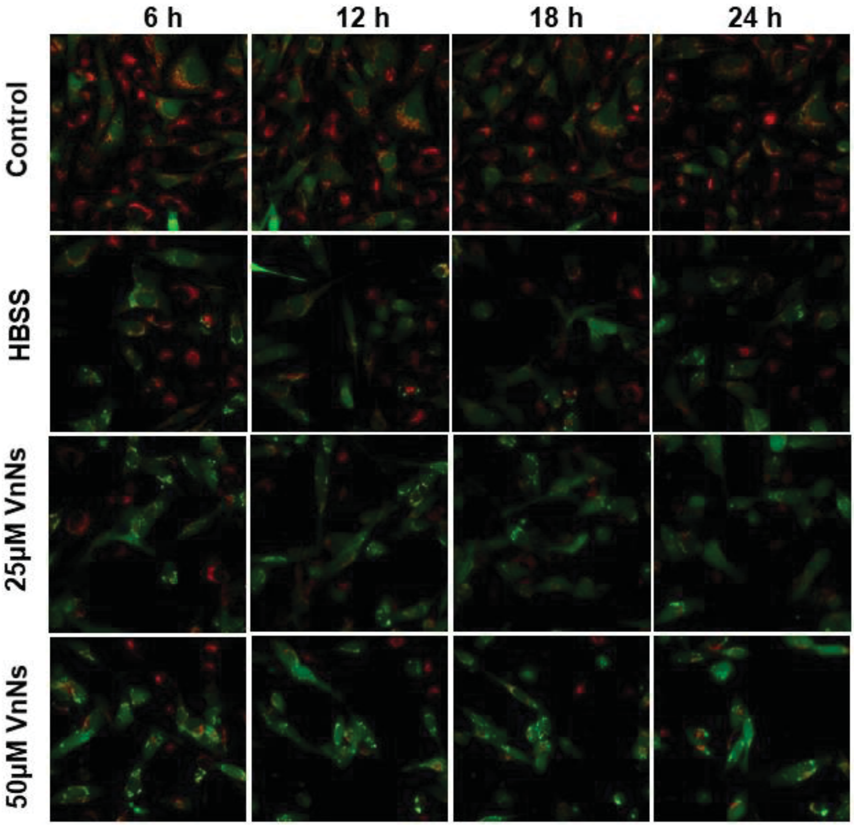

**Figure 4.21. Time-lapse fluorescence microscopy imaging on GFP-LC3 cells.** LC3 puncta seen as sharp green spots in autophagy inducted GFP-LC3 expressing MB-231 cells treated with VnNs. Red fluorescence is from TMRM stained mitochondria, indicating the mitochondrial viability.

The autophagy process also initiates the loss of mitochondrial membrane potential (MMP). Hence, we evaluated the MMP with mitochondrial membrane potential indicator dye - JC-10. Quantified the population of VnNs treated cells that have lost MMP by flow cytometry in JC-10 stained cells. In addition, it utilized fluorescence microscopy for visual identification of lost MMP.

#### *4.5.3.2. Analysis of mitochondrial membrane integrity through JC-10 staining*

Mitochondrial membrane potential plays a crucial role in maintaining organelle architecture and function. Hence, analyzed the mitochondrial membrane potential in VnNs treated MB-231 cells using JC-10 dye. The flow cytometry data revealed control cells possessing both red and green fluorescence indicated through the population of cells in the quadrant positive for both PE and FITC. While the VnNs treated cells established a remarkable shift in the population of cells towards the FITC region, showing more green fluorescence along with a low red fluorescence intensity pattern. The results indicated a change in the mean fluorescence intensity from red to green over a 50 µM VnNs treatment period of 24 h **Figure 4.22 a**. This observation indicated a loss of mitochondrial membrane potential upon 24 h VnNs treatment through the flow cytometry analysis.

Further, fluorescence microscopy provided visual evidence on the fluorescence pattern in cells either treated or untreated with VnNs, followed by JC-10 staining. The untreated control cells presented active spots of red fluorescence from the intact mitochondria; and diffuse green signals from the cytoplasm. While, the 24 h, 50 µM VnNs treated cells, exhibited a drop in the red fluorescence intensity pattern, with more cells exhibited only green fluorescence. This observation further indicated the loss of mitochondrial membrane potential upon 24 h VnNs treatment **Figure 4.22 b**.

Again, confirmed this observation with live-cell mitochondrial membrane potential indicator, TMRM in VnNs treated cells. The healthy cells readily give out strong spots of red fluorescence from intact mitochondria, while the VnNs treatment resulted in a loss of mitochondrial membrane potential and indicated a low red fluorescence intensity pattern in comparison with the untreated control population of cells **Figure 4.22 c**.

**a. Flow cytometry with JC10**

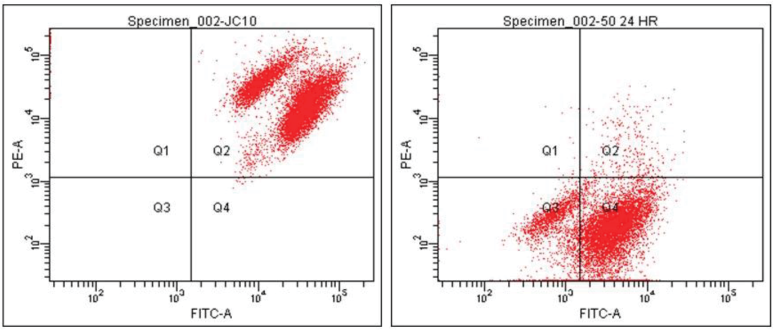

**b. Fluorescence microscopy with JC-10 staining**

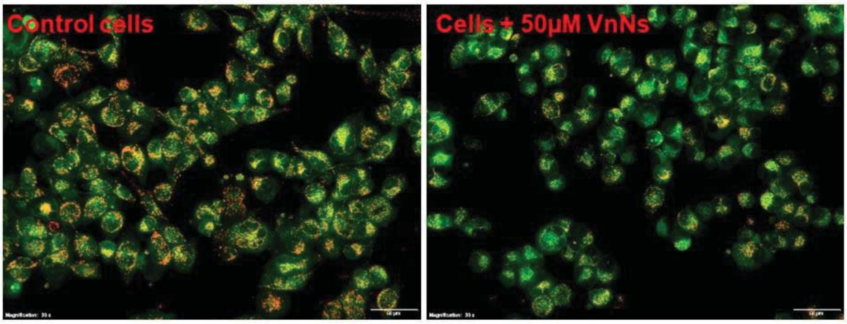

**c. Fluorescence microscopy with TMRM staining**

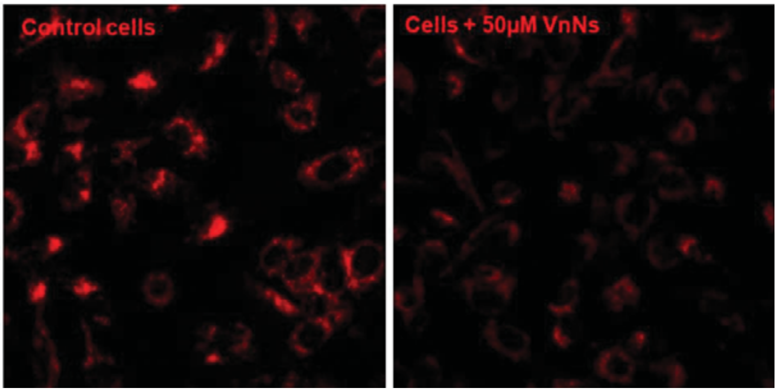

**Figure 4.22. Assay for mitochondrial membrane potential (ΔΨm).** (a) Flow cytometry assay on 24 h VnNs treated cells stained with mitochondrial JC-10, Scale bar 50 µm. (b & c) Fluorescence images from 24 h 50 µM VnNs treated MB-231 cells stained with JC-10 and TMRM, respectively, indicating loss of mitochondrial membrane potential.

The mitochondrial membrane potential loss could also result in opening the mitochondrial membrane permeability transition pores (MPTP), which allow the accumulation of VnNs inside the mitochondria. Hence, the prolonged effect of VnNs treatment for 24 h on cellular organelles such as mitochondria was evaluated using electron microscopy.

### *4.5.3.3. VnNs uptake into the Mitochondria through electron microscopy*

Electron microscopy on 24 h VnNs treated cells depicted the characteristic presence of nanoparticles inside the mitochondria **Figure 4.23.** The sharp, intense black spots from the mitochondria revealed VnNs uptake by the organelles. The images were representative of 10 different fields from the 24 h, 50 μM VnNs treatment.

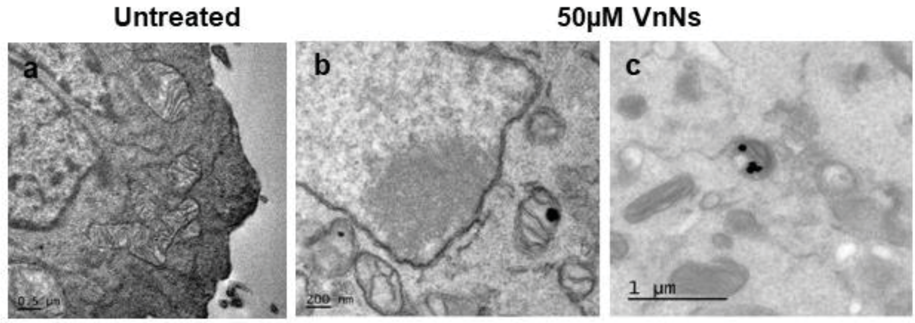

**Figure 4.23. Electron micrographs depict the mitochondrial uptake of VnNs in MB-231 cells. (a)** Control cells show intact organelles in the cytoplasm. **(b & c)** Represents cytoplasm of VnNs treated cells with particle accumulation within the mitochondria of treated cells.

In addition to the mitochondria, lysosomes also play an essential role in nutrient recycling during the process of autophagy. Hence, the prolonged effects of VnNs treatment for 24 h on cellular organelles such as lysosomes were further evaluated using fluorescence microscopy and electron microscopy.

## 4.5.4. Intracellular interactions of VnNs on lysosomes

### 4.5.4.1. *Lysosomal distribution using Lysotracker red imaging*

Lysotracker red stains acidic compartments within the cells. The fluorescence images depict untreated control cells, with a small-sized, minimal lysosomal number. And the 50 μM VnNs pre-treated samples indicated a significant difference in the lysosomal size, total lysosomal number, and increased red fluoresce intensity pattern in cells following 24 h 50 μM VnNs exposure. The lysotracker fluorescence intensity increased significantly by 10 times in treated cells compared with their untreated control cells **Figure 4. 24**.

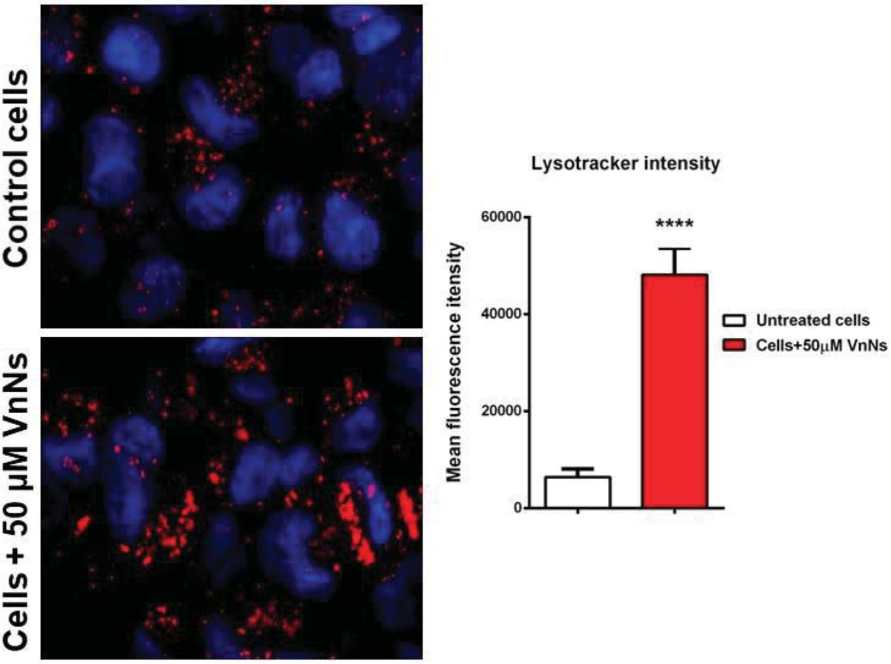

**Figure 4.24. Fluorescence micrographs showing lysotracker red intensity profile on control and cells treated with 50 μM VnNs for 24 h.** Shows the difference in lysosomal size, total lysosomal number, and increased red fluorescence intensity pattern; error bar shows S.D where n=8, ****P < 0.0001. Image obtained at 100 X magnification.

### *4.5.4.2. Lysosomal membrane integrity through acridine orange staining*

The membrane integrity of the lysosomal compartments plays an essential role in deciding the fate of cells. Monitored vesicular acidification, a hallmark of autophagy with the help of acidic vesicle specific acridine orange, which gave sharp red fluorescence intensity pattern from acidified compartments.

Here, the VnNs treated MB-231 cells stained with acridine orange dye, revealed sharp spots of red fluorescence and showed an increased number and size of acidic compartments in the 24 and 48 h treated samples. They were indicated through an increased red fluorescence intensity pattern from the cytoplasm of control cells when compared between the 24 and 48 h treated samples. In addition, the cells were observed to have an intact lysosomal membrane up on VnNs treatment on cells even after 48 h of incubation **Figure 4. 25**. Nuclei of the cells were pre-stained with Hoechst, indicated as blue signals from the cells. None of the treatment groups showed a loss of lysosomal membrane integrity or any decline in the red fluorescence intensity pattern during any time point of the study period. Any damage in the lysosomal membrane would have otherwise resulted in leakage of the dye to the cytoplasm, leading to a reduction in the red fluorescence intensity pattern. This strongly indicated the presence of intact lysosomal membranes.

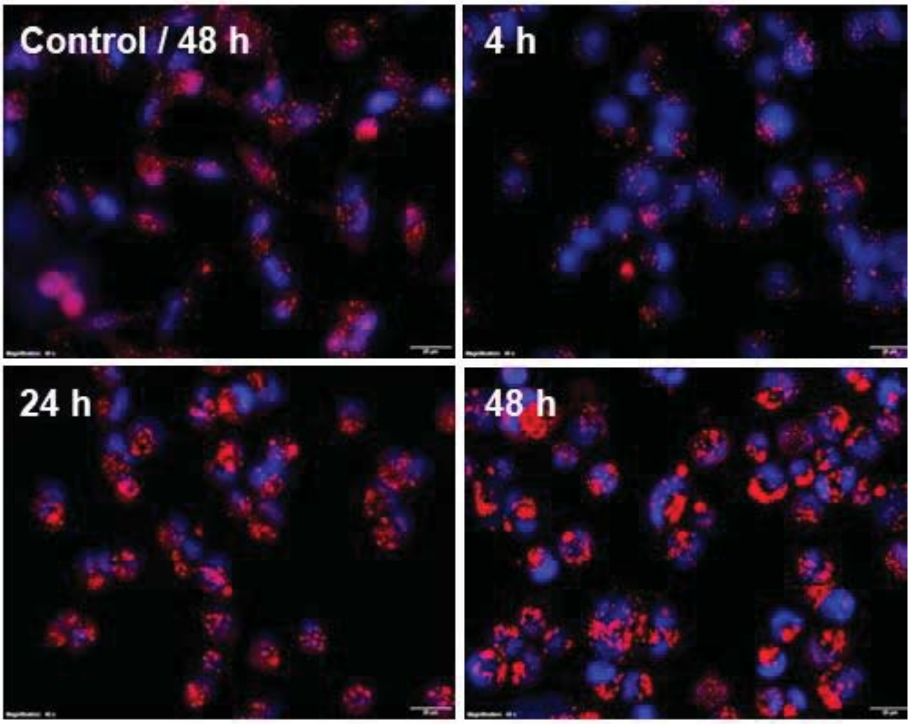

**Figure 4.25. Fluorescence micrographs of acridine orange stained cells.** Untreated and 50 µM VnNs treated cells show intact lysosomal membrane towards 4, 24 & 48 h of post-VnNs exposure. Scale bar 20 µm

To have more information on the above findings, a detailed investigation of the membrane architecture of lysosomes in VnNs treated cells were obtained with electron microscopy.

#### *4.5.4.3. Changes in lysosomal compartments through Electron Microscopy*

Electron micrographs depict untreated MB-231 cells, with small-sized sparsely distributed lysosomes **Figure 4. 26 a**. However, the 24 h, 50 µM VnNs pre-treatment resulted in a significant difference in lysosomal size, acidification, and total lysosomal numbers and denoted a pattern migration towards the peri-nuclear region, indicating the high acidity of these organelles **Figure 4. 26 b.**

The acidic compartments are heavily stained in with osmium tetroxide used for processing cells for TEM, that clearly visualize the presence of large darkly stained rounded lysosomes, around 150-200 nm size following 24 h of VnNs treatment.

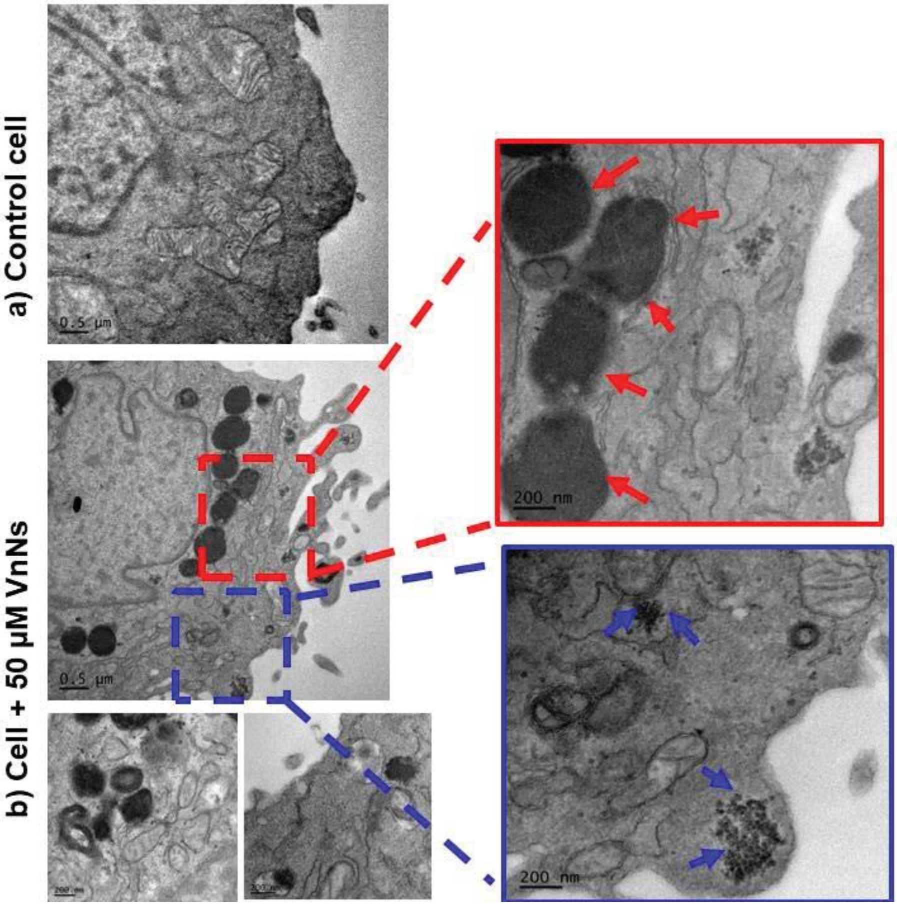

**Figure 4.26. Electron micrographs of the VnNs treated and untreated MB-231 cells depicting lysosomal acidification**. a) Control cells. b) Shows VnNs treated cell with acidification, and perinuclear localization of lysosomes.

The micrographs clearly showed darkly stained lysosomes (red arrows) and the presence of VnNs in the cytoplasm (blue arrows).

An increase in lysosomal number and size is indicative of defective autophagy, which could lead to alterations in the cell cycle and further evoke various other stress response reactions in VnNs treated cells. Hence, it analyzed the progression of cells in the cell cycle using a flow cytometry assay. The cellular stress response was further evaluated using DCFDA assay, which indicated the level of total ROS in treated cells at different time points. Both qualitative and quantitative measures of ROS were studied.

### 4.5.5. Cell cycle analysis through flow cytometry

Flow cytometry studies evaluated the number of cells at different phases of the cell cycle. 25 & 50 µM VnNs were used on cells for 24, 36 & 48 h, which resulted in a G2/M phase cell cycle arrest with a rise in cell population corresponding to the second spike in each of the histograms represented in **Figure 4.27**. Population of cells in the G1 phase declined from 66 % (control) to 45 % (50 µM), 61 % (control) to 40 % (50 µM), and 56 % (control) to 30 % (50 µM) upon 24, 36 & 48 h of incubation. Correspondingly, the results indicated an increase in total number of cells in the G2/M phase from 15 % (control) to 38 % (50 µM), 20 % (control) to 46 % (50 µM), and 20 % (control) to 49 % (50 µM) among the 24, 36 & 48 h of VnNs treated samples. These measures accounted for more than two-fold of cells that progressively accumulated in the G2/M phase of post-treatment. A comparable pattern of cell cycle arrest was observed within the 24, 36, and 48 h of incubation.

The progressive accumulation of cells in the G2/M phase indicated cell cycle arrest, and the cells no longer undergo cell division. The cells also experience stress response reactions in these cells, which were subsequently evaluated using DCF assay, Amplex red assay, and also quantitatively evaluated the mRNA levels of antioxidant genes.

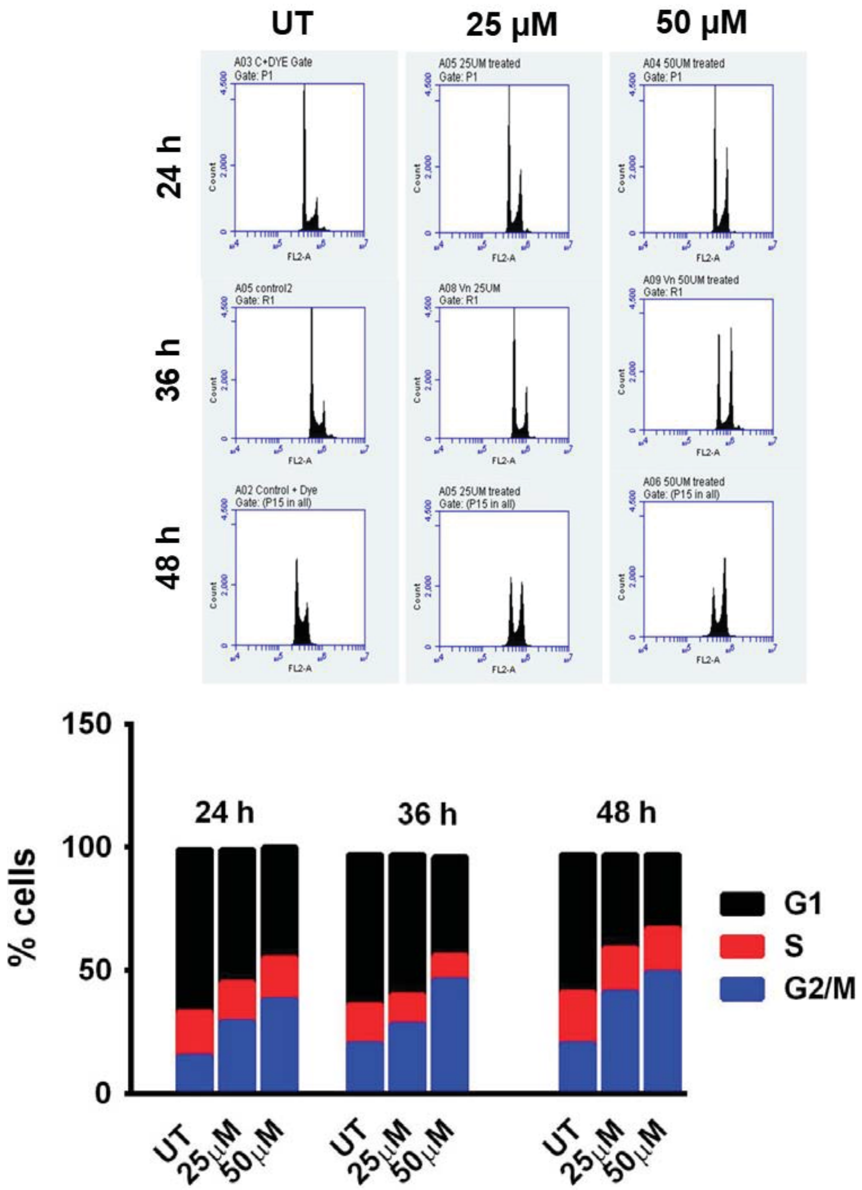

**Figure 4.27. Flow cytometry analysis of VnNs treated cells for cell cycle progression.** Quantification depicts the number of cells at each phase of the cell cycle. Denotes increased cell number at the G2/M phase of the cycle at 24, 36, and 48 h of VnNs treatment, indicating cell cycle arrest in the cells.

### 4.5.6. *In vitro* analysis on reactive oxygen species (ROS)

#### *4.5.6.1. In vitro analysis on MB-231 cells using DCF-DA assay*

The potential of VnNs to alter the redox balance in treated cells was studied by measuring the levels of ROS formed inside the cells using H2-DCFDA assay assisted fluorescence microscopy. The qualitative observation denoted a concentration and time-dependent green fluorescence intensity decrease at 4 h and an increase at 24 h of VnNs treatment in the levels of ROS production between treatment and control groups. Further, quantitative results expressed here indicates the percentage relative fluorescence intensity (% RFU) of the fluorescent dye from the treated cells. The cells in the treatment group showed about a 30 % reduction in the ROS levels at 4 h of 50 μM VnNs incubation, though the ROS pattern overturned to give a noteworthy increase in levels towards 24 h treatment period in association with the 24 h untreated control group **Figure 4. 28**.

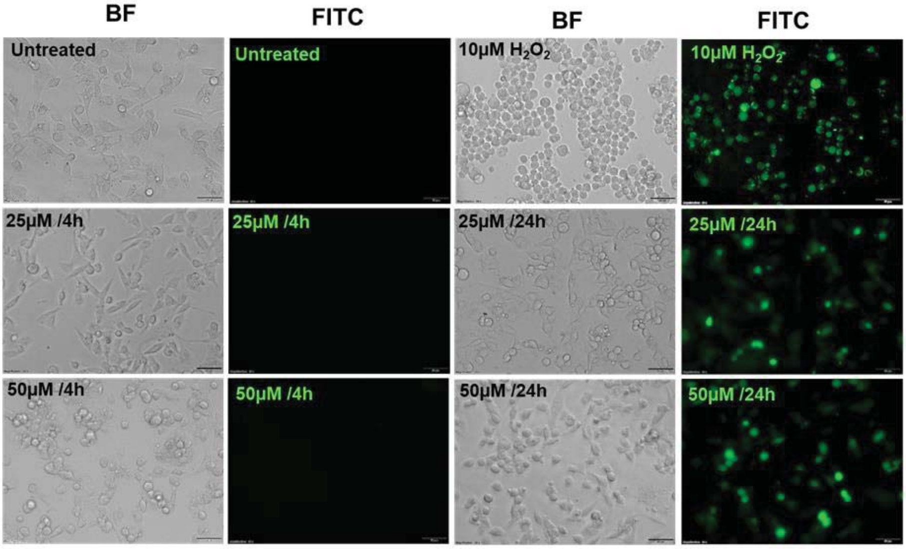

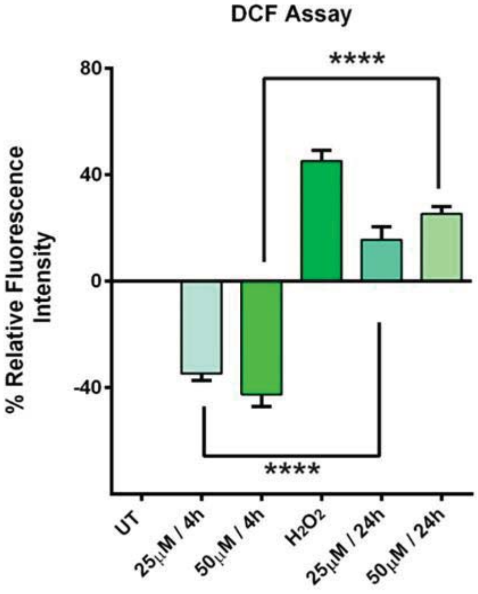

**Figure 4.28. DCF fluorescence from MB-231 cells at 4 and 24 h post-VnNs treatment.** Cells show a decline in the ROS levels at the initial 4 h and a significant increase in ROS towards 24 h of VnNs incubation, Scale bar 50 µm. Qualification on the fluorescence intensity achieved through spectrofluorometric analysis. Data with error bar shows S.D, where n=5, ****P < 0.0001.

The decrease in DCF fluorescence could be due to the intrinsic property of VnNs to quench intracellular ROS, or the treatment could evoke cellular anti-oxidant machinery to cope up with the generated ROS. Hence, the activity of VnNs to quench the highly reactive oxy radicals were evaluated using a cell-free system, adopting Pyrogallol assay.

#### *4.5.6.2. In vitro analysis on a cell-free system using Pyrogallol assay*

Pyrogallol decomposes to give superoxide and purpurogallin. They undergo auto-oxidation in the presence of superoxide, and the rate of the forward reaction is dependent on the extent of superoxide produced or quenched. A kinetic spectroscopic study proved the ability of VnNs to quench the superoxides produced due to the decomposition of Pyrogallol to its chromophore purpurogallin. Observed a decrease in the rate of pyrogallol auto-oxidation by 7 % in the presence of VnNs within the initial 10 minutes of reaction **Figure 4. 29.** Attributed to the ability of VnNs to inhibit superoxide formation or accelerated neutralization of oxy-radicals.

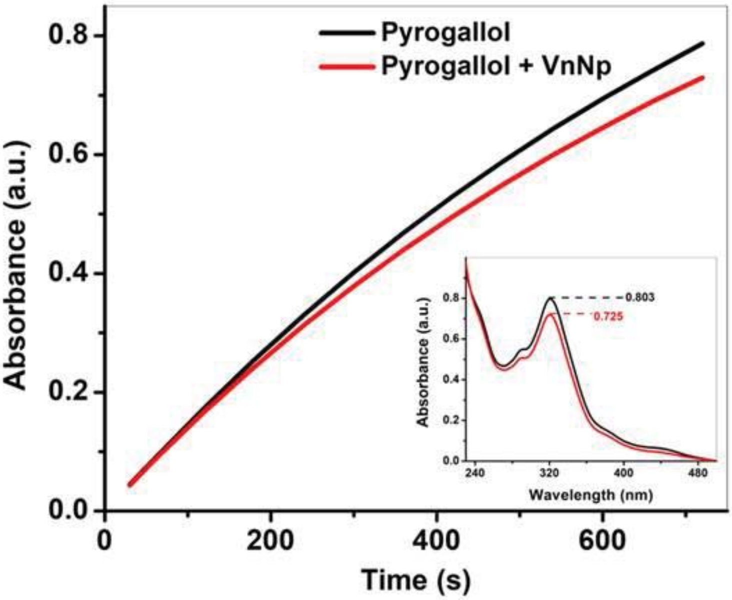

**Figure 4.29. Kinetic study expressing the rate of pyrogallol autoxidation**. VnNs treatment on pyrogallol slowdown in the rate of pyrogallol autoxidation. The inset shows the decrease in the absorbance pattern of the product, purpurogallin, at 320 nm.

A significant component of the cellular ROS is $H_2O_2$; hence, apart from the DCF assay, a more specific assay that precisely understands the levels of $H_2O_2$ at different time points of VnNs treatment was further performed.

### *4.5.6.3. In vitro amplex red assay for $H_2O_2$ detection in MB-231 cells*

Utilized an Amplex red assay, which is highly specific for $H_2O_2$, to further confirm the results of DCF assay. This assay indicates the fluorescence intensity of the dye component resorufin, which is directly related to the $H_2O_2$ levels between treated and untreated cell populations. This spectroscopic technique clearly showed a more than 40 % reduction in the fluorescence intensity at 4 h of 50 µM VnNs treatment **Figure 4. 30.**

This result indicates the VnNs mediated $H_2O_2$ quenching activity *in vitro* at early time points. Furthermore, the levels of $H_2O_2$ heightened to around 20 % towards 24 h of incubation points similar to the hike in ROS levels observed with the DCF assay.

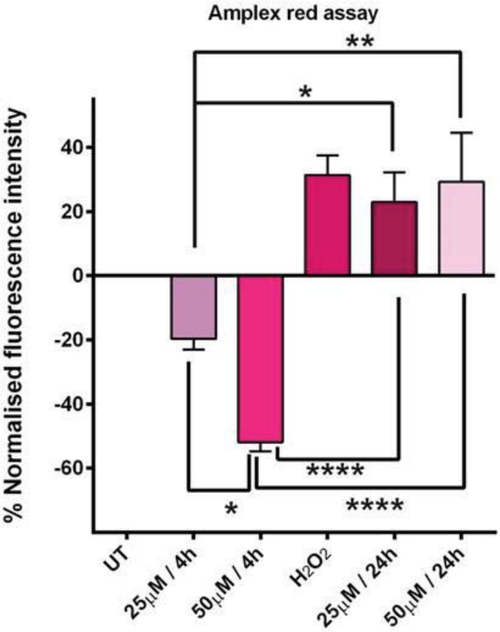

**Figure 4.30. Amplex Red fluorescence intensity on MB-231 cells.** Spectrofluorometric quantification on the fluorescence intensity levels of the reaction product resorufin, between treated and untreated cell populations. Data with error bar shows S.D, where n=3, ****$P < 0.0001$, ***$P < 0.001$, **$P < 0.01$ & *$P < 0.05$.

Cells maintain a constant balance between ROS generation and redox cycling. The cells tightly regulate the process of redox balance by controlling the levels of stress response mRNA at any given point of time. Hence, further, evaluated the levels of stress response mRNA in 4 and 24 h VnNs treated MB-231 cells using the real-time qPCR technique. The assay used 18s rRNA as the internal control for normalizing the levels of specific mRNA at each time point.

### 4.5.7. Analysis of the mRNA levels of stress response genes *in vitro*

The redox potential in cells is tightly regulated by converting highly reactive superoxide radicals into comparatively less reactive hydrogen peroxide ($H_2O_2$) involving the activity of various dismutase's like SOD1, SOD2, SOD3, and catalase respectively. Relative levels of these SOD's and catalase mRNA were monitored as a measure of redox function in cells upon VnNs treatment. Comparatively low levels of SOD1 mRNA was seen in cells treated with 25 & 50 μM for 4 h and 25 μM for 24 h, while a two-fold increase in mRNA levels was detected with the 50 μM, 24 h treatment group **Figure 4.31 a**. In addition, there was a steady rise in the pattern of mitochondrial SOD2 mRNA levels, though the increase was not statistically significant at any of the treatment concentrations and time points **Figure 4.31 b**. The levels of SOD3 in the 4 h 50 μM VnNs treatment resulted in a statistically significant decrease in mRNA levels as compared to their untreated controls. While the other treatment groups did not show any significant alterations from the basal control mRNA levels, **Figure 4.31 c**. Catalase mRNA showed approx. Three-fold increase in the mRNA levels with the 4h 25 & 50 μM treatment, while the levels declined below the basal mRNA levels with 24 h vanadium treatment **Figure 4.31 d**.

Correlating, these results on increased lysosomal accumulation, ROS, $H_2O_2$, and low catalase mRNA profiles, towards 24 h of treatment, all accounted for the stress responses in VnNs treated cells. These phenomena could significantly evoke cell death in treated cells towards 24 and 48 h of treatment. Hence, further prompted to study the mode of cell death via, apoptosis is in detail. Used various methods to arrive into the conclusion of apoptotic mode of cell death, which kill the affected cell by causing no harm to the neighbouring cell population. The molecular changes including membrane flipping, caspase activation and membrane blebs were analysed. Adopted flow cytometry assay with Annexin-V and PI, FRET based fluorescence microscopy imaging for caspase activation and used scanning electron microscopy for visualizing the apoptotic blebs over the cell surface of apoptotic cells.

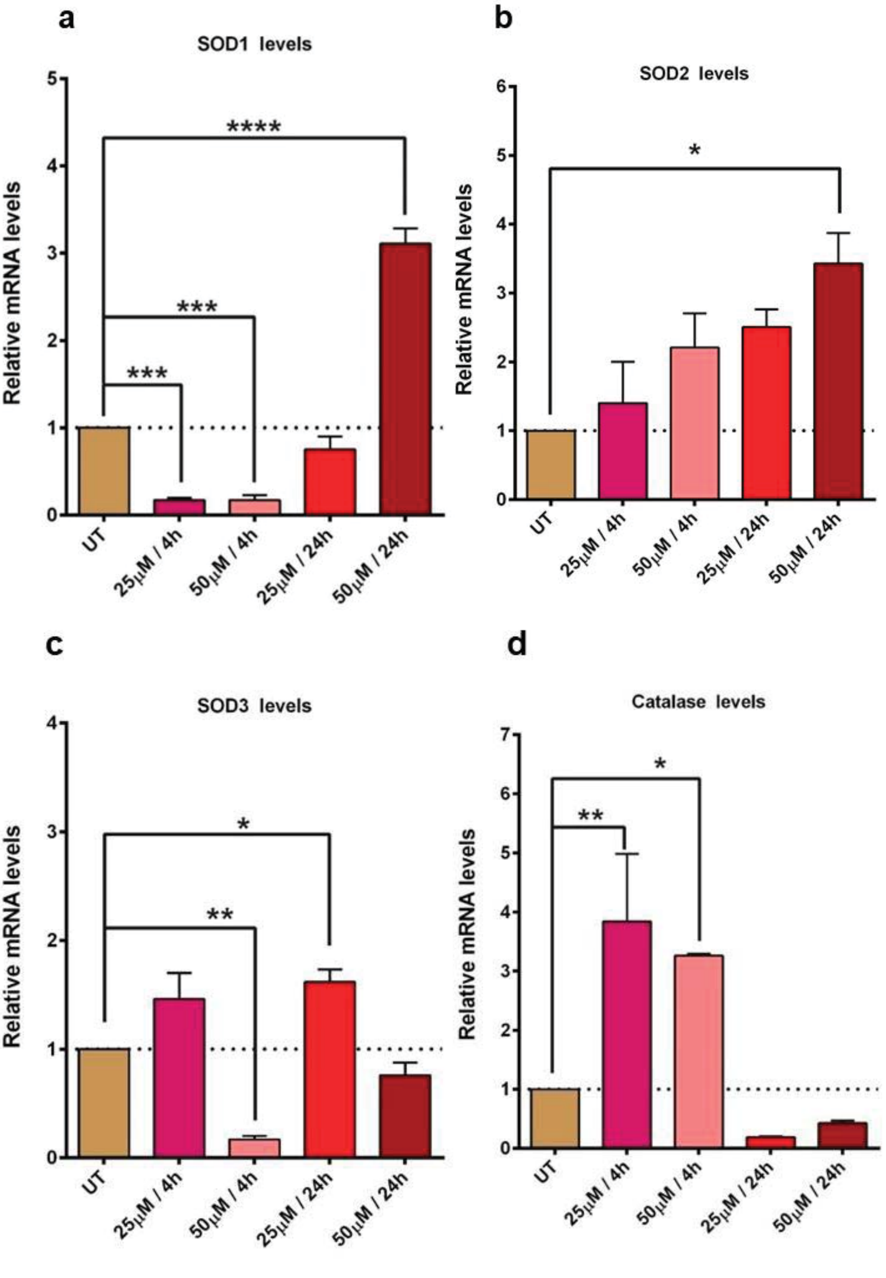

**Figure 4.31. Relative mRNA levels of SOD1, 2, 3 and catalase between the untreated controls and VnNs treated MB-231 cell populations.** Indicate a concentration and time dependent activity and the data represent error bar that shows S.D, where n=4, ****P < 0.0001, ***P < 0.001, **P < 0.01 & *P < 0.05.

## 4.5.8. Assay for cell death in VnNs treated MB-231 cells

### *4.5.8.1. Flow cytometry analysis with Annexin-V-FITC/ Propidium Iodide*

The 50 µM VnNs treated cells showed a noticeable rise in cell population positive for Annexin–V, (seen in the FITC channel) in comparison with the untreated control cells as established through flow cytometry **Figure. 4. 32.** The cells that labeled as late apoptotic cells in the 48 h treatment accounted for more than twice the population seen with 24 h treatment. Data presented no considerable increase in the cell number corresponding to early apoptosis, upon 24 h VnNs treatment.

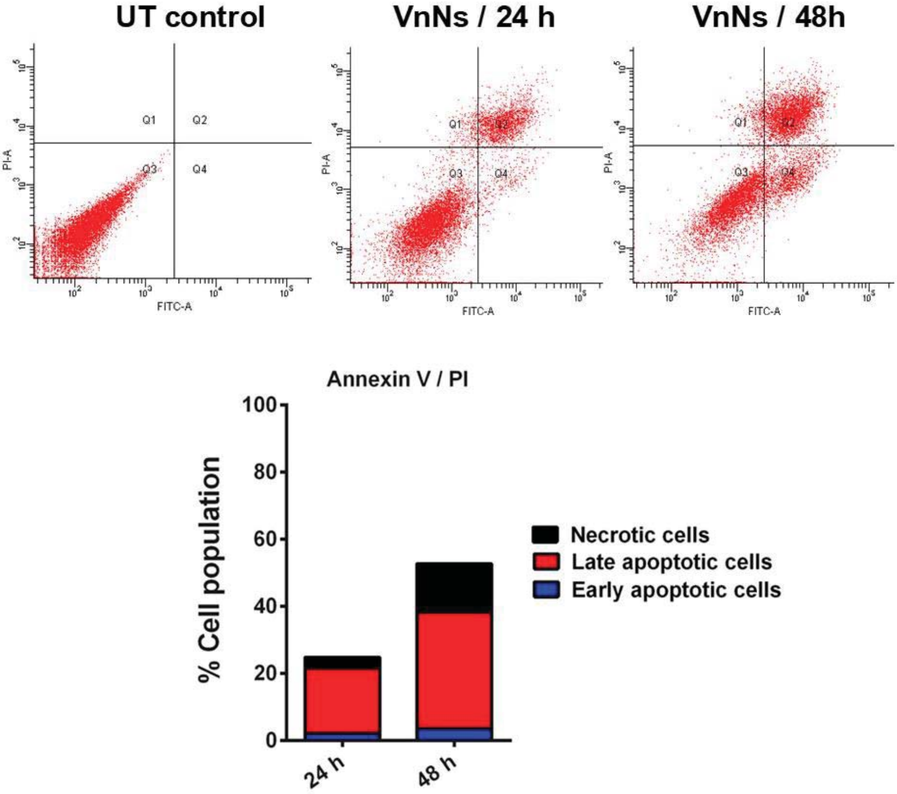

**Figure 4.32. Flow cytometry analysis on the quantification of apoptotic cells.** Quantitative data reveal the number of cells at each phase of apoptosis via, Annexin-V/PI staining upon VnNs exposure for 24 & 48 h.

However, the results of this assay are sensitive to the environmental changes. Hence a much more sensitive method was adopted, which utilized a caspase sensitive sensor protein translated from the plasmid in the transformed cells.

#### *4.5.8.2. FRET based assay on MB-231 cells expressing Caspase-3 sensor*

A FRET-based live-cell imaging technique, was adopted to understand the degree of cytosolic caspase activation in engineered MB-231 cells. The cells expressing caspase-3 sensor FRET probe SCAT3 NLS were adopted for the study. VnNs treatment-induced caspase activation in cells and resulted in successive FRET loss, which was reflected in the amplified donor (ECFP) to acceptor (Venus) fluorescence (ECFP/Venus) **Figure. 4.33**. The caspase-activated cells exhibited a characteristic FRET loss, and the fluorescence merged images were detected as blue spots (3rd merged panel). The number of cells towards 24 h VnNs treatment resulted in efficient caspase activity and was linked to the increased number of blue cells in the merged images. The ratiometric images gave a better visual clarity, which represented caspase-activated cells with yellow-red fluorescence. The imaging is established based on the caspase activity in real-time. The FRET mechanism is lost due to the cleavage of caspase sensitive sequencences by activated caspases in treated cells. The FRET assay is turned onn only in caspase activated cells and the mechanism is insensitive to the external environmental variations. Here, the extent of caspase activity in VnNs treated cells were considered as a hall mark of apoptosis mediated cell death. The results show an evident increase in the number of cells positive for caspase activity in 25 and 50 µM of 48 h VnNs treated cells. This microscopic evidence for caspase activation in treated cells further proves that the 48 h treatment resulted in apoptosis mediated cell death in the breast cancer cells.

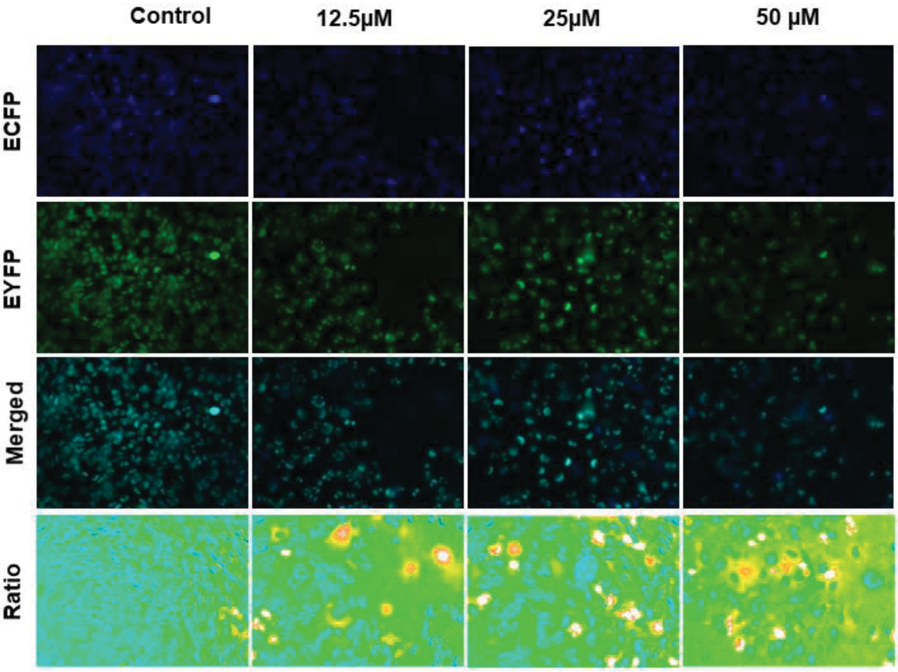

**Figure 4.33. Fluorescent microscopy images of SACT3-NLS expressing cells.** FRET activity denoted through ratio images (in the lowermost panel) shows cells with activated caspase 3/7 at 24 h of VnNs treatment. Used a 20X objective with 0.75 NA.

These results reveal the co-existence of a variety of complex pathways that involved in an interplay between autophagy with increased LC3 levels that finally lead to caspase activation resulting in apoptosis. These mechanisms operate in tandum that prompt the breast cancer cells to die. In addition, apoptosis also marks changes in the cytoskeletal architecture, cell membrane morphology, and nuclear condensation pattern, hence further assessed these aspects, which accounted for an apoptotic mode of cell death towards 48 h of VnNs treatment. The study proves a time dependent shift in the cell resque pathway with an apoptosis mediated cell death, with the help of various assays and visual evidence from transmission electron microscopy.

### 4.5.9. Morphology observation through cytoskeletal architecture

Actin filament, a significant component in the cytoskeleton, showed characteristic filament retraction, reorganization, which resulted in altered cellular morphology in cells pretreated with 50 µM of VnNs for 48 h. Monitored the pattern of actin reorganization using Rhodamine phalloidin, **Figure 4. 34** and Alexa Fluor 488, **Figure 4. 35** with a confocal microscope. Results indicated evident actin retraction with both the stains. The nuclei were stained with DAPI, indicated through blue fluorescence.

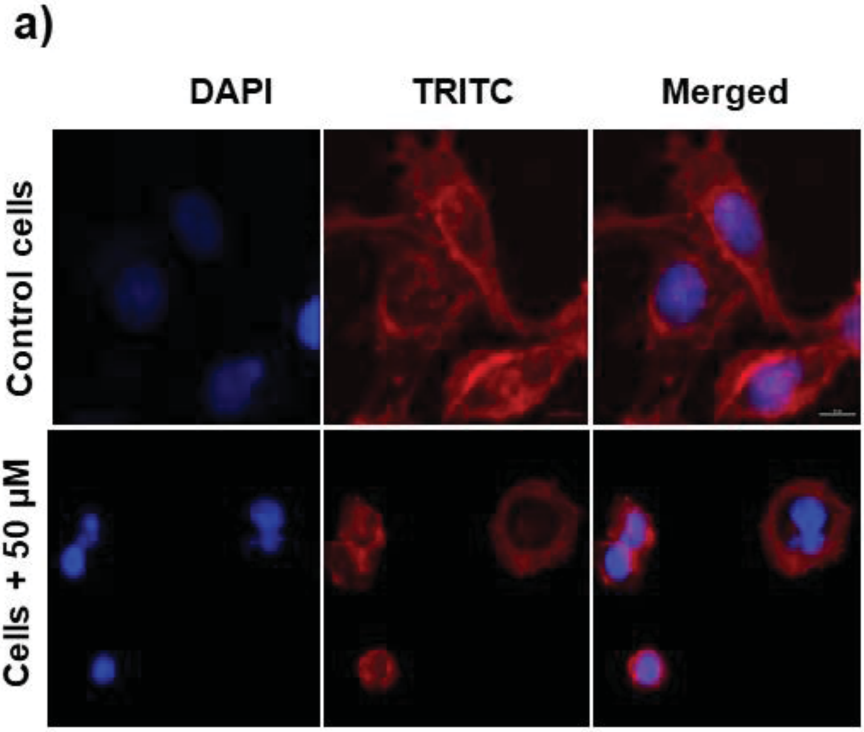

**Figure 4.34. Fluorescence microscopy images show morphology observation in VnNs treated MB-231 cells stained with Rhodamine phalloidin.** Indicate the cytoskeletal actin filament reorganization upon 48 h VnNs treatment. Scale bar shows 100 µm.

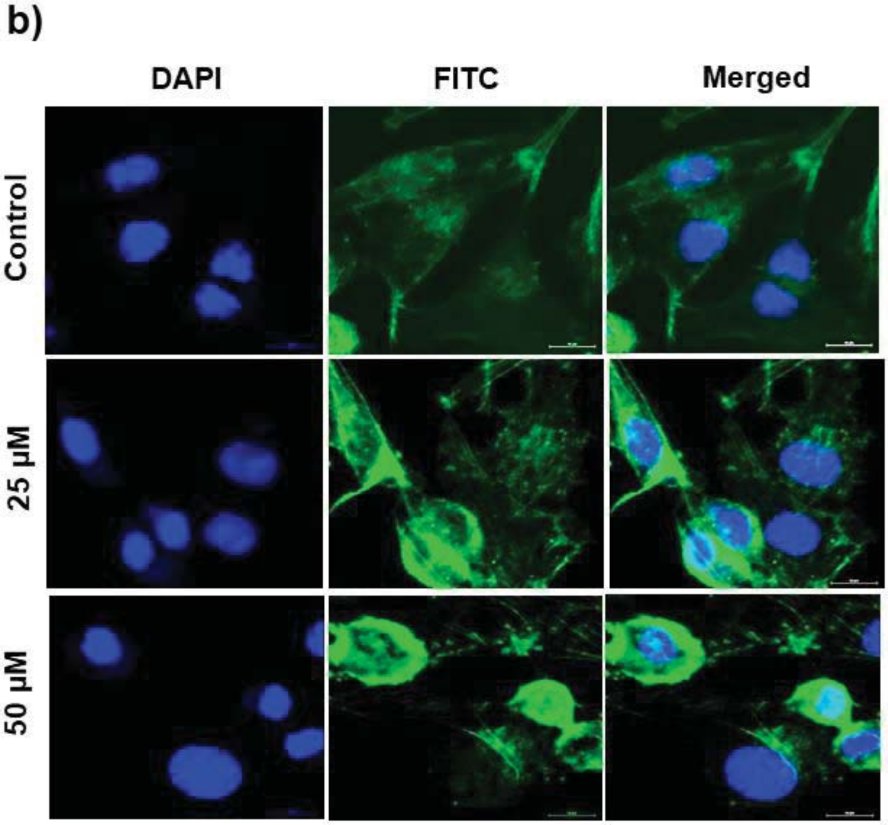

**Figure 4.35. Fluorescence microscopy images show morphology observation in VnNs treated MB-231 cells stained with F-actin specific Alexa 488 dye.** Indicate the cytoskeletal actin filament condensation upon 48 h treatment. Scale bar indicates 100 µm.

## 4.5.10. Membrane morphology analysis through scanning electron microscopy

The onset of apoptotic events is marked by membrane blebbing, which allows the extrusion of damaged organelles along with a portion of the cytoplasm without damaging the neighbouring cells. Scanning electron micrographs clearly show the presence of these membrane blebs, which further proves the mechanism of cell death via apoptosis in 48 h; VnNs treated MB-231 cells **Figure 4. 36.**

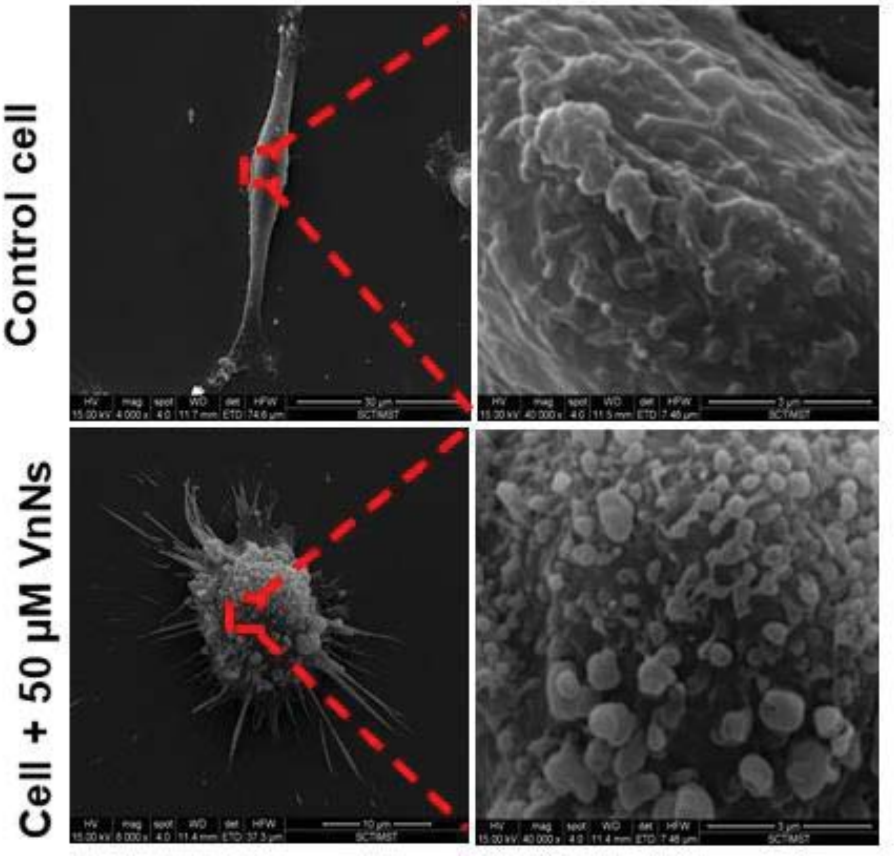

**Figure 4.36. Surface morphology analysis through scanning electron microscopy in VnNs treated MB-231 cells.** Micrographs depict the surface morphology of the control cell, and the characteristic membrane blebs in 48 h VnNs treated cells. Magnified image is with a 3 µm scale bar.

### 4.5.11. Transmission electron microscopy observation on 48 h VnNs treated cells.

The electron micrographs on the 48 h VnNs treated cells showed visible DNA condensation, chromatin disintegration, and nuclear membrane fragmentation. While these changes were absent in the untreated control cells **Figure 4. 37**. The red arrows indicate the dissolution of nuclear membrane in VnNs treated cells.

Together with these observations, the darkly stained lysosomal compartments show pattern of acidification and the presence of acidic vesicles were seen towards the periphery of the distorted nuclear membrane in the 48 h treatment group.

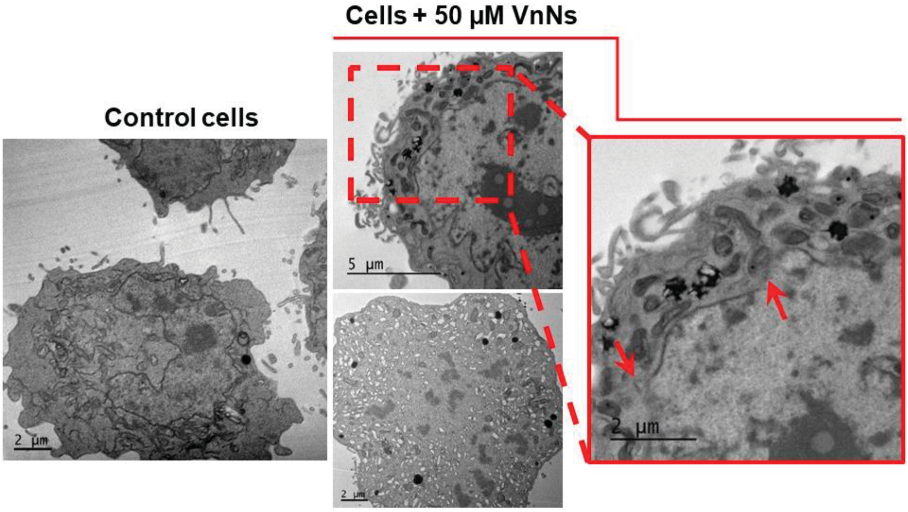

**Figure 4.37. Transmission electron micrographs of VnNs treated MB-231 cells.** The micrographs depict changes in the ultrastructural pattern of the nuclear membrane and pattern of chromatin condensation in the 48 h treated and untreated cells.

### 4.5.12. Fluorescence microscopy on DNA condensation pattern and nuclear fragmentation

Chromatin condensation and break down is considered as a hallmark characteristic of apoptotic cells. The 48 h VnNs treatment resulted in an increase in the number of cells showing chromatin condensation and chromatin fragmentation in comparison with their corresponding untreated control group of cells. Fluorescent images clearly depict apoptotic nuclei in 48 h VnNs treated cells when stained with DAPI **Figure 4. 38**. The field image shows a representative of five different fields from the same treatment condition.

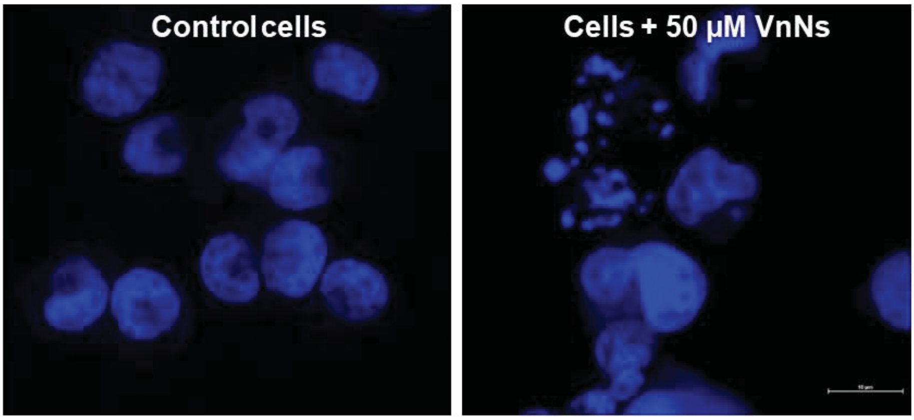

**Figure 4.38. The nuclei of 48 h VnNs treated cells stained with DAPI.** Images indicate chromatin condensation and fragmentation upon 50 µM treatment. Scale bar show 10 µm.

These are characteristic of the process of apoptosis; hence, through these experiments, the property of VnNs to inhibit MB-231 cells was very well proved. Moreover, for efficient cancer management, one needs to address the issue of cancer cell metastasis, as well. Therefore, the ability of VnNs to inhibit cancer migration *in vitro* was further evaluated in MDA-MB-231 breast cancer cells.

### 4.5.13. *In vitro* cell migration assay

Cancer cell metastasis, a significant setback in cancer management, was studied by evaluating the potential of VnNs to inhibit the migration of breast cancer cells. An *in vitro* wound-healing assay showed that the wound created on confluent monolayers of MDA-MB-231cells, upon treatment with 12.5, 6.25 and 3.125 µM VnNs, showed the persistence of the wound/patch even after 72 h of nanomaterial treatment, indicating the potential of the nanomaterial to inhibit cancer cell proliferation and migration *in vitro*. While the wound created in the untreated cell population found closed by the end of 24 h after the injury has created **Figure 4. 39**.

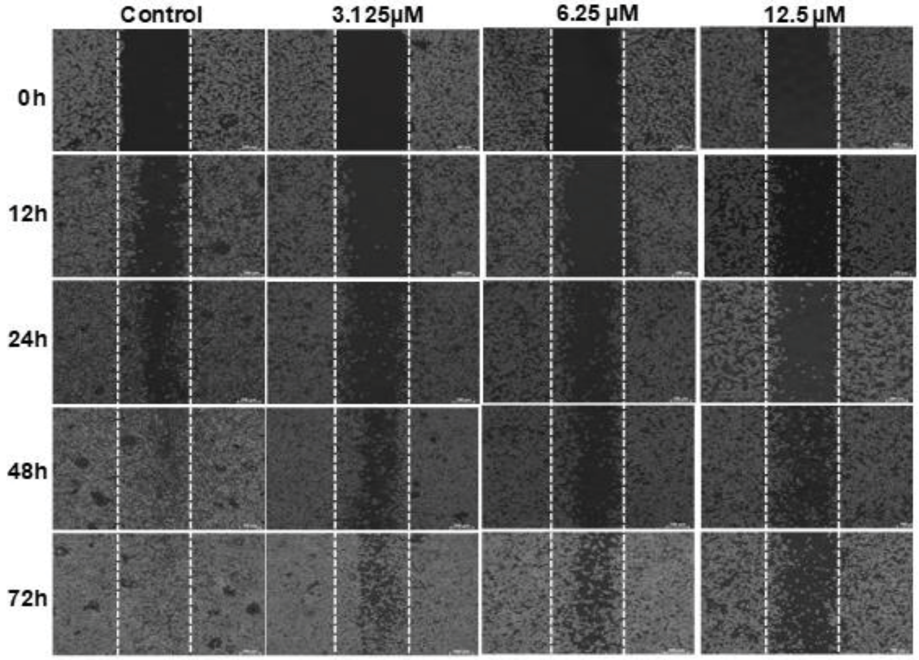

**Figure 4.39. VnNs mediated inhibition on cell migration in a wound-healing assay.** The patch did not seal even after 72h post-treatment, while the control showed efficient cell migration *in vitro*.

Ectopic cancer progression arise from a single cancerous cell that has immense potential to generate colony of cells leading to tumor formation. Hence studied the ability of VnNs to inhibit colony formation through an *in vitro* colony formation experiment.

## 4.5.14. Colony formation assay

The colony formation assay was performed on MB-231 cells to evaluate the ability of single cells to survive VnNs treatment and multiply into colonies. The results indicated that the VnNs treatment inhibited cell survival and proliferation indicated through reduced colony formation ability of treated cells **Figure 4.40**. The 50 & 100 µM VnNs treatment resulted in the complete elimination of cells from the plate; this observation further supports the potential of VnNs to be used in controlling cancer progression by inhibiting tumor formation.

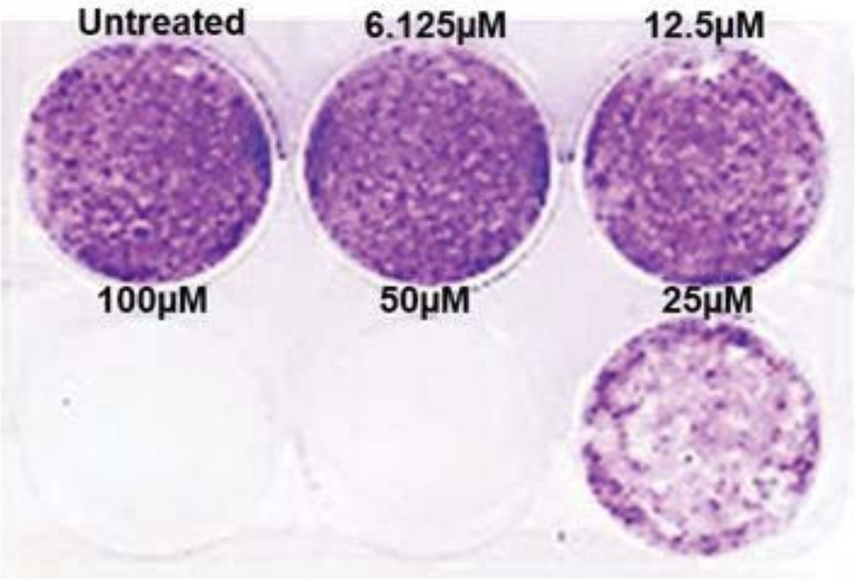

**Figure 4.40. *In vitro* inhibition on colony formation with VnNs.** The 50 & 100 µM of VnNs treatment did not leave even a single cell colony in the plate, while lower concentrations showed comparatively less number of cell colonies *in vitro* in comparison with the untreated control.

Through all the above results, an idea on the possible applicability of VnNs using cancer cells was established. Further, we have also attempted to see their probable interactions *in vivo* using healthy animal models. Normal healthy Swiss albino mice were adopted to gain an idea on the effect of VnNs on its biodistribution in vital organs, metabolism, excretion, and any significant profiles of oxidative stress in excretory organs.

## 4.6. *In vivo* biological interactions of VnNs on Swiss albino mice

### 4.6.1. The acute response towards VnNs administration

Adopted female Swiss albino mice with a single dose VnNs (1 mg/kg body weight) intravenous (*i.v.*) administration for the study. None of the animals displayed any signs of clinical illness, stress response, or any other symptoms like motor, convulsion, reflexes, respiratory, cardiovascular signs, salivation, or gastrointestinal reactions throughout the experimental phase. Observed no adverse reactions or deaths during the trial period. The gross observation indicated no abnormalities in any of the treatment groups.

### 4.6.2. Body weights of experimental animals

The experiment used animals weighing 25 ± 3 g and monitored their body weights throughout the investigation period. By the end of 21 days of post-exposure, the animals weighed an average of 27 ± 2 g that was comparable with that of the control animals. There was no statistically significant difference in the body mass of animals administered *i.v* with VnNs until 21 days of experiment completion.

### 4.6.3. Monitoring clearance of VnNs through urine

Analysed the urine samples collected from the experimental mice using Raman spectroscopy, which validated the presence of vanadium in samples obtained at various time points. The prominent symmetrical C-N stretching bond of urea at 1006 $cm^{-1}$ in the pre-treatment urine samples and metal-oxygen vibration of VnNs at 995 $cm^{-1}$ in the post-treated samples were considered at various time points starting from 1 h of injection (**Figure 4.41**). The interaction between VnNs and urea resulted in the peak shift of V-O stretch from 995 to 944 $cm^{-1}$. The peak corresponding to V-O stretch gradually increased until 72 h of VnNs treatment while that of urea gradually decreased. Post three days, the urea peak ultimately regained its position, whereas the very weak V-O peak at 72 h indicated VnNs clearance.

There was no presence of VnNs in the urine by the 21st day, indicating the first round clearance mechanism of vanadium through kidneys.

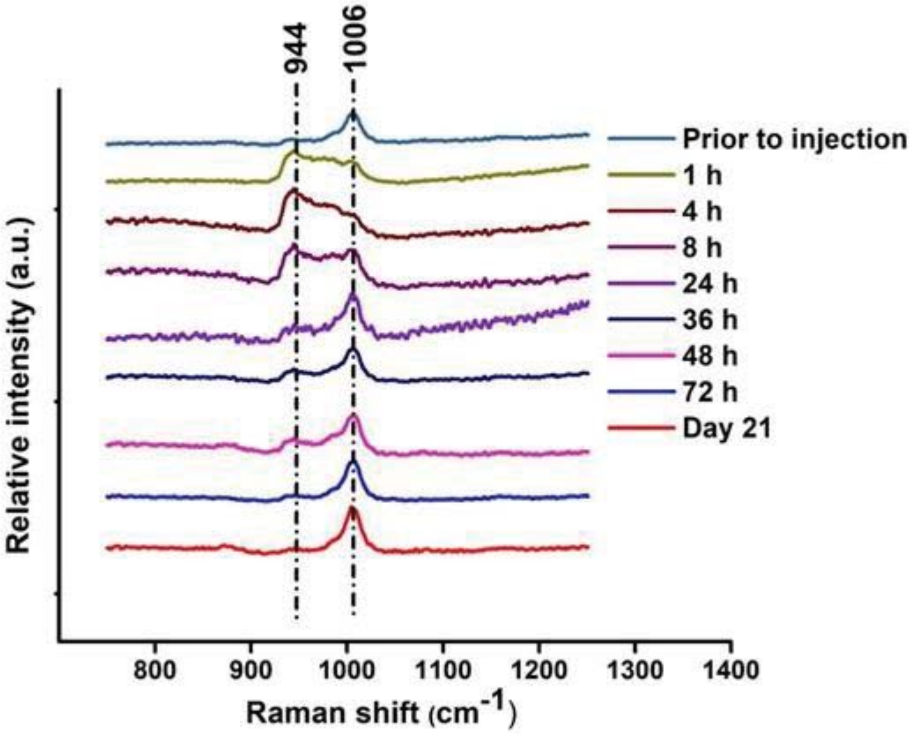

**Figure 4.41. Raman spectra from urine samples of pre and post VnNs treated mice.** The spectra show a prominent urea peak in the urine samples collected from animals prior to VnNs injection and a peak shift in samples after VnNs treatment collected at different time points.

### 4.6.4. Hematology and biochemistry parameters

Subjected the blood samples from the VnNs treated animals collected at day-1, day-3, and day-21 post-injection to various hematology and biochemistry parameters. The results on the blood parameters like total blood cell count, blood cell volume, hemoglobin content, and platelet count remained in the normal range and were comparable with that of untreated control animal values (**Table 4.2)**. In addition, blood analysis studies revealed elevated WBC levels in the treatment group in comparison with the untreated control population.

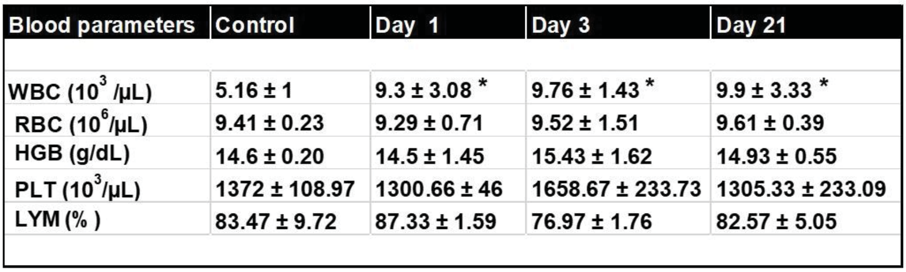

| Blood parameters | Control | Day 1 | Day 3 | Day 21 |
|---|---|---|---|---|
| WBC ($10^3$ /μL) | 5.16 ± 1 | 9.3 ± 3.08 * | 9.76 ± 1.43 * | 9.9 ± 3.33 * |
| RBC ($10^6$/μL) | 9.41 ± 0.23 | 9.29 ± 0.71 | 9.52 ± 1.51 | 9.61 ± 0.39 |
| HGB (g/dL) | 14.6 ± 0.20 | 14.5 ± 1.45 | 15.43 ± 1.62 | 14.93 ± 0.55 |
| PLT ($10^3$/μL) | 1372 ± 108.97 | 1300.66 ± 46 | 1658.67 ± 233.73 | 1305.33 ± 233.09 |
| LYM (% ) | 83.47 ± 9.72 | 87.33 ± 1.59 | 76.97 ± 1.76 | 82.57 ± 5.05 |

**Table 4.1. Blood analysis for various hematology parameters in experimental mice.** Shows variances between blood samples of control and VnNs treated mice. All the values are expressed as mean ± SD, n=4

Further, there were no noticeable alterations in the biochemistry parameters as well, like creatinine, urea, aspartate aminotransferase (AST) & alanine aminotransferase (ALT) levels found comparable with that of the untreated control animal groups even in the 21-day post-exposure group suggesting normal blood parameters between the treated and untreated groups **(Table 4.3)**. However, the cholesterol levels were observed to decrease in blood towards day 3 and day 21 of post-exposure.

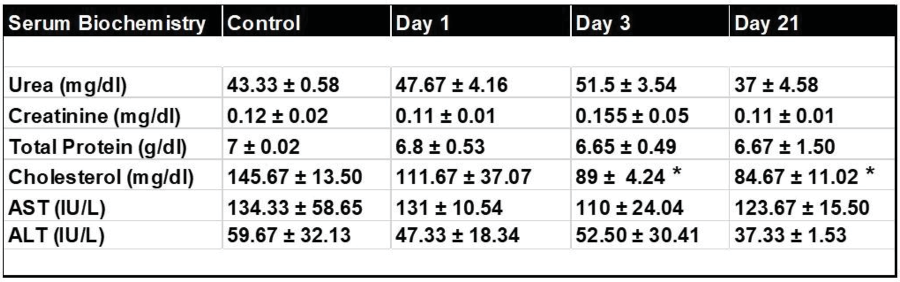

| Serum Biochemistry | Control | Day 1 | Day 3 | Day 21 |
|---|---|---|---|---|
| Urea (mg/dl) | 43.33 ± 0.58 | 47.67 ± 4.16 | 51.5 ± 3.54 | 37 ± 4.58 |
| Creatinine (mg/dl) | 0.12 ± 0.02 | 0.11 ± 0.01 | 0.155 ± 0.05 | 0.11 ± 0.01 |
| Total Protein (g/dl) | 7 ± 0.02 | 6.8 ± 0.53 | 6.65 ± 0.49 | 6.67 ± 1.50 |
| Cholesterol (mg/dl) | 145.67 ± 13.50 | 111.67 ± 37.07 | 89 ± 4.24 * | 84.67 ± 11.02 * |
| AST (IU/L) | 134.33 ± 58.65 | 131 ± 10.54 | 110 ± 24.04 | 123.67 ± 15.50 |
| ALT (IU/L) | 59.67 ± 32.13 | 47.33 ± 18.34 | 52.50 ± 30.41 | 37.33 ± 1.53 |

**Table 4.2. Blood analysis of various biochemistry parameters in experimental mice.** Shows variances in blood samples between control and VnNs treated mice. All the values are expressed as mean ± SD, n=4.

### 4.6.5. Effect of VnNs on the size and gross weight of internal organs

The wet weights of vital organs collected from the animals, the overall size of the internal organs from VnNs treated animals, and saline-injected animals were compared. There were no significant observable changes in the organ size and weights in any single group or between the experimental animal groups **(Table 4.4)**.

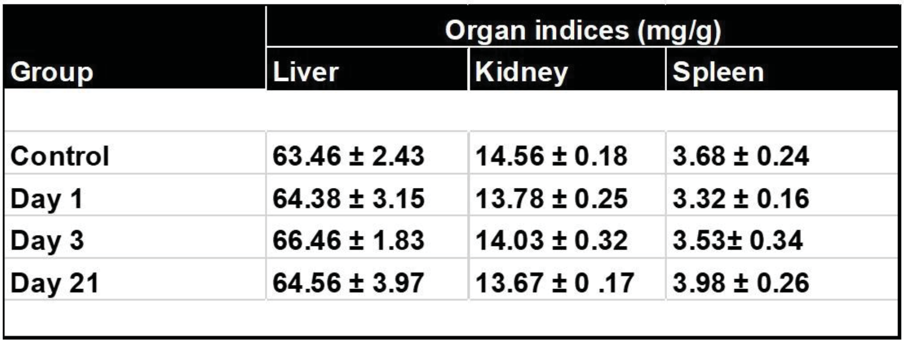

| Group | Organ indices (mg/g) | | |
|---|---|---|---|
| | Liver | Kidney | Spleen |
| Control | 63.46 ± 2.43 | 14.56 ± 0.18 | 3.68 ± 0.24 |
| Day 1 | 64.38 ± 3.15 | 13.78 ± 0.25 | 3.32 ± 0.16 |
| Day 3 | 66.46 ± 1.83 | 14.03 ± 0.32 | 3.53± 0.34 |
| Day 21 | 64.56 ± 3.97 | 13.67 ± 0 .17 | 3.98 ± 0.26 |

**Table 4.3. Organ indices of liver, kidney, and spleen of mice treated with and without VnNs.** All the values are expressed as mean ± SD, n=4.

### 4.6.6. Bio-distribution of VnNs

The excretory organs like the liver, spleen, and kidney from all the animals in the study were quantified for understanding the residual levels of VnNs using ICP-OES analysis. The liver samples indicated 0.014 parts per million (ppm), 0.065 ppm, and 0.036 ppm of vanadium in the 1, 3, and 21-day post-treatment samples **Figure 4.42.** The levels were maximum in the day-3 sample indicating the possibility of its persistence in the blood until deposition, and the levels declined towards day-21, which attributed to particle elimination. The spleen samples showed traces of vanadium, with 0.017 ppm towards day-21 **Figure 4.42.** While none of the kidney samples showed detectable levels of vanadium in any of the time points.

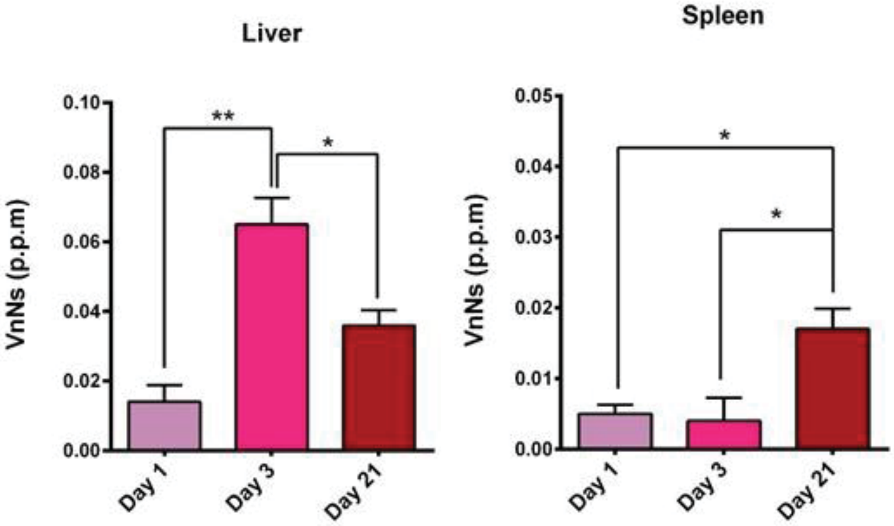

**Figure 4.42. ICP analysis of the liver and spleen samples from VnNs treated mice.** The results indicate the presence of traces of elemental vanadium at various time points. Data represent error bar shows S.D, where n=4, $^{**}P < 0.01$ & $^{*}P < 0.05$.

## 4.6.7. Influence of VnNs on the levels of stress response mRNA

The level of antioxidants present in any cell directly indicates the environmental stress that the cells tolerate at that point in time. For this, the levels of various stress response mRNA like SOD's and catalase from the organs of VnNs injected and saline-injected animals were compared using real-time PCR experiments. Focussed on seeing whether VnNs treatment elicited any stress response in these organs at various time points. The pattern of SOD's and catalase from liver, kidney, and spleen was analyzed to monitor the extent of nanomaterial induced stress responses *in vivo*. The transient mRNA levels of these genes specify the redox status of particular organs involved in the elimination process. The low levels of SOD1, 2, 3, and catalase mRNA in the day-1 liver samples indicated no immediate stress response in the liver **(Figure. 4.43)**. An increase in levels of all the 3 SOD's and catalase mRNA was observed towards day 3, indicating delayed response towards VnNs treatment. Interestingly, it was found that all these mRNA levels dropped back to normal by day-

21 in liver samples. This observation points out that in spite of the presence of traces of VnNs within the liver, even after 21 days following a single dose exposure, the organs still maintained a healthy redox balance and hepatic function.

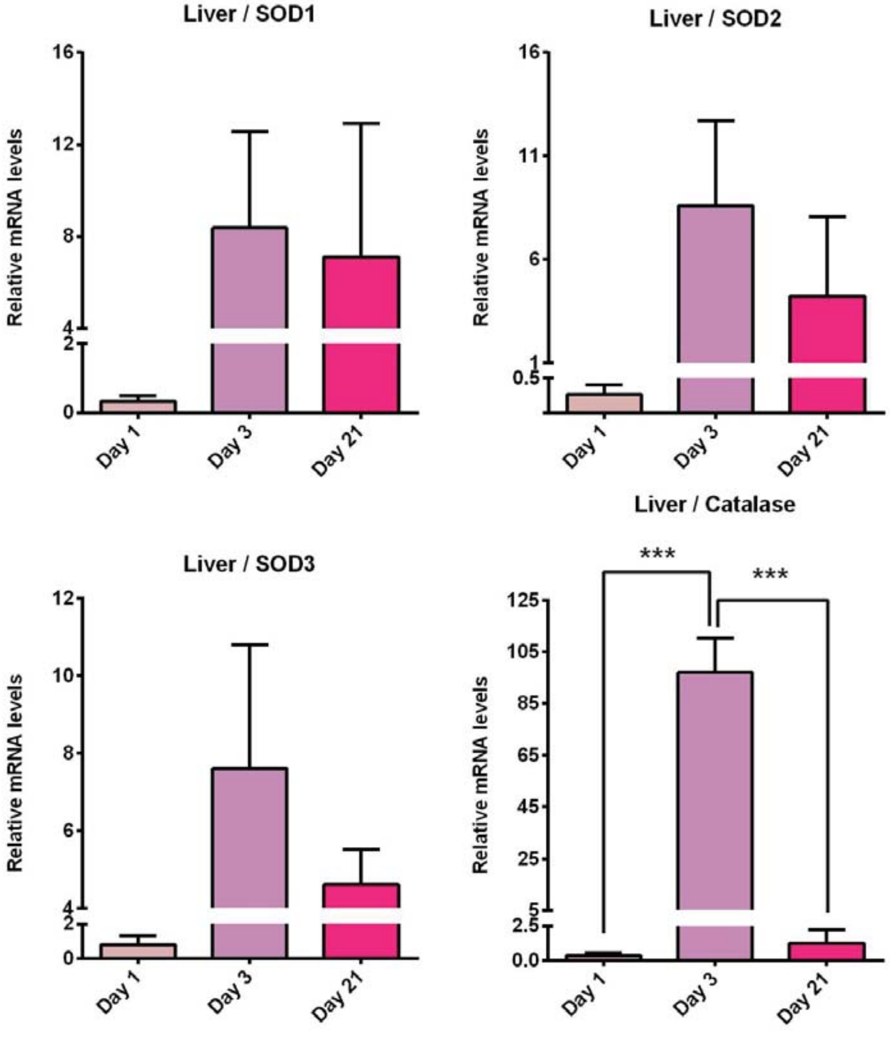

**Figure 4.43. RT-PCR analysis of the relative mRNA levels of SOD's and catalase in the liver samples.** Error bar indicates S.D, where n=5, ****P < 0.0001, ***P < 0.001, **P < 0.01 & *P < 0.05.

The kidney samples showed a rise in the mRNA levels of all the three SOD's and catalase in the day-1 sample, that was found subsided towards day-21 **Figure. 4. 44**. This observation indicated the absence of any delayed stress response in the kidneys and thus proved the renal safety aspects of VnNs.

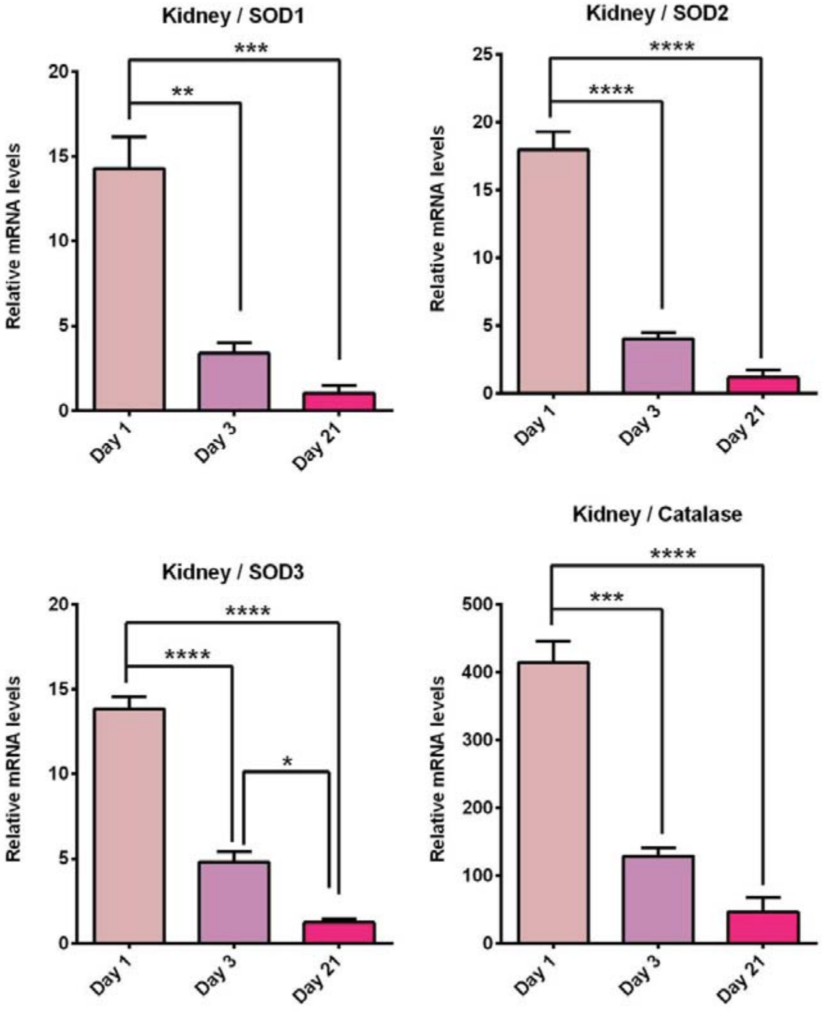

**Figure 4.44. RT-PCR analysis on relative mRNA levels of SOD's and catalase in the kidney samples.** Error bar indicates S.D, where n=5, ****P < 0.0001, ***P < 0.001, **P < 0.01 & *P < 0.05.

The relative levels of SOD's and catalase in the spleen samples also indicated basal redox mRNA levels in day-1 samples. Moreover, all the mRNA levels showed a significant reduction in its levels by the end of day-21 of post-exposure (**Figure 4. 45)**, indicating the absence of VnNs induced stress response in the spleen.

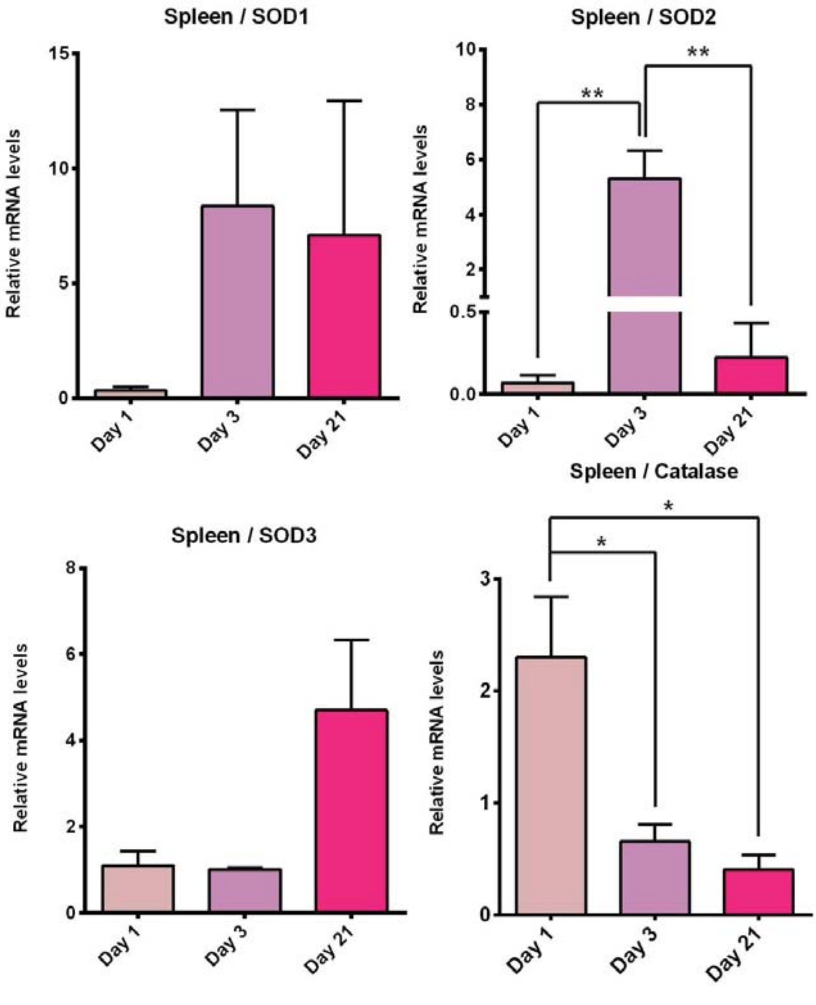

**Figure 4.45. RT-PCR analysis on relative mRNA levels of SOD's and catalase in the spleen samples.** Error bar indicates S.D, where n=5, ****P < 0.0001, ***P < 0.001, **P < 0.01 & *P < 0.05.

### 4.6.8. Enzymatic assay for superoxides

The biological system encounters oxidative stress when there occurs an imbalance between the generation and dissimilation of ROS and the antioxidant defense mechanism. The cells employ a variety of antioxidant enzymes to maintain the redox state of cells. Among which SOD plays a vital role in being one among the defense machinery by converting superoxide radicals into molecular oxygen and comparatively less reactive hydrogen peroxide. The liver is the largest internal organ involved in the elimination process; the superoxide enzyme levels in them were measured in samples collected at various time points. It was observed that the levels of SOD enzyme activity showed an increase at its initial levels and thereafter subsided in the kidney samples, whereas the enzyme levels in liver and spleen samples were reasonable and comparable to that of the untreated controls towards the end of 21 days of the experimental period.

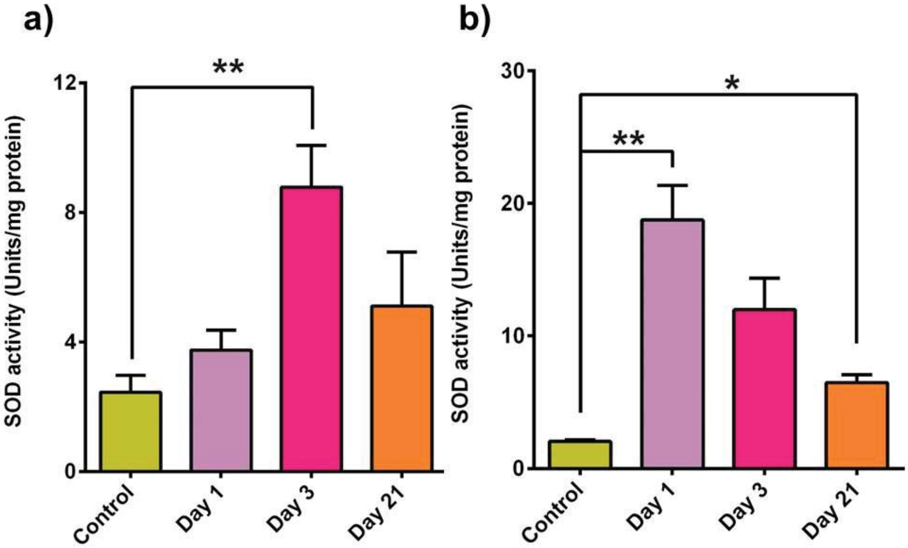

**Figure 4.46. Quantification of the level of total SOD protein.** a) SOD levels in the liver samples at various time points. b) SOD levels in the kidney samples at various time points. Error bar indicates S.D, where n=5, $^{**}P < 0.01$, $^{*}P < 0.05$.

### 4.6.9. Histopathology analysis

As the nanomaterial gets into the circulatory system, they get easily transported and accumulate into various organs like liver, spleen, kidney, etc., where they elicit many responses, oxidative stress, inflammatory responses, and subsequent histology changes. Liver tissues from the saline-injected control group presented standard hepatic chord, portal vein, and hepatocytes with granular cytoplasm and intact nucleus. Bi-nucleated hepatocytes (11 cells/field) were observed around the portal triad and central vein in the periportal region. Kupffer cells and few mononuclear cells (MNC) were noted in the sinusoids. In the case of animals from the treatment groups, the 1 & 3-day post *i.v* injected mice liver exhibited granular cytoplasm and moderate levels of chromatolysis in the nuclei among the hepatocytes that were concentrated around the central vein. Dark black circular cytoplasmic objects were seen in the sinusoids of the 3-day post-injection group. However, the 21-day post-treatment group showed typical cellular arrangements similar to that of the untreated control sample. All the treatment groups had a few MNC's with polymorphonuclear cell (PMC) infiltration and Kupffer cells in the periportal region of sinusoids.

In the kidney samples of the control group, the cortex region involving the glomerulus, Bowman's capsule, proximal convoluted tubules, distal convoluted tubules, and loop of Henle appeared normal. Further, normal histology was observed in the medullar region, involving the collecting tubules and collecting duct. The 1-day post-treated mice showed typical histology pattern with respect to the glomerulus of the cortex and collecting tubules in the medulla of control animals. While the tubular epithelium appeared bulged with a narrow lumen in the proximal convoluted tubule and a normal distal convoluted tubule. The kidney from the 3-day post-exposure animal was observed to have a normal cortex, medullae, and Bowman's capsule. The 21-day post-exposure kidney showed normal interstitium and collecting tubule in the medullar region **Figure 4.47**.

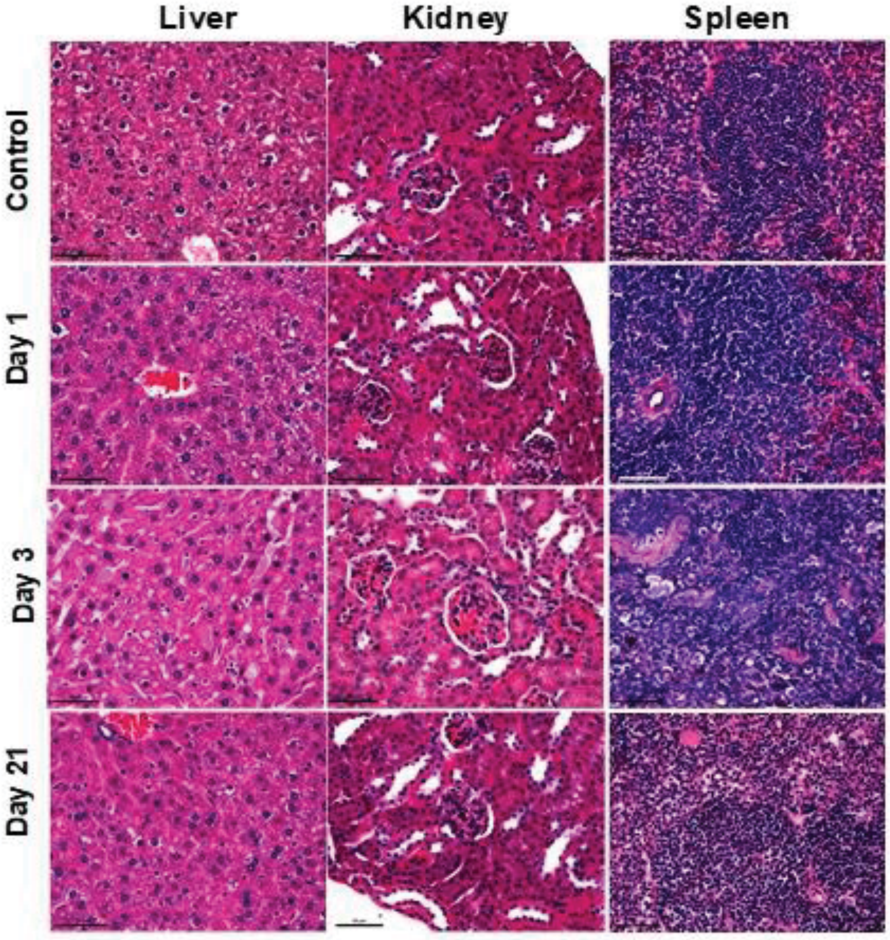

**Figure 4.47. Histopathology of tissue sections from VnNs treated mice.** The H & E stained bright-field optical micrographs depict tissue sections from the liver, kidney, and spleen from the 1mg/kg VnNs injected mice sacrificed at day-1, day-3, and day-21 of post-injection.

Histology of the control spleen showed well-appreciated, distinct red and white pulp regions. The white pulp, germinal center, marginal zone, and lymphoid follicles of spleen appeared normal. In the red pulp region, splenic trabeculae and megakaryocytes were seen. The 1-day post-injected animals also showed similar histology as that of the untreated control spleen. However, the 3-day treated mice showed basophilic staining pattern and edema. The cellularity was less in both white and red pulp regions. Interestingly the 21-day post-injected spleen showed a morphology similar to that of the control group with clear red and white pulp region and lymphoid proliferation, **Figure 4.47**. Overall, the study did not observe any significant alterations in the histology sections of the liver, kidney, and spleen from VnNs administered mice over 21days of post-exposure.

# CHAPTER – 5

# 5 DISCUSSION

The current chapter gives a detailed discussion of the results mentioned in chapter 4 and for clarity, divided the discussion part into five sections. The initial section presents a detailed description of the technique adopted for the synthesis of vanadium pentoxide nanoparticles. Followed by the explanation of the results obtained with the characterization of the Nps. The chapter also covers a detailed description of the differences in the antimicrobial activity of VnNs and VnNp on representative gram-positive and gram-negative bacteria. In addition, a detailed explanation of the various *in vitro* biological interactions of Vn on mammalian cell culture models and details on it's *in vivo* interactions using the Swiss albino mice model are discussed.

## 5.1. Synthesis of Vanadium pentoxide nanoparticles

Adopted an easy to perform methodology for the synthesis of vanadium pentoxide nanoparticles (Vn). Involved a hydrothermal route where vanadium oxychloride and benzoyl alcohol reacted to obtain the intermediate product, which further subjected to calcination, obtained nano-sized vanadium pentoxide of either spherical morphology (VnNs) or plate-like morphology (VnNp). Achieved this by adjusting reaction conditions and parameters for the synthesis process, which yielded highly water dispersible “Nano” vanadium.

## 5.2. Physico-chemical characterization of Vn

The final vanadium-based nanoparticles were obtained by calcinating the intermediate product achieved from the hydrothermal reaction. The intermediate product was subjected to TGA analysis to find the optimum temperature for nano vanadium pentoxide formation through calcination. The high-temperature material heating in this technique showed weight loss, which is characteristic of the loss of impurities and traces of solvent material used in the synthesis procedure. An initial drop in weight-denoted the loss of ethanol and water. Further, a 30 % reduction in the weight at 376 °C, denoted loss of benzoyl alcohol. The weight of the material remained stable thereafter. Evaluated thermal properties of the inert material through DSC, for its crystallinity and glass transition phases during thermal processing. Further, the DSC curve denoted a phase formation with an exotherm at 376 °C necessary for the formation of vanadium pentoxide. Further observed an endothermal peak at 572 °C, denoting a phase transition corresponding to the formation of elongated structures. Further, an endothermic peak at 672 °C indicated the melting of the product, which goes well in hand with the previous reports (Prześniak-Welenc *et al.*, 2015). These analyses gave an idea of optimizing the calcination temperature used for the formation of nano vanadium pentoxide. Hence, out of curiosity, we further evaluated the morphology characters of the nanoparticles produced at 376 °C and 572 °C.

The Field emission scanning electron microscopy revealed sphere-like (VnNs) and plate-like (VnNp) morphology of the samples calcined at 376 °C and 572 °C, respectively. In addition, the EDX analysis marked the only presence of vanadium and oxygen in both the samples, clearly indicating high sample purity and efficiency of the calcination process in removing the reactants. Precisely, the shape of the nanomaterials confirmed with the help of Transmission electron microscopy indicated VnNs with an average particle size of 50 nm and VnNp with a length of several micrometers and a 1 nm width between layers. Small-sized nanoparticles have more surface area and surface reactivity. In addition, Np's with sharp edges pierce the cellular membranes more efficiently than Np's with smooth surfaces, attributing to their physiological activity.

The hexagonal diffraction pattern through SEAD analysis revealed the monocrystalline nature of VnNs and VnNp. VnNs showed diffuse concentric rings, attributed to small-sized particles. Further, multiple spotted patterns were observed in VnNp, which is attributed to the numerous layers found with VnNp through the TEM images, which also indicated that the crystal is devoid of any crystal defects, also signifying the disordered layer structure in the VnNp (Chan *et al.*, 2007).

Studies on the particles dispersed in a solution established strong dipole interactions with the dispersant medium. This represents the hydrodynamic diameter of the particle and indicates the colloidal stability, which are essential factors influencing the biological activity of the nanomaterials. The present study determined the hydrodynamic diameter of both the particles by DLS measurements. The hydrodynamic size of VnNs averaged in 100 – 200 nm range, at different nanomaterial concentrations, used. Due to their large structures in the VnNp samples, they did not qualify for the hydrodynamic size measurement using this method. There is an inverse relationship between the material size and surface reactivity, which marks the critical feature of the nanoparticles and make them stand different from their bulk counterparts. The VnNs exhibited a smaller size than that of the VnNp, and this feature explains the higher reactivity of these nanomaterials over VnNp. The polydispersity index (PDI) value indicates the extent of homogeneity of the samples used. In this case, the PDI value of VnNs was near to 0.1, indicating moderate homogeneity in the sample suspension. Another factor influencing the nanomaterial biological property is their surface charge, which determines the efficacy of nanomaterial uptake into the biological system and subsequent alterations caused in the molecular pathways. It was noted from many of the previous reports that the cationic or positively charged particles have high profiles of cytotoxicity and they were more likely to damage RBC's, WBC's and platelets than neutral or negatively charged (anionic) particles (Nel *et al.* 2009). Both the materials of the study, VnNs and VnNp, exhibited a net negative charge of -13 and -21 MeV, respectively, at the physiological pH. The study observed efficient VnNs cellular uptake in cancer cells, attributed to the high metabolic activity of these cells and enhanced Np uptake. Further, morphology evaluation on G+ and G- microbes further proved changes in the cell membrane caused due to Np interaction, which attributed to the surface charge, and shape of these particles (detailed in section 5.4)

XRD analysis identified the crystal structure and corresponding diffraction signals by comparing it with the diffraction pattern with the PDF database. The pattern correlated well with the PDF 00-041-1426 value, which strongly indicated the monocrystalline, orthorhombic, sherrabanite structure for both VnNs and VnNp. The narrow peaks in the spectra indicated the high crystallinity of the samples and its

"Nano" nature. The peaks in the XRD pattern denote crystal growth and orientation of atoms in different XYZ planes. In addition, the growth pattern at 001 and 110 planes of crystals are responsible for the difference in particle morphology. The catalytic activity of vanadium pentoxide varies concerning the planar arrangement of vanadium and oxygen, where the fastest growth takes place in the 010 plane and weakest growth in the 001 plane. Further, the 010 facet indicated the most reactive plane and 001 plane the least (Ghosh *et al.*, 2018). The crystal growth of atoms in these planes contributes towards the reactivity of Vn in the biological system. $V_2O_5$ is the most stable oxide system in vanadium, having different polymorphs, such as orthorhombic, monoclinic, or tetragonal.  Correlating with the DSC pattern, the exotherm at 376 °C, associate with the starting of vanadium crystallization, forming α- $V_2O_5$ structure. In addition, the peak at 572 °C, attributed to the phase formation of β- pattern. The increase in the intensity of XRD pattern with an increase in calcination temperature to 572 °C revealed formation of α- $V_2O_5$, since the β- $V_2O_5$ structures are less stable, and they get converted back to the α- $V_2O_5$ structures during the cooling step of calcination procedure (Prześniak-Welenc *et al.*, 2015). Even though the PDF value correlated well with the database of 00-041-1426, indicating the orthorhombic structure, it could be possible that the sample-contained traces of β-pattern also.

As per the reports of Hryha *et al.*, the oxidation state of $V_2O_5$ is determined from the difference between the binding energies of core O1s and the $V2p_{3/2}$ (Hryha, Rutqvist and Nyborg, 2012). The two components in the XPS spectrum around 517eV and 530 eV corresponds to the $V2p_{3/2}$, and O1s respectively, which indicated the sample purity and confirmed the +5 - oxidation state in both the nanomaterials. FTIR analysis uses infrared light having a longer wavelength and lower frequency to examine different kinds of molecular vibrations corresponding to the chemical components and properties in the test sample. The samples showed typical peaks at 1012 and 846 $cm^{-1}$ matching to the V=O stretch and O–(V) vibrations in both VnNs and VnNp. While the peak at 668 $cm^{-1}$ in VnNs showed a shift towards 675 $cm^{-1}$ in VnNp, which could be possibly attributed from any traces of β- $V_2O_5$ structures (Venkatesan *et al.*, 2013; Prześniak-Welenc *et al.*, 2015).

The complementary Raman analysis involves the interaction of light with chemical bonds of materials that scatter light. These characterization techniques showed characteristic metal-oxygen stretching and bending vibrations confirming the formation of unique bonds in vanadium pentoxide. Typically the hallmark peak at 993 $cm^{-1}$ denoting the V=O stretching vibrations is found in both VnNs and VnNp, respectively (Šurca and Orel, 1999). The peak is considered as the most stable peak that involves the terminal unshared oxygen atom denoting V-oxo, which was considered later in the studies to prove VnNs internalization in mammalian cells.

## 5.3. *In vitro* interactions of Nano vanadium on cell lines

### 5.3.1. Endotoxin detection

It is of prime importance to analyze nanomaterials for the presence of any traces of bacterial endotoxin, which otherwise could result in false-positive toxicity profiles. In the current study, the endotoxin content in the NP's was observed to be well below the USP instructed limit for biomaterials for both VnNs and VnNp (Smulders *et al.*, 2012).

### 5.3.2. *In vitro* cell viability assay on cell lines

Cell viability as a function of nanomaterial interaction is usually established by analyzing mitochondrial health. Mitochondria help the cells to meet the energy needs by involving in ATP production. They are also easily prone to damages from chemical toxicants and xenobiotic by inhibiting the mitochondrial metabolic pathway. "MTT assay value" acts as a function of metabolic activity of any cell, depicts the mitochondrial dehydrogenase activity. The mitochondrial health assayed on MDA-MB-231 cells, and L929 fibroblast cells upon 4 h VnNs treatment showed above 80 % cell viability at all the treatment concentrations used while 24 h treatment resulted in 50 % loss in cell viability and a further decline in cell viability was observed with the 48 h treatment sample **Figure 5.10**. VnNp treatment in MDA-MB-231 cells and L929 fibroblast cells showed a drastic decline in cell number irrespective of healthy cells or cancer cells in use. The cellular response observed towards the two different morphologies suggests that the possible mechanism of action in VnNs treatment towards cells could be a delayed response. VnNp had an immediate response due to its sharp edges; it would have interacted with the cell membrane in a nonspecific manner and accounted for reduced cell viability in both the cells.

Further, the effect of VnNs and VnNp was compared on representative microbial systems, while a detailed study on the effect on the cancer cells was restricted to VnNs alone.

## 5.4. Interaction of Vn on microbial systems

The antimicrobial property of the vanadium-based nanomaterials was evaluated using representative gram-positive and gram-negative microorganisms. The current study involved a brief understanding of various mechanisms by which vanadium pentoxide nanoparticles (Vn) elicit their antibacterial efficacy on representative Gram-positive (G+) and Gram-negative (G-) bacteria with attributes to the nanomaterial shape and sizes. Different concentrations of VnNs and VnNp were used to determine the effects on Staphylococcus aureus (*S. aureus*) and Escherichia coli (*E. coli*) as representative (G+) and (G-) model organisms and possess significant changes in their bacterial membrane architecture.

### 5.4.1. Minimum Inhibitory Concentration of 'Vn' in liquid broth

MIC is the lowest concentration of the drug molecule, which inhibits the visible growth of the bacterium, usually done in liquid broth cultures. The value depends on the type of microorganism, efficiency, and mode of action of the drug molecule. In the present study, the nanomaterials directly interacted with the bacterial culture and were observed to have a significant reduction in optical density as a function of the antibacterial activity of the material under study. These observations indicated a comparatively higher activity of VnNp on *E. coli* cells towards nanoparticle treatment. While *S. aureus* was less susceptible to VnNs treatment when compared with the *E. coli* culture. Mainly this observation is attributed to the characteristic morphology of the VnNp with sharp edges that aid in piercing the bacterial cell membrane, thus resulting in the observed antibacterial activity. Vanadium nanowires were also reported to have a bactericidal activity, which is attributed to their surface morphology (Sharma *et al.*, 2010). Another possibility is attributed to the difference in membrane architecture between the bacterial species. *E. coli* being G- bacteria possess a thin peptidoglycan layer and *S. aureus* being G+ maintain a thick layer of peptidoglycan, which is responsible for hindrance of materials from entering inside the cells. The membrane undergoes continuous changes that make alterations in the cell membrane architecture and contribute towards the emergence of drug-resistant bacterial strains such as Methicillin-resistant Staphylococcus aureus (MRSA).

### 5.4.2. Disc diffusion assay

In this technique, the bacterial zone of inhibition as a function of antibacterial activity is measured in agar plates. Interestingly, it was surprising to observe no bacterial zone of inhibition or clear zone of inhibition against these gram-positive and gram-negative bacteria with either VnNs or VnNp **Figure 5.11**. This could be attributed to the binding of vanadium nanoparticles with the cellulose content in the discs that rendered these particles difficult to diffuse out of the discs. However, the antibacterial activity evident from the liquid broth experiment further was utilized to understand the mechanism of activity.

### 5.4.3. Bacterial surface morphology through electron microscopy

Modifications instigated in the bacterial morphology upon treatment with vanadium-based nanoparticles examined with an FE-SEM revealed remarkable membrane alterations in both *E. coli* and *S. aureus* samples treated with VnNp **Figure 5.12**. VnNp interacted with the bacterial cell membrane in *E. coli*, by inducing physical damage with their sharp edges attributed to specific surface morphology (Dizaj *et al.*, 2014). The presence of an outer membrane and thin peptidoglycan layer possibly allow these VnNp to cause alterations in the phospholipid membrane, thereby enabling VnNp to enter inside the bacteria, thus impeding osmotic balance and activated subsequent cell death. However, VnNs treatment did not induce any such membrane damage in either of the organisms utilized, which could be attributed to the spherical shape of the nanomaterial. In a general scenario, any form of spherical nanoparticles exhibit a cell-friendly nature (Geng *et al.*, 2007); similarly, in this case, attributed to their shape, VnNs failed to pierce these microbes. Thus, the bacteria maintain an intact cell morphology after vanadium nanosphere treatment. Even though *E. coli* had a more negative cell surface, these bacteria responded well to the negatively charged VnNp than *S. aureus*. Thus overall indicated that VnNs treatment resulted in comparable morphology corresponding to both the untreated bacterial cell populations, and VnNp treatment resulted in cell membrane disruption in *E. coli* bacteria. These observations clearly displayed that the antibacterial effect of Vn is attributed to the combinatorial effect of the surface morphology of nanoparticles as well as the difference in bacterial membrane architecture (Doshi and Mitragotri, 2010). The EM results were again validated to have an understanding of whether Vn induced any changes in the structural components of the bacteria through Raman spectral mapping on Vn treated bacterial cells.

### 5.4.4. Raman spectral analysis

Each biomolecule possesses specific Raman peaks and is considered as a fingerprint of that particular molecule. Any membrane damage or physical damage caused by the nanomaterial, make it more susceptible to nanomaterial uptake and allow their possible interaction with the cellular components like protein and DNA. *E. coli* possesses a thin peptidoglycan layer with an outer membrane, which upon treatment with nanoscale vanadium pentoxide, showed drastic alterations in the Raman spectral pattern in comparison with the signals from the untreated control population. While the *S. aureus*, with a thick peptidoglycan layer, resulted in only minor changes in the Raman spectra **Figure 5.13**. This could possibly be attributed to the difference in bacterial membrane composition, which makes the organism more or less susceptible to the external environmental treatment conditions. A thick peptidoglycan layer in the G (+) bacteria renders them more resistant to membrane damages thereby, restricting the entry of nanomaterials into the bacterial cells, which could also account for slight alterations in the Raman signal peaks and its intensity. In our experiment, we observed apparent modifications in the peak positions and the peak intensity with the 1 mM VnNp treatment in *E. coli* cells.

In addition to the intrinsic membrane attributes of the bacteria, specific properties about the nanomaterial like its shape also contributed towards the antimicrobial property. VnNp with the sharp edges found to be more effective as an antibacterial agent than VnNs with smooth and spherical morphology, which is in correlation with the previous reports (Xiao, Wang and Yu, 2013). The VnNp was observed to interact with the bacterial outer membrane in G (-) *E. coli* species and was evident from the Raman peak position and intensities. It could be possible that the interaction between 1mM VnNp and the peptidoglycan layer have resulted in the decreased Raman signal intensity in the treated *E. coli* sample. In addition, this could have further facilitated the penetration of VnNp into the interior of the bacterial cells, which allowed possible interactions with the intracellular components like the DNA phosphate backbone. This could be a possible reason behind the drastic decrease in Raman peak intensity observed at 1095 $cm^{-1,}$ corresponding to the DNA components (**Figure 5.13**). The observation gave a clear indication that nanomaterial interaction with the DNA might have occurred and could be responsible for such a change in the bacterial Raman signals in the Vn treated *E. coli* sample. The Raman spectra in the VnNs treatment on *S. aureus,* when compared with the UT control group, indicated an insignificant change in Raman signals. The peaks remained unchanged in its position and intensities in the representative gram-positive bacterium, *S. aureus,* even after Vn treatment, which could be due to the presence of a thick peptidoglycan layer. These Raman spectral studies explain the observed antibacterial effect of nanoscale vanadium pentoxide on representative bacterial species. In addition, Raman spectroscopy thereby worked as an excellent tool for studying differences between the intact and disrupted bacteria with the corresponding Raman signals indicating reproducible molecular signatures and can even be used for analytical species identification based on the differences in the outer membrane layer of bacterial species.

### 5.4.5. ROS detection in vanadium treated bacteria

Since we found Vn as a successful antibacterial agent against *E.* coli, they were utilized to study ROS generation in *E. coli* biofilms (Manke, Wang and Rojanasakul, 2013). Here, both VnNs and VnNp treatment on biofilms resulted in ROS generation, monitored through DCF assay. Quantification revealed a statistically significant increase in the levels of ROS, which also tell that the mechanism of antibacterial activity of Nano Vn on *E. coli* cells is through ROS generation. Further, the experiment proved that VnNp was more successful in generating ROS than VnNs, which is attributed to the shape of the nanoparticles. The sharp edges in the VnNp were more efficient to pierce the bacterial membranes and further contributed towards ROS generation in treated bacterial populations.

## 5.5. Details on the *in vitro* biological interactions of VnNs on cell lines

Based on the initial results on the cell viability assay conducted on MB-231 and L929 cells, we were curious to understand the mechanism of action by which the dose and time-dependent activity of VnNs worked on MB-231 cancer cells. For which, the initial cellular uptake studies were conducted.

### 5.5.1. Cellular uptake studies at 4 h of VnNs treatment

VnNs uptake in MB-231 cells was proven with flow cytometry, electron microscopy analysis, and Raman spectral mapping on treated cells in order to validate the effect of Nano-induced effects in the cell culture system.

### ***5.5.1.1. Cellular uptake by flow cytometry studies***

Cellular internalization of VnNs measured changes in the granularity of treated cells by analyzing the forward scatter (FSC) and side scatter (SSC) pattern through flow cytometry. Ojea *et al.* demonstrated that an increase in the SSC and a decrease in the FSC, due to any change in the refractive index of cells indicate increased cellular granularity, which in turn is correlated with the efficiency of nanoparticle uptake or an increase in the number of intracellular organelles (Ojea-Jiménez *et al.*, 2016). In this study, the result indicated a small but consistent and statistically significant increase in the SSC pattern in 4h, 50-µM VnNs treatment in comparison with their respective untreated control population. This gives a clear indication of VnNs uptake into the cells.

### ***5.5.1.2. Cellular internalization through Raman spectroscopy***

The sharp prominent Raman peak observed at 995 cm$^{-1}$ in the 50 µM VnNs treated live MB-231 cell sample at 4h of nanomaterial incubation indicated vanadium oxygen bond, which was absent in the untreated sample. The peak at 996 cm$^{-1}$ is the strongest and least reactive bond among all the other bonds of VnNs (**Figure 5.16**), which could be the reason for the prevalence of this specific bond in the Raman spectral mapping of treated cells. This also reflects the efficiency of nanomaterial uptake within 4h of incubation time (Romero *et al.*, 2011). However, other peaks of vanadium pentoxide were not considered for the cellular study. This is mainly due to the change in the region of interest of the Raman spectra while considering the cellular studies and also due to the chances of masking the VnNs peaks by various cellular signals emerging from numerous other cellular components (Jang, Kang and El-Sayed, 2018).

### ***5.5.1.3. Cellular internalization studies through electron microscopy***

Electron microscopy is an excellent tool to have a detailed understanding of the various cellular organelles, nucleus, membrane ultrastructure, etc. Due to the high electron density, direct visualization of the intracellular localization of VnNs was promising from the electron micrographs (Huo *et al.*, 2016). Typically based on the shape of NP's, they enter into the cells by direct cell membrane disruption or are taken up through non-destructive endocytosis (Song *et al.*, 2015). The nanomaterial uptake through the endocytosis pathway involves the formation of membrane-bound vesicles taking up the cargo along with a portion of the cytoplasm. TEM analysis on the ultra-thin cross-sections of VnNs treated MB-231 cells gave a detailed understanding of its intracellular localization. In general, biological materials are nearly "transparent" to the electrons, and the electron-dense area becomes clearly visible inside the cells through EM (Klionsky *et al.*, 2016). Pertaining to the high electron density of the nanomaterial, we could clearly see efficient nanosphere internalization. EM images evidently showed that VnNs uptake followed vesicle formation, and was observed as small aggregates in the cytoplasm, which indicated efficient nanoparticle entry into the cells (**Figure 4.17**). We also observed mitochondria, compartmentalized within the cytoplasmic extensions called the "phagophores/phagosomes," which denoted the onset of a physiological event named Autophagy. In addition, TEM showed the fusion between autophagosomes and lysosomes, which finally resulted in the degradation of damaged organelles, thereby helping in nutrient recycling. Despite these cellular changes, the 4h VnNs treated cells maintained overall cell and nuclear membrane morphologies. Hence, it adopted various techniques to analyze the level of autophagy induction at various time points of VnNs treatment in MB-231 cells.

## 5.5.2. Autophagy induction studies

### *5.5.2.1. Studies using live-cell time-lapse fluorescence microscopy*

The process of nanoparticle internalization into cells fuel a variety of reactions, as the cells recognize them as foreign materials. These reactions determine the fate of the NP's inside the cells and alter many of the normal physiological functions in several ways. One such process is the induction of a stress response called autophagy (Huang, Zhou and Gao, 2015). A basal level of autophagy is maintained in all cell types as part of normal cellular homeostasis, and it helps to eliminate misfolded proteins, damaged organelles, etc. Apart from the usual case, autophagy is also induced under various stress conditions like growth factor deficiency, hypoxia, or when the cell encounter any foreign materials. Karna *et al.* reported that nanomaterial uptake was followed by the upregulation of various stress response genes like microtubule-associated protein 1 light chain 3 (LC3), which is considered as a gold standard in autophagy evaluation (Stern, Adiseshaiah and Crist, 2012).

In this study, the levels of LC3 were checked using GFP-LC3 transformed MB-231 cell clones. The degree of autophagy induction was studied based on the manifestation of the corresponding number of fluorescent autophagosomes named GFP-LC3 punctuates **Figure 5.19**. The time-lapse imaging revealed the ability of VnNs to induce sharp spots of autophagy specific green LC3 proteins as an initial cell response, while untreated cells showed a diffuse green signal. The signal intensity of the sharp spots faded towards later time points by 24 h, which specified that the autophagy response evoked by VnNs is an initial stress indicator in treated cells. This was also reported by (Barth, Glick and Macleod, 2010).

Autophagy induction also marks a progressive decrease in the mitochondrial number and indicates a loss of mitochondrial membrane potential (MMP). Hence simultaneous evaluation of mitochondrial health was assayed along with GFP-LC3 in the fluorescence microscopy. The untreated control cells showed intact red fluorescence intensity pattern with the TMRM dye, even in the 24 h sample, while the 12.5, 25 & 50 μM VnNs treated cell samples for 24 h indicated low red fluorescence intensity pattern, which could be due to the mitochondrial degradation during the autophagy process. The process of self-eating or autophagy is a method adopted by the cells under stress to gain energy for cellular activities. Further, the levels of LC3 protein were quantitatively measured by western blot assay using nontransfected MB-231 cells treated with VnNs for 4 h.

#### *5.5.2.2. Western blot analysis for LC3 protein detection*

The LC3 protein is persistent and stable in the autophagosomes unless degraded by fusion with lysosomes, and hence the levels of this protein are used to screen the degree of autophagy induction in VnNs treated MB-231 cells. LC3-I and II are different forms of the same protein that switches between the two upon autophagy. Typically, LC3-I remains as free proteins throughout the cytoplasm, and upon autophagy induction, it translocates into the membrane of autophagosomes and forms active conjugation with the membrane-bound phosphatidylethanolamine creating membrane-bound LC3-II. Autophagy, being a highly dynamic process involving transient shuttle between the LC3 I & II, was assayed using a quantitative flux assay. Thus, a commonly used western blot methodology was adopted to estimate the levels of LC3 protein in VnNs treatment-induced autophagy. Chloroquine, a lysosomotropic reagent used to hinder the autophagosome-lysosome fusion by obstructing LC3-II degradation, was used for the flux assay. Chloroquine caused the autophagosome to accumulate in the cytoplasm, and as a result, the specific levels of LC3 - I & II was monitored between the chloroquine blocked and unblocked samples after 4h of VnNs treatment (**Figure 5.20**). The fold increase in LC3 expression was calculated by normalizing the levels of LC3 II to GAPDH levels; the difference in LC3-II levels between samples with and without chloroquine treatment was compared in the flux assay. Hence, a clear indication of autophagy induction was thus proved in 4h VnNs treated cells. Also, high LC3 II levels at different time points until 24 h also proved the prolonged autophagy effects in the treated cells. This kind of autophagy-related gene expression study was also previously reported (Lin *et al.*, 2017). Prolonged effects of VnNs treatment on cellular organelles like mitochondria and lysosomes were further evaluated using electron microscopy.

### 5.5.3. Mitochondrial activity study using fluorescence microscopy imaging

The main organelles affected by autophagy are mitochondria, and any subtle changes in the physiological microenvironment of this organelle hinder ATP production and make cells starve to death. Mitochondrial inter-membrane undergoes a constant flux of ions into and outside the mitochondria, which denote the importance of MMP to generate ATP. The fluorescent dye specific to mitochondrial membrane potential, JC-10 accumulates inside healthy mitochondria forming JC-10 aggregates and gives out red fluorescence in cells that have an intact MMP or the dye remain as monomers in the cytoplasm emitting green fluorescence when they lose their MMP. VnNs accumulation within the mitochondrial matrix resulted in altered mitochondrial membrane potential and is shown quantitatively via flow cytometry and qualitatively through fluorescent microscopy (**Figure 5.22**). A statistically significant rise in the percentage of cells with green fluorescence and a shift in the mean fluorescence intensity from red to green over a treatment period of 24 h, indicated a loss of MMP in VnNs treated MDA-MB-231 cells, which is attributed to VnNs uptake by the cells or due to the uptake of VnNs by the mitochondria. Fluorescence microscopy also revealed active spots of red fluorescence from the intact mitochondria, and the 24 h VnNs treated cells showed a drop in the red fluorescence intensity pattern, which again reconfirmed the observation. An adaptive mechanism exhibited by cells undergoing stress is through the formation of mitochondrial clumps (Rainbolt *et al.*, 2013). The primary function of these mitochondrial clumps (**Figure 5.22 c**) is to work together and satisfy the energy needs of the cells. Surprisingly, the VnNs treated cells showed these kinds of mitochondrial clumps and indicated the effects of damage executed on these organelles by VnNs. In addition, the treatment resulted in mitochondrial membrane damage, which further evoked mitochondrial permeability transition pores (MPTP) and various other stress response mechanisms. The prolonged effect of VnNs treatment on cellular organelles such as mitochondria and lysosomes were further evaluated using electron microscopy.

### 5.5.4. Electron Microscopy analysis on the mitochondria and lysosomes of cells treated with VnNs for 24 h

The electron micrographs showed characteristic autophagy markers like autophagosomes, which comprised of defective and damaged mitochondria. VnNs interaction with the mitochondria caused mitochondrial membrane disruption and allowed Np's to enter into the cells, which eventually hindered their metabolic activity. It was also observed that the nanomaterials found localized within the mitochondria (**Figure 5.23**), and this would have led to mitochondrial dysfunction in the treated cells. These observations could be the reason for a 20 % decline in cell viability in treated cells towards 24 h VnNs in the MTT assay.

In a general scenario, foreign particles enter into the cell through phagosome formation, which carries the cargo to be degraded, by fusion with the lysosomes. They engage lysosomal hydrolases in digesting the endocytosed material in the acidic environment (Luzio *et al.*, 2014). Also, these acidic compartments appear as dark-stained bodies in the electron micrographs, it could be possible that nanomaterial accumulation might have occurred in the lysosomes, but they were not distinguished due to otherwise darkly stained organelle (**Figure 5.26**). The thus formed phagolysosomes observed in the TEM micrographs as dark-stained bodies denoted increased lysosomal size, high organelle dimensions, and perinuclear accumulation in comparison with the untreated control group of cells (Yang *et al.*, 2016). These observations were further validated using the fluorescence microscopy images of lysosomes of treated cells at different time points.

### 5.5.5. Changes in lysosomes through Fluorescence microscopy

Lysosomes act as suicidal bags of the cell and play a pivotal role in maintaining cellular homeostasis by acting as the destination place for the endocytosed cargo to undergo degradation. The lysosomal activity depends on the presence of more than 50 hydrolyzing enzymes; notable one comprises the family of cathepsin proteases (Mindell, 2012). Lysosomes develop mechanisms to maintain an optimal level of lysosomal membrane integrity, which is most important for healthy cell survival. In a typical case, the membrane integrity is maintained pertaining to the presence of heavily glycosylated proteins with complex intraluminal carbohydrate chains (Serrano-Puebla and Boya, 2016). These structures act as efficient obstacle compared to the hydrolytic activity of lysosomal enzymes, which thwart any unintentional release of lysosomal ingredients into the cytosol (Johansson *et al.*, 2010).

This portion of the study focused on understanding the effect of VnNs treatment on vesicular acidification with the help of acidic vesicle specific fluorescent dyes. The results revealed an increase in lysosomal size as evident from the fluorescence images **Figure 5.24** and electron micrographs, which could have resulted from the fusion between phagosome and lysosomes during autophagy. In order to maintain the organelle acidity, lysosomes showed a pattern migration towards the perinuclear site, the most acidic area in the cytoplasm. Once any foreign particle enters the cell, the lysosomal hydrolases engage in digesting the endocytosed or phagocytosed material within the lysosomal/autolysosomal compartment. A ten-fold increase in lysotracker fluorescence in the VnNs treated cells in comparison with the untreated control cells, attributed to the increased lysosomal acidification. Various extracellular or cytoplasmic queues like cellular stress response mechanism towards VnNs treatment could result in increased lysosomal biogenesis or an escalation in its surface area due to increased lysosomal activity (maximum hydrolase activity at pH 4–5). Alternatively, a diverse class of inhibitors like actin microfilament stabilizers, tubulin depolymerizes, and adenylyl cyclase inhibitors prevent lysosomal exocytosis, thereby resulting in an increased number of total acidic components per cell. The increased lysosomal size would foster higher surface tension, which makes lysosomes more vulnerable to leakage or rupture. This lysosomal instability could also lead to the subsequent release of lysosomal hydrolases to the cytosol, which results in lysosomal membrane permeabilization (LMP). Surprisingly in our study, we observed that VnNs treatment increased the lysosomal size, but it never caused lysosomal membrane disruption even after prolonged incubation time points of 48 h, thus preventing the cells from undergoing necrosis. Altogether these results suggest that VnNs treatment on MB-231 cells leads to phagolysosome formation, an increase in number & size of acidic compartments, which points towards the onset of defective autophagy, which could lead to alterations in the cell cycle and further evoke various other stress responses in treated cells.

### 5.5.6. Cell cycle analysis through flow cytometry

Various cell cycle regulators are involved in the tight control of cell division to prevent any progressive accumulation of genetic mistakes in the genome. Among which, the G2/M phase checkpoint performs a critical role in maintaining normal cellular homeostasis and genome stability by inhibiting cell progression towards mitosis if any of the cellular machinery relating to DNA replication is damaged (Liu *et al.*, 2016). The progressive accumulation of cells committed to the G2/M phase indicated cell cycle arrest, and the cells no longer undergo further rounds of cell division **Figure 5.27**. Mechanistically, our data showed that VnNs treatment triggered irreversible cell cycle arrest at the G2/M phase, which could have happened due to any incomplete DNA replication, DNA or mitochondrial damage, or even due to acidic vesicle accumulation subsequent to VnNs treatment. The cell cycle arrest is also marked by higher levels of reactive oxygen species (ROS) in treated cells. Hence, it evaluated the levels of ROS at different concentrations and time points of incubation (Evan and Vousden, 2001).

### 5.5.7. Reactive oxygen species analysis in VnNs treated cells

Studied the effect of VnNs onto the redox balance in treated cells using $H_2$-DCFDA assay by measuring the levels of ROS formed inside the cells. One of the ROS molecules generated inside the cells under stress is $H_2O_2$. Proper functioning of cellular machinery requires continuous redox cycling involving various antioxidant enzymes (Ďuračková and Gvozdjáková, 2008). Major critical antioxidant enzymes, such as superoxide dismutase (SOD's), including different allotypes, and catalase were studied here. The cancer cell line used in this particular study, MB-231, has inherent low enzymatic catalase activity, and as a result, these cells express high levels of hydrogen peroxide ($H_2O_2$) than other cancer cells. In the present study, VnNs treatment gave rise to an initial reduction in ROS levels at 4 h of incubation, and it reversed its ROS levels after 24 h of treatment **Figure 5.28**. Both quantitative and qualitative results confirmed an initial decrease in DCF fluorescence intensity, which attributed to the intrinsic ROS quenching ability of VnNs pertaining to the growth of the material in the 001 plane. In another study, the 010 plane in vanadium nanowires were reported to exhibit halo-peroxidase activity (Golchin *et al.*, 2017), where the plane acted as a Lewis base capable of accepting oxygen atoms. However, in this study, the peak corresponding to 001 plane, stacked with neutral coordinative saturated vanadium cations are found responsible for the initial catalytic activity of ROS quenching in vanadium treated cancer cells. Moreover, an increase in ROS levels towards 24 h is attributed to the loss of catalytic activity at longer time points. Towards later stages, the treatment could have also activated the intrinsic cellular antioxidant machinery, which failed to elicit its properties by contributing to elevated ROS levels towards 24 h. It was surprising to note such an observation and pathway switch between the antioxidant pathway and oxidative stress. Further, a more specific ROS indicator, such as $H_2O_2$, was evaluated using an Amplex Red assay.

### 5.5.8. Detection of $H_2O_2$ using Amplex Red assay

In order to precisely monitor the levels of $H_2O_2$, rather than quantifying the total ROS as in DCF assay, further used an $H_2O_2$ specific dye, Amplex red. The dye conjugated to horseradish peroxidase undergo oxidation with $H_2O_2$ and give red fluorescence intensity, which clearly matched with the levels of $H_2O_2$ in treated cells. This method of oxidative stress measurement is considered as the most efficient and sensitive method which utilized whole cell lysate for the experiment (Kalyanaraman *et al.*, 2012). Spectroscopic quantification on the levels of $H_2O_2$ in VnNs treated cells marked an initial decline in the fluorescence pattern after 4 h, which is in par with the results from the DCF assay **Figure 5.30**. Hence, together with these two experiments on ROS detection, it revealed the probable chances on the influence of the nanomaterial exposure time and the extent of nanomaterial uptake into the cells at any given point of time are the deciding factors on imparting essential roles in executing changes in the cellular physiological activity. Cells spend most of their energy in maintaining a constant balance on the redox potential of cells by tightly regulating the mRNA levels of stress response genes. Hence, further, evaluated the levels of stress response mRNA in VnNs treated MB-231 cells.

### 5.5.9. Effect of VnNs treatment on stress response mRNA levels

Cells implement various mechanisms to cope up with any incurred stress by activating various stress response genes and proteins. Mitochondria is one of the most sensitive organelles which respond faster to these responses. Cellular ATP is produced as a result of electron transfer between different compartments through the mitochondrial intermembrane space. Damage to these mitochondrial membranes leads to the escape of electrons from the electron transport chain and produces highly reactive superoxide radicals. These radicals create damages to the various cellular organelles by altering the cell and organelle membrane. However, regular cellular activity is achieved through a strong interplay between oxidative stress and antioxidative defense system. These antioxidant mechanisms involve the activity of several enzymes like SOD1, SOD2, SOD3, catalase, etc. which are engaged in the conversion of highly reactive free radicals into $H_2O_2$. While, the homologous dismutase enzyme is classified according to their intracellular localization with SOD1 in the cytoplasm, SOD2 in the mitochondrial matrix, and SOD3 within the extracellular milieu. Catalase enzyme is produced by the peroxisomes and is involved in the process of conversion of $H_2O_2$ into the water and molecular oxygen. The relative level of mRNA of these SOD's and catalase was monitored as a measure of redox function in cells upon VnNs treatment.

The results of the study indicated low levels of all the three SOD mRNA with 50 uM VnNs treatment for an initial 4 h period **Figure 5.31**. These results, when compared with the DCF assay results, where we observed a drop in the ROS levels at 4h, possibly explained the impact of reactive surface groups in the nano vanadium, responsible for the reduction in ROS levels in treated cells. Moreover, the involvement of low levels of SOD mRNA could further support this finding. This observation points out that VnNs were able to neutralize basal levels of superoxide radicals as a result of immediate response to cells under treatment; further, the results were well correlated with the initial high levels of catalase mRNA. The observation indicated the efficacy of VnNs treated cells to trigger catalase mRNA production, which aid in the conversion of $H_2O_2$ to water. However, upon more extended incubation periods, various intrinsic cellular machinery gets activated in response to the high cellular uptake of VnNs. Further, a decrease in surface reactivity of VnNs would have accounted for decreased catalase mRNA levels towards 24 h and is reflected through the increased $H_2O_2$ levels in the cytosol resulting in membrane damage and subsequent activation of various stress response elements towards 24 h of the treatment period. These reactions also evoked a significant number of cell death in treated cells towards 24 and 48 h of treatment. Further, the study focussed on understanding the mode of cell death using various methods.

### 5.5.10. Apoptosis assay by Annexin-V-FITC / Propidium Iodide

Necrosis and apoptosis are the major classical cellular death pathways. Various markers are involved in classifying cells undergoing death via apoptosis and necrosis. Some of the key features that mark necrosis are the early stage loss of cell membrane integrity and an energy-independent progression of cells towards plasma membrane rupture and leakage of cellular components to its extracellular microenvironment thereby damaging the neighboring cells. While the process of apoptosis is marked in cells by the formation of characteristic membrane blebs and is an energy-dependent phenomenon that involves complex molecular signaling cascades with preserved membrane integrity even until later stages in the apoptotic process (Chen *et al.*, 2008). Apoptosis also includes a first event where the cell membrane integral protein phosphatidylserine, flip outside the membrane as the cells get destined to undergo apoptosis while still maintaining the intact plasma membrane (Denecker *et al.*, 2000). Hence, an assay based on the accessibility of this protein marked during apoptotic cell death is adopted for the study by making use of a highly specific protein, annexin-V conjugated to a fluorophore. Quantification was done using a flow cytometry study using annexin V/PI apoptotic kit and determined the distribution of death in cells following 24 h and 48 h of VnNs treatment. The MB-231 cells exposed to VnNs exhibited the unique positioning of cells towards late apoptotic stages within 24 h of treatment, and there was an insignificant number of early apoptotic cell populations towards 24 h treatment **Figure 5.32**. In addition, cells were stained PI-positive in the 24 h time point, which could be due to the loss of nuclear membrane integrity, which allowed most of the PI molecules to enter into the cells and stained cells PI-positive. Cells in the 48 h treatment showed the presence of both early and late apoptotic cells, which accounted for more than twice the population that was observed in the 24 h group. Hence, the study observed that, more than 50 % of the cells underwent death via apoptosis by the end of 48 h of VnNs treatment. In addition, a more apoptosis specific caspase molecules were identified with a based FRET experiment in the VnNs treated cells.

### 5.5.11. SCAT3 - NLS as an apoptotic Caspase-3 sensor

Caspases exist in their inactive form called as zymogens, which are kept under the strict control of various inhibitory molecules inside the cells. They are maintained under tight control and prevent any unnecessary activation of caspases until destined cells receive specific death queues (Riedl and Shi, 2004) and are often used as markers to determine the mechanism of cell death. MB-231 cells transfected with SCAT3 – NLS had amino acid sequences that were flagged in between the donor and acceptor molecules. The SACT signals were cleaved by activated caspases, which resulted in the loss of FRET activity, which was monitored using live-cell ratio imaging (Joseph *et al.*, 2011). The fluorescence images accounted for the extent of the real-time caspase 3/7 activation and thus pointed to the transient induction of apoptosis **Figure 5.33**. This technique is considered as highly caspase specific and is insensitive to any environmental queues. Damages to the mitochondrial membrane potential have an impact on caspase activation. Here, in this study, the cells expressed MMP activation and superoxide generation; the FRET-based assay also resulted in caspase activation, thereby indicated strong evidence towards the apoptotic mode of cell death. These studies reveal the co-existence of a variety of complex paths involving the interplay between various cellular pathways, which finally lead VnNs treatment towards the apoptotic way of cell death.

Apoptosis is also marked by changes in the cytoskeletal architecture, cell membrane morphology, and nuclear condensation pattern, hence further evaluated these factors, which accounted for an apoptotic mode of cell death.

### 5.5.12. Cytoskeletal architecture

Typically, cell morphology is maintained through the activity of a significant component in the cytoskeletal protein called actin, and they play essential roles in the intracellular movement of cellular organelles, protein trafficking, etc. Changes in its cytoskeletal architecture result in the reduction of cell viability; hence, morphological observation is considered as a simple, more dependable display of cellular cytotoxicity. A cytoskeletal retraction was observed due to actin filament reorganization and resulted in altered cellular morphology when detected using Rhodamine phalloidin **Figure 5.34**. It could be one of the possible mechanisms behind mitochondrial clumping, as seen with the JC-10 experiment, which requires actin reorganization (Boldogh and Pon, 2006). Cellular extensions are essential for maintaining cell adhesion within cells and also with the cell culture substratum (Pellegrin and Mellor, 2007). In this study, the cytoskeletal retraction could be a possible reason behind the potential action of VnNs and also account for the decrease in cell viability in the 48 h MTT experiment.

### 5.5.13. Membrane morphology through SEM

Characteristic membrane blebs mark morphology alterations during the onset of apoptotic events (Coleman *et al.*, 2001). The primary function of these blebs is to eliminate the damaged organelles by compartmentalizing the whole cellular components within various membrane-bound vesicles with a portion of the cytoplasm, and they get extruded out or pinched out of the cell membrane **Figure 5.36**. This kind of cell death does not cause damage to the nearby cells and hence acts as an efficient mode of cell destruction in generating newer cancer therapeutics. The scanning electron micrographs showed clear and smooth cell surface on the untreated cell population while the cell surface of VnNs treated cells established membrane blebs, which indicated the process of active apoptosis in these cells.

### 5.5.14. DNA condensation pattern and nuclear fragmentation

Various inter-nucleosome enzymes are involved in the cleavage of DNA, DNA condensation and break down, as a late event in the apoptotic process. In the current study, VnNs treatment evoked cellular death mechanism via apoptosis, and DNA breakdown, a characteristic to the process. Chromatin condensation, DNA fragmentation, and a reduction in nuclear size are characteristics of the apoptotic cell death pathway (Susin *et al.*, 2000). The 48 h VnNs treated population had an increased number of cells showing DNA fragmentation pattern, as evident from the electron micrographs **Figure 5.37** and fluorescent microscopy images **Figure 5.38**, which supported the mechanism of apoptosis induction. They also showed very less distribution of cellular organelles, distorted nuclear membrane integrity, and broken down chromatin, which indicated apoptosis mediated cell death.

### 5.5.15. *In vitro* cell migration assay

Cancer cell metastasis is a significant setback in cancer management (Yokota, 2000). Hence, the ability of VnNs to inhibit *in vitro* cell migration was checked using MDA-MB-231 breast cancer cells through a wound-healing experiment on a confluent monolayer of cells. The result exhibited great success, and the wound created was found to be persistent even after 72 h of nanomaterial treatment, clearly indicating the efficiency of VnNs to inhibit cancer cell migration **Figure 5.39**. This result demonstrates the probability of VnNs to be developed as an effective blocker for cancer cell metastasis and as a cancer management modality for inhibiting cancer cell multiplication *in vitro* for future applications.

Regression of tumor formation is also a significant task when we think about cancer management. Further, the ability of VnNs to inhibit cancer cell clone formation was studied using a clonogenic assay.

### 5.5.16. Colony formation assay

A single cancer cell has the ability to generate a colony of more than 50 cells. This indicates the tumor formation ability of the fraction of cells that survived the treatment from cytotoxic drug molecules or ionizing radiations (Franken *et al.*, 2006). The reproductive viability of cancer cells after treatment with VnNs, monitored through a clonogenic test, revealed a significant reduction in the ability of cells to multiply after VnNs treatment **Figure 5.40**. The analysis is done in comparison with the untreated control cell population. The experiment indicated that the 50 & 100 µM VnNs treatment-induced irreversible cellular damage, inhibited cell survival, and cell proliferation. Thus, the VnNs treatment hindered colony formation, and the assay showed the effectiveness of VnNs to be further developed as an anti-tumor agent for future applications.

## 5.6. VnNs interaction studies with *Swiss albino* mice

*In vivo* interactions of VnNs were studied using healthy Swiss albino mice to gain an idea on the effect of nano vanadium on normal mice. The test and control groups of animals followed experiments and evaluated the biodistribution of vanadium in vital organs involved in the metabolism and excretion of VnNs particles and also evaluated any significant profile of toxicities.

### 5.6.1. The acute response towards VnNs administration

VnNs followed intravenous administration in female *Swiss albino* mice were monitored for acute (immediate) response in this part of the study. The pharmacological dose of administration, route of administration, and bioavailability of the nanoparticle determine its fate and also the actual effect it does to the biological system (Born *et al.*, 2003). The treatment of administration was chosen to be 1 mg/kg body mass of the animal, which was ten times lower than the value, that was generally used for the toxicity studies. The experimental animals were exposed to a single dose of intravenous (*i.v.*) administration of VnNs and were observed to study various parameters like nanoparticle persistence, organ distribution, excretion, and clinical signs of toxicity. None of the animals under treatment exhibited any clinical signs of illness, stress response, or any other symptoms like motor reflexes, respiratory, cardiovascular distress, salivation, or any gastrointestinal responses throughout the experimental phase. No adverse reactions or death due to toxic insult were observed during the trial period.

### 5.6.2. Body weights of experimental animals

Any change in the bodyweight of animals is considered as an indirect indication of the effect of nanoparticle exposure. Generally, nanoparticles exhibit organ-specific accumulation and interfere with the physiological activities of the test animals and are reflected as secondary indications of nanomaterial treatment (Yildirimer *et al.*, 2011). In the present study, there were no observable changes in body weight or standard deviations in the overall weight profiles of animals following a single dose of intravenous injection in any of the treatment groups monitored under the investigation period.

### 5.6.3. Study on urine analysis

Retention and removal of VnNs from the animal body were evaluated by detecting its presence in the urine samples via Raman spectroscopy. Intravenously administered nanoparticles get access to various organs by traveling through the bloodstream. They mainly accumulated in multiple organs such as the liver, spleen, and kidney as they are involved in the process of elimination of foreign materials from the body. The urine analysis at different time points of the study indicated the persistence of VnNs in the blood and an idea regarding the time point of nanomaterial elimination **Figure 5.41.**

Raman peak at 1006 $cm^{-1}$ in the pre-treatment urine samples exhibited the unique C-N stretching in urea. The post-treatment urine samples were considered at various time points after injection. Further checked for the Raman signals at 995 $cm^{-1}$, which corresponded to the metal-oxygen vibrations in VnNs in the post vanadium injected urine samples starting from 1 h. The resultant spectra showed a peak shift in V-O stretch from 995 to 944 $cm^{-1}$. And these results go in par with the previous report (Keuleers *et al.*, 1999) on nanomaterial conjugation with the urea molecules. The shift in peak position is possibly attributed to the interaction between VnNs and urea with a gradual increase in peak intensity until 72 h with a continuing decrease in the urea peak. However, post three days, the urea peak regained its position and indicated a very weak V-O peak at 72 h. However, by day 21 of post-exposure, there was no presence of vanadium in the urine, which gave an idea about the mechanism of clearance in VnNs. It could be possible that the nanomaterial would have accumulated in some of the organs, making them difficult for detection in the urine analysis via Raman spectroscopy in the later time points.

### 5.6.4. Blood studies for hematology and biochemistry parameters

Whole blood analysis for hematology parameters like blood cell volume, hemoglobin, count of total blood cells, and platelets indicated a standard range of values in the treatment group at all the time points and was comparable with that of untreated control animal blood reports. An increased WBC count was observed with the 21-day post-exposure sample, which indicated immune activation, which could be explained as a result of delayed response towards the nanomaterial treatment. However, other blood parameters were in the normal range and denoted no adverse toxic effects (**Table 4.1**), and the treatment did not induce any acute immune activation in the nanomaterial treated experimental animals.

The biochemistry measures obtained from the serum samples like creatinine and urea were found to be comparable with that of the untreated control animal samples. These two enzymes gave an indication regarding the efficacy of renal function and the health of kidneys. Any damage to these organs results in the elevated levels of these enzymes (Assem and Levy, 2009). In the current study, the levels of serum urea and creatinine, even in the 21-day post-exposure group, maintained a normal range and were comparable with that of the saline-injected control values.

The physiological health condition of the liver is generally indicated through the levels of liver enzymes named alanine aminotransferase (ALT) & aspartate aminotransferase (AST) in the blood. High serum levels of ALT and AST indicate loss of cellular integrity, indicating hepatic toxicity. The present study demonstrates that the enzyme levels were consistent throughout the experimental period and was comparable with that of the UT control values **Table 4.2**. The importance of these enzymes in the assessment of hepatic toxicity is well established (Yang *et al.*, 2014).

In addition, the levels of blood cholesterol indicated a significant decline in the value indicating the efficacy of VnNs to reduce the cholesterol levels towards the endpoint of the study. Pillai *et al.* also reported the effectiveness of vanadium to act as a cholesterol-reducing agent (Pillai, Subramanian and Kandaswamy, 2014). Overall, the blood parameter study indicated no observable changes with the hematology or biochemistry parameters in animals exposed to 1 mg/kg of VnNs in comparison with the saline-injected control group.

### 5.6.5. Effect of VnNs on the size and gross weight of internal organs

Gross observation for the size of various internal organs involved in the metabolism and excretion of foreign material indicated the probable chances of organ degeneration, hypertrophy, or edema (Yang *et al.*, 2017). However, in this work, there were no significant observable changes in organ weights within a single group or between the experimental animal groups when compared to that of the saline-injected control group indicating that the nanomaterial hasn’t caused any severe damage of atrophy to any of the internal organs within in the experimental animals.

### 5.6.6. Bio-distribution of VnNs through ICP analysis

A systematic study on Absorption, Distribution, Metabolism, Excretion, and Toxicity (ADME Tox) is essential to understand nanomaterial interaction with the biological system. Absorption involves the transfer of molecules into the systemic circulation where the dose and route of administration determine its bioavailability and biodistribution parameters. Nanomaterials, as same as the case of any other material once introduced into the bloodstream, get translocated into various organs along with the blood, denote the distribution part, and subsequently, they get accumulated into various organs (Exbrayat, Moudilou and Lapied, 2015). Bioavailability is the quantity of material reaching the designated organ, and its fate is determined by its persistence and metabolism there. In the current study, where a single shot tail vein injection strategy is adopted, all the injected VnNs enter into the bloodstream and get immediately translocated into various organs. Interestingly the ICP analysis showed a very less quantity of the nanomaterial accumulation towards the initial 1-day post-injection with liver, spleen, and kidney samples. While the 21-day post-injection liver denoted significant levels of vanadium followed by spleen and kidneys **Figure 4.42**. This observation indicated that the nanomaterial preferred to persist in the circulation rather than getting accumulated immediately after the injection, and a regular pattern of accumulation in the liver was observed post-1-day injection. The liver is the critical organ involved in the internal metabolic process, and it doesn't interfere with the metabolism of inert and unmodified nanomaterials. Persistence of VnNs in the liver samples indicated long circulation life and also didn't cause any damage to the metabolic profile of hepatic cellular system as displayed through the biochemistry parameters like ALP and AST. Metabolism is involved in the biotransformation of a toxic form of material into a less toxic, more water-soluble, and easily execrable form, which mainly involves liver enzymes. Dose/concentration, duration of exposure, and the persistence of the material in a biological system determine the toxicity of the compound. The kidney samples didn't display significant levels of nanomaterial persistence even towards later time points, indicating fewer damages to kidneys as they are involved in the excretion of foreign materials. Spleen also denotes very less accumulation of VnNs towards 21day post-injection, which could also result in immune activation and could be responsible for the increased WBC levels displayed through the blood analysis. Overall these studies suggested that VnNs are persistent in the blood and later showed long term persistence and accumulation in the liver after 21 days of post-exposure.

### 5.6.7. VnNs influence on levels of stress response mRNA

Transcription is the process of mRNA synthesis in cells, which later undergo translation and obtain the final effector protein molecules. Any altered transcription and expression of specific mRNA at a particular time point in a biological system advertises information on the environmental condition through which the cell proceeds. Antioxidants are enzymes that protect the cells from ROS, trigger oxidative damage, and also help cells to maintain their redox pathway. The primary antioxidant enzymes studied are SOD's, and catalase. The SOD's convert superoxide radicals into $H_2O_2$, and molecular oxygen and catalase further convert $H_2O_2$ into less reactive water molecules (Fatahian-Dehkordi *et al.*, 2017). The current study observed initial low levels of mRNA followed by a hike at post-3-day exposure and after that, a decline towards 21 days post-exposure with SOD1,2,3 and catalase in the liver sample suggested that the nanomaterial accumulation towards later time points might be responsible for such a delayed response in the liver sample which is evident from the ICP observations too. While the kidney samples elicited an initial hike in the mRNA levels, which was shown subsided on day 3 and day 21 samples **Figure 4.44**. This observation could be correlated with the Raman analysis on urine samples which indicated vanadium elimination through the urine from the initial hours of i.v injection till 3-day post-exposure which indicated efficient VnNs elimination through the kidneys, and also the ICP results correlate that very less quantity of vanadium remained in the kidney samples at all the time points under the study. Even though in kidney samples, an initial increase in the SOD mRNAs was observed, the process was also dealt with enormous catalase involved in detoxifying any $H_2O_2$ produced during the initial days of post-treatment. Similar observations were also made with the spleen, indicating an initial hike in mRNA levels, which subside at later time points indicating efficient nanomaterial clearance, and also proved that VnNs don't induce any oxidative damage to the splenic cells. Hence, the present study indicated that a single dose exposure of VnNs did not alter the oxidative balance in the liver, kidney, and spleen of the treated mice.

### 5.6.8. Enzymatic assay for superoxides

The mRNA produced in cells is translated into proteins, specifically enzymes that catalyze explicit reactions. Here the protein levels of SOD also depicted similar results in comparison with the mRNA levels. A significant increase in the total enzymatic activity of SOD was observed only with the 3-day post-injection liver sample and a 1day post-injection kidney sample. This observation goes well in hand with the mRNA levels and ICP results, which indicated the retention of vanadium in the 3rd-day post i.v liver and 1-day post *i.v* kidney samples. However, the 1day and 21day post injected liver samples didn't show a significant increase in the SOD levels attributed to the less prevalence of VnNs. The hike in SOD activity in the 1-day post-injection kidney samples indicated efficient redox activity and elimination occurring at this time point, which significantly reduced the SOD activity in the post 3rd day, indicated efficient removal of nanoparticles **Figure 4.46**. The spleen also denoted very less superoxide activity, which could be attributed to the low accumulation of the nanoparticles.

The overall impression of this assay is that the VnNs induced a transient increase in ROS levels and which is reflected from the slight increase in SOD levels in various organs towards the initial period of VnNs administration. The enzyme levels gradually subsided towards later points of the study, which could be attributed to the nanomaterial clearance mechanism or due to the prevalence of various redox machinery operating within the *in vivo* conditions.

### 5.6.9. Histopathology analysis

Internal organs such as the liver, spleen, and kidney of the animals from the treatment group were observed for histology examinations in comparison with the control group of animals. It was evident from the histology findings of liver tissue that VnNs treatment elicits moderate levels of pathological changes after immediate administration of the material, which regained normal morphology towards the end of the study period. However, the blood parameter analysis showed no deviations in the

AST and ALT values between treated and untreated groups. The histology of the kidney was also found to be typical with a clear distinction between the cortex and medullary regions with well-defined Bowman's capsule and collecting ducts. These observations go in hand with the blood parameters indicated comparable urea and creatinine levels. The spleen histology also showed cellular architectural deformities at an initial period, which regained its characteristic cellular architecture towards day 21 of post-injection, which meant a morphology comparable to that of the control group with clear red and white pulp regions **Figure 4.47**. These results were compared with the increase in WBC count, which acted as an indicator of immune activation because of delayed response towards the VnNs treatment. In general, the study gave an overall idea of various histological modifications that occurred in multiple organs at different time points of the study.

# CHAPTER - 6

# 6 SUMMARY & CONCLUSIONS

Nanoparticles elicit drastic changes in their physicochemical properties pertaining to their charge, size, shape, oxidation state, and the crystal structure, which makes them stand different from their bulk material counterparts. The beauty regarding nanomaterials is that any particles can be synthesized within the range of nanometres with fascinating properties that account for their increased surface area and exceptional physicochemical properties. Numerous studies have come up emphasizing the nanomaterial effect on each of these parameters in the biological system. There are excellent previous reports which describe various applications of vanadium-based nanosystems depending on their specific morphology and oxidation states. Such a report describes the biological significance of shape-dependent antioxidant property of nanowires where they exhibited haloperoxidase like activity. Nanoparticles with inherent enzyme-like activity make them find applications as low-cost catalysts with excellent stability. Research encompassing understanding the underlying biological response towards engineered nanoparticles is of all time interest due to its full acceptance and versatile possibilities in the application. Such an understanding will significantly foster our ability to engineer a newer generation of potential nanoformulations with specific indented end-use. For the successful development of such formulations, the focus of studies must change from proof-of-concept to detailed basic studies.  Hence, there is an urgent need to look into various aspects of the biological interaction of engineered nanomaterials due to the rapid development of nanotechnology and increased use of NPs and NP-based formulations.

Considering the drastic advances and versatile applications of nanomaterials, nano vanadium is under the spotlight considering the previous reports on the use of vanadium compounds in cancer management. The study of this thesis utilized nanovanadium pentoxide application in the triple-negative breast cancer cell model, and this chapter summarises the overall findings and significant highlights of the study. The study optimized a method of synthesis of two different shapes of nano vanadium.

The nanoparticle synthesis adopted an easy to perform hydrothermal method with vanadium oxychloride and benzoyl alcohol following calcination. The intermediate material subjected to detailed thermal analysis revealed a 50 % weight loss at 350 °C that contributed to the loss of residual reactants, and around 25 % of the mass remained after 367 °C, which indicated thermal stability and high sample purity at this temperature. The DTA curve between 300-700 °C showed an exotherm at 375 °C and an endotherm at around 570 °C, which attributed to the crystallization and melting of vanadium pentoxide, respectively. The materials resulted were thoroughly characterized for their size, shape, sample purity, oxidation state, and surface charge. The morphology analysis of the sample calcined at 367 °C showed spherical morphology (VnNs), and 570 °C showed plate-like morphology (VnNp) when observed through a Transmission electron microscope. The HR-TEM proved VnNs to have an average 50 nm size, and each plate of VnNp had 1 nm thickness and several micrometers in length. The selected area diffraction (SAED) pattern of samples demonstrated a highly crystalline nature corresponding to respective VnNs and VnNp. Further, the EDX analysis showed that the sample contained only vanadium and oxygen. The XRD analysis also confirmed the pattern of nano vanadium pentoxide to have an orthorhombic, sherrebanite crystal structure corresponding to the PDF 00-041-1426 value of $V_2O_5$. The unique metal-oxygen bond stretching and bending vibrations in both the Vn samples clearly observed through the FT-IR analysis. The spectroscopy showed peaks at 1014, 840, and 675 $cm^{-1}$, which corresponded to the V=O stretching, O–V vibrations, and asymmetric and symmetric stretching modes in V–O–V bridging respectively. The Raman spectral analysis further explained the metal-oxygen bonding structure with peaks at 281 & 403 $cm^{-1}$, corresponding to the bending vibration of O–V=O. Besides, the stretching vibrations at 687 $cm^{-1}$ and 992 $cm^{-1}$ denoted doubly coordinated oxygen in V=O and the terminal unshared oxygen atom in V–O, respectively. However, slight variations in the peak positions between the two samples were observed, which is attributed to the traces of β forms of $V_2O_5$ along with the α forms. The surface charge of VnNs was found to be -13 MeV and -21 MeV for VnNs and VnNp, respectively.

Following the physicochemical characterization, initial cytotoxicity studies were conducted for optimizing the concentration of Vn materials using an MTT assay. The study used immortalized triple-negative breast cancer MDA-MB-231 cell lines and normal mouse fibroblast cell line L929. More than 70 % of the L929 cells treated with VnNs for 24 and 48 h were viable at all the treatment concentrations, while VnNp treatment resulted in massive cell death in L929 cells. VnNs treatment on MB-231 cells showed a dose-dependent effect on cell viability. At 50µM VnNs treatment, a statistically significant 50 % reduction in cell viability was observed towards 24 h, which further reduced towards 48 h in MB-231 cells. However, MB - 231 cells treated with VnNp showed a dose-independent massive decline in cell viability towards 24 and 48 h.

Based on these results, further studies were divided into two, which covers the study on exploring the antimicrobial interactions of VnNs and VnNp on representative G+ and G- bacterial populations. 50µM and lower concentrations of VnNs were used to evaluate its molecular mechanism of action in MB-231 breast cancer cells and *in vivo* models.

The bacterial interaction studies were initiated with an experiment to find the MIC of the VnNp that inhibits the growth of the 50 % bacteria in the culture system. The MIC of VnNp was found to be 0.613 mM for *E. coli* and 0.856 mM for *S. aureus*. And VnNs elicited 0.654 mM on *E. coli* and 0.937 mM for *S. aureus* in liquid broth cultures. This clearly indicated that a comparatively lower concentration (0.613 mM) of VnNp was enough to cause significant cell death in *E. coli* when compared to *S. aureus*. In order to see whether the antibacterial activity is elicited through cell membrane damage, the respective VnNs and VnNp treated bacterial cells were observed under a field-emission scanning electron microscope. The electron microscopy revealed remarkable membrane alterations in *E. coli* samples treated with VnNp, which is attributed to the physical damage induced with its sharp edges. While the VnNp treated *S. aureus,* bacterial cells didn’t show cell membrane damage, but bacterial clumps entrapped VnNp within them. Whereas, VnNs neither caused any membrane disruptions in *S. aureus* or *E. coli* nor could they pierce these microbial membranes, attributed to their characteristic spherical morphology.

The EM results were further validated to have an understanding of whether Vn induced any changes in the structural components of the bacteria through Raman spectral mapping on Vn treated bacterial cells. The Raman spectra from the bacteria denoted specific band modifications in the peak positions and peak intensity with VnNp treatment in comparison with the untreated bacterial population. Irrespective of the VnNp treatment concentration, *E. coli* bacteria resulted in a drastic decline in the Raman peak intensity at 1095 $cm^{-1}$, which corresponds to the vibration of the DNA phosphate backbone. This could be attributed to the direct or indirect effect of VnNp interaction with the bacterial components, which resulted in damaging the DNA backbone structure. While Raman spectra from VnNp treated *S. aureus*, didn't show alterations in the bacterial spectra at a lower concentration, but 1mM VnNp treated samples showed two additional peaks at 697 and 993 $cm^{-1}$ which indicated the presence of entrapped vanadium within the bacterial clumps. Unlike *E. coli*, the *S. aureus* didn't show an evident DNA phosphate peak at 1095 $cm^{-1}$, which could be due to the presence of a thick peptidoglycan layer in these bacteria. This thick layer renders *S. aureus* more resistant towards physical damages and could be the reason for bacterial clump formation and vanadium entrapment. In addition, the Raman spectra of VnNs treated *S. aureus* did not show any visible changes in the overall spectral pattern, which is again attributed to the presence of a thick peptidoglycan layer. These results indicated high susceptibility of *E. coli* cells towards VnNp treatment; this study also revealed a statistically significant increase in the levels of ROS in *E. coli* biofilms, thus proving the efficiency of VnNp as a potent antibacterial agent against G(-), *E. coli* bacteria.

The subsequent section of the thesis dealt with studies on understanding the *in vitro* biological interactions of VnNs and VnNp on MDA-MB-231 and L929 cells. The MTT assay revealed a 50 % reduction in cell viability upon treatment with 50 μM VnNs on MDA-MB-231 cells for 24 h, while L929 cells were viable at all the tested concentrations. The results indicated that VnNs exhibited a concentration-dependent modulation of cell viability in cancer cells while they did not cause such dependency in a standard fibroblast cell line. Based on the preliminary MTT studies, further experiments used 50 μM and lower concentrations of VnNs for detailed investigations on the cellular organelles, stress response, and cell death in MB-231 cells upon nanomaterial internalization. The study gave special attention to understand its biological effects on efficient nanomaterial uptake by the treated cells. Proved the cellular uptake of VnNs via techniques like side scatter pattern analysis through flow cytometry, Raman spectral mapping, and TEM. The flow cytometry data showed distinct shifts in SSC and FSC patterns proving efficient VnNs uptake by MDA-MB-231 breast cancer cells in comparison with the standard L929 fibroblast cell line. The Raman spectral mapping on VnNs treated cells also proved efficient Vn internalization with a prominent peak at 996 $cm^{-1}$ corresponding to the stable vanadium oxygen double bond, with 50 μM treatment. The weak optical property of the material hindered the use of optical microscopy in tracking the VnNs inside the cells. Therefore, in this study, EM has been used extensively to prove the cellular uptake by direct visualization of intracellular localization of VnNs. A closer look with TEM clearly revealed efficient nanomaterial uptake with 50 μM treatment for 4 h, and subsequent changes took place within MDA-MB-231 cells upon nanosphere treatment. Here, the flow cytometry results were again confirmed with electron microscopy, which demonstrated efficient VnNs uptake by the cells. In addition, TEM enabled us to have a clear idea of the positioning of nanomaterials inside the cells, which also revealed specific cellular structures corresponding to autophagy induction. In addition, we observed that lysosomes also play a pivotal role in maintaining the cellular process of autophagy. The study proved altered autophagy balance with prominent induction of autophagy marker protein, LC3, through western blot analysis on a flux assay. The analysis indicated a 2 fold increase in the levels of LC3 II proteins upon 4h VnNs treatment, which further elevated its levels in the presence of chloroquine. This observation was further validated by analyzing the degree of autophagosome formation in cells expressing GFP-LC3. The results noted a significant increase in autophagy induction through the formation of GFP-LC3 punctuates. The process of autophagy, also affected mitochondrial health, as evident from the results of MMP indicators such as TMRM and JC-10. Which, clearly revealed a simultaneous loss of mitochondrial membrane potential along with GFP-LC3 induction. Fluorescent microscopy and flow cytometry showed an increased number of cells with lost mitochondrial membrane potential. The EM studies also revealed specific accumulation of VnNs within these mitochondria, which could be a reason for the impaired mitochondrial membrane activity or the impaired mitochondrial membrane activity could be a reason for the VnNs uptake. Autophagy is a process of clearing the damaged cellular organelles, by entrapping them within autophagosomes and digesting in the lysosomes. In this study, an important notable observation was that VnNs accumulated inside the lysosomes with enhanced acidification, increased lysosomal number, and lysosomal size due to active lysosomal fusion with the autophagosomes without any lysosomal membrane disruption even after prolonged incubation time points. The lysosomes maintained excellent membrane integrity even after 48 h of VnNs treatment, as proved with lysotracker red and acridine orange. The lysosomal membrane integrity act as a pivot, which determines the mode of cell death to proceed towards necrosis or apoptosis. However, the VnNs treatment maintained a significant level of lysosomal membrane integrity and prevented cellular necrosis. Apart from autophagy induction and altered mitochondrial membrane potential, the VnNs treated cells experienced altered mitochondrial respiratory chain function. This involved oxidative stress-mediated signaling events operating simultaneously and or vice versa. Increased oxidative stress led to transitional pore formation in the mitochondrial membrane, which further resulted in distorted membrane integrity, enhanced VnNs uptake into mitochondria, as evident from the TEM micrographs and ROS generation. The levels of ROS produced in cells subsequent to 4 h VnNs treatment through DCF assay showed a decline in the initial cellular ROS levels, these results correlated well with the cell-free experiment on the inhibition of pyrogallol auto-oxidation. This level of ROS quenching in MB-231 cells is attributed to the intrinsic ROS quenching activity of the 001 crystal plane in VnNs. Whereas 24 h VnNs treatment showed elevated ROS levels, which is due to the loss of catalytic activity in VnNs pertaining to active site saturation towards later stages. It was amazing to note such a dramatic switch between pathways having an initial antioxidant activity, resultant decreased cellular ROS towards 4 h treatment, and later oxidative stress induction portrayed by increased ROS towards 24 h of VnNs treatment. Similarly, the $H_2O_2$ profile in cells after treatment with VnNs also exhibited a robust $H_2O_2$ quenching activity during the first hours of treatment, and the phenomenon gradually reversed upon longer VnNs incubation time points. These experiments indicated the potential of VnNs to act in conjugation with the cellular antioxidant enzymes to modulate the cellular stress response machinery.

Further, changes in the transcriptional level of genes associated with cellular oxidative stress helped us to understand the subtle differences in the mRNA levels of VnNs treated cells at different time points. An initial low level of superoxide dismutase stress response mRNA, such as the SOD1, SOD2, and SOD3, was later increased towards 24 h. These initial low levels of SOD mRNA were complemented with enormous catalase in the first hours, which was later declined and accounted for the high SOD activity towards 24 h. These responses propelled the cells, further towards the onset of other stress response reactions such as cell cycle arrest. VnNs treatment also resulted in a pronounced increase in the number of cells with G2/M phase cell cycle arrest. The induction of cell cycle arrest was attributed to various reasons such as loss of mitochondrial membrane potential, respiratory chain dysfunction, ROS generation, increased acidic vesicle burden in cells. Despite the involvement of protective autophagy with suboptimal concentrations of VnNs, the treatment-induced apoptosis in cells via intracellular organelle damage by generating reactive oxygen species. Further, prolonged treatment with VnNs induced apoptosis detected through a highly specific dye Annexin-V,  proved a significant increase in cell number, decisive for apoptosis towards 48 h of VnNs treatment. VnNs treatment also resulted in nuclear membrane disruption, chromatin condensation, and lead cells to the apoptotic mode of cell death towards 48 h of treatment. Consistent with this, a FRET-based caspase sensor confirmed the activation of caspase 3/7 in VnNs treated cells, which further confirmed the apoptotic mode of cell death. The colony formation assay and cell migration assay further confirmed its potential to inhibit tumor clone formation and cell migration, which are thought to be critical towards metastatic cancer management.

The results on the preliminary efficacy studies, including stress response, biodistribution, and organ toxicity of VnNs on healthy swiss albino mice, indicated no signs of systemic or organ toxicity in the liver, spleen, and kidney. The study evaluated various blood parameters, vanadium accumulation, elimination, and biodistribution in the spleen, liver, and kidney of mice injected with VnNs. Urine analysis for VnNs elimination was studied with a confocal Raman spectroscopy, which revealed efficient excretion through urine by day 3 of post-injection. This observation indicated the efficacy of initial phase VnNs metabolism in the kidney. Even though there was an initial increase in the stress response mRNA levels of specified antioxidants in the liver, spleen, and kidney post-VnNs injection, the mRNA levels came down by post-21-day. Histopathology observation further revealed the pathological changes in the tissue sections from various organs, which also indicated the normal tissue architecture in these organs. These results accounted for the hepatic and renal safety aspects of VnNs exposure in animal models. These results need further validation in cancer animal models. All these observations point towards the fact that VnNs could be an exciting candidate for developing future cancer therapeutics.

Overall, the major conclusions that are drawn from the current study on the effects of vanadium nanoparticles on various cellular pathways and ultrastructural details of the molecular mechanism-taking place in mammalian, microbial, and animal models. The study provides a precise mechanistic understanding of the molecular interactions of nano vanadium pentoxide *in vitro* and *in vivo*.

- ✓ A detailed description of the technique adopted for the synthesis of two different morphologies of vanadium pentoxide nanoparticles is given in this work.
- ✓ Thorough characterization of the nanomaterials revealed the Physico-chemical properties of VnNs and VnNp matching with the previous reports on vanadium pentoxide.
- ✓ Morphology analysis revealed the spherical and plate-like morphology of the nanoparticles. XRD pattern correlated well with the JCPS values corresponding to the orthorhombic vanadium pentoxide structure. XPS and EDX showed high sample purity. FT-IR and Raman analysis proved the metal-oxygen bonds between atoms in the nanoparticles, which were also in par with

the previously reported values.

- ✓ A comparison of the antimicrobial activity of VnNs and VnNp on representative gram-positive and gram-negative bacteria revealed VnNp more effective against *E. coli* bacteria when compared with *S. aureus*. And VnNs showed similar antimicrobial activity with the two microorganisms. This finding agrees to the fact that nanoparticles with sharp edges show more toxicity than spherical ones.

- ✓ *In vitro,* studies on the biological interaction with mammalian cell lines revealed a dose-dependent cytotoxic behavior of the VnNs on triple-negative breast cancer cells, while VnNp treatment didn't alter the cell viability in L929 normal fibroblast cell lines. Detailed studies proved cellular uptake and established various events that occurred in VnNs treated cells such as initial autophagy response, mitochondrial and lysosomal damage, cell cycle arrest, nuclear double membrane disintegration, DNA damage, and apoptosis as the mechanism of action behind the cytotoxic profile of VnNs.

- ✓ *In vivo* interactions of VnNs on swiss albino mice showed excellent clearance mechanism via kidney without serious side effects or organ toxicity.

- ✓ Hence, we can say that VnNs could be further modified, dose optimized and fine-tuned to be developed for cancer management for the future.

# REFERENCES

André, R. *et al.* (2011) 'V2O5 Nanowires with an Intrinsic Peroxidase-Like Activity', *Advanced Functional Materials*, 21(3), pp. 501–509. doi: 10.1002/adfm.201001302.

Ansari, C. *et al.* (2014) 'Development of novel tumor-targeted theranostic nanoparticles activated by membrane-type matrix metalloproteinases for combined cancer magnetic resonance imaging and therapy', *Small*, 10(3), pp. 566–575. doi: 10.1002/smll.201301456.

Assem, F. L. and Levy, L. S. (2009) 'A Review of Current Toxicological Concerns on Vanadium Pentoxide and Other Vanadium Compounds: Gaps in Knowledge and Directions for Future Research', *Journal of Toxicology and Environmental Health, Part B*, 12(4), pp. 289–306. doi: 10.1080/10937400903094166.

Badmaev, V., Prakash, S. and Majeed, M. (1999) 'Vanadium: A Review of its Potential Role in the Fight Against Diabetes', *The Journal of Alternative and Complementary Medicine*, 5(3), pp. 273–291. doi: 10.1089/acm.1999.5.273.

Bao, G., Mitragotri, S. and Tong, S. (2013) 'Multifunctional Nanoparticles for Drug Delivery and Molecular Imaging', *Annual Review of Biomedical Engineering*, 15(1), pp. 253–282. doi: 10.1146/annurev-bioeng-071812-152409.

Barth, S., Glick, D. and Macleod, K. F. (2010) 'Autophagy: assays and artifacts', *The Journal of Pathology*, 221(2), pp. 117–124. doi: 10.1002/path.2694.

Beeran, A. E. *et al.* (2015) 'Multifunctional nano manganese ferrite ferrofluid for efficient theranostic application', *Colloids and Surfaces B: Biointerfaces*. Elsevier B.V., 136, pp. 1089–1097. doi: 10.1016/j.colsurfb.2015.11.010.

Biette, L. *et al.* (2005) 'Macroscopic Fibers of Oriented Vanadium Oxide Ribbons and Their Application as Highly Sensitive Alcohol Microsensors', *Advanced Materials*, 17(24), pp. 2970–2974. doi: 10.1002/adma.200501368.

Bishayee, A. *et al.* (2010) 'Vanadium in the detection, prevention and treatment of cancer: The in vivo evidence', *Cancer Letters*. Elsevier Ireland Ltd, 294(1), pp. 1–12. doi: 10.1016/j.canlet.2010.01.030.

Boldogh, I. R. and Pon, L. A. (2006) 'Interactions of mitochondria with the actin cytoskeleton', *Biochimica et Biophysica Acta (BBA) - Molecular Cell Research*, 1763(5–6), pp. 450–462. doi: 10.1016/j.bbamcr.2006.02.014.

Booth, F. W., Laye, M. J. and Spangenburg, E. E. (2010) 'Gold standards for scientists who are conducting animal-based exercise studies', *Journal of Applied Physiology*. doi: 10.1152/japplphysiol.00125.2009.

Born, S. L. *et al.* (2003) 'Comparative metabolism and kinetics of coumarin in mice and rats', *Food and Chemical Toxicology*. doi: 10.1016/S0278-6915(02)00227

Buglyo, P. *et al.* (2005) 'Aqueous Chemistry of the Vanadium III (V III ) and the V III −Dipicolinate Systems and a Comparison of the Effect of Three Oxidation States of Vanadium Compounds on Diabetic Hyperglycemia in Rats', *Inorganic Chemistry*, 44(15), pp. 5416–5427. doi: 10.1021/ic048331q.

Byrne, A. R. and Kosta, L. (1978) 'Vanadium in foods and in human body fluids and tissues', *Science of The Total Environment*, 10(1), pp. 17–30. doi: 10.1016/0048-9697(78)90046-3.

Cao, A. *et al.* (2005) 'Self-Assembled Vanadium Pentoxide (V2O5) Hollow Microspheres from Nanorods and Their Application in Lithium-Ion Batteries', *Angewandte Chemie International Edition*, 44(28), pp. 4391–4395. doi: 10.1002/anie.200500946.

Chan, C. K. *et al.* (2007) 'Fast, Completely Reversible Li Insertion in Vanadium Pentoxide Nanoribbons', *Nano Letters*, 7(2), pp. 490–495. doi: 10.1021/nl062883j.

Chen, F. *et al.* (1999) 'Vanadate induction of NF-κB involves IκB kinase β and SAPK/ERK kinase 1 in macrophages', *Journal of Biological Chemistry*. doi: 10.1074/jbc.274.29.20307.

Chen, Y. *et al.* (2008) 'Oxidative stress induces autophagic cell death independent of apoptosis in transformed and cancer cells', *Cell Death & Differentiation*, 15(1), pp. 171–182. doi: 10.1038/sj.cdd.4402233.

Choi, J. and Sun, N. (2011) 'Nanoparticles in Biomedical Applications and Their Safety Concerns', in *Biomedical Engineering - From Theory to Applications*. InTech. doi: 10.5772/18452.

Clarkson, P. M. and Rawson, E. S. (1999) 'Nutritional Supplements to Increase Muscle Mass', *Critical Reviews in Food Science and Nutrition*, 39(4), pp. 317–328. doi: 10.1080/10408699991279196.

Coleman, M. L. *et al.* (2001) 'Membrane blebbing during apoptosis results from caspase-mediated activation of ROCK I', *Nature Cell Biology*, 3(4), pp. 339–345. doi: 10.1038/35070009.

Costa, M. (1997) 'Toxicity and Carcinogenicity of Cr(VI) in Animal Models and Humans', *Critical Reviews in Toxicology*, 27(5), pp. 431–442. doi: 10.3109/10408449709078442.

Crans, D. C. (2015) 'Antidiabetic, Chemical, and Physical Properties of Organic Vanadates as Presumed Transition-State Inhibitors for Phosphatases', *The Journal of Organic Chemistry*, 80(24), pp. 11899–11915. doi: 10.1021/acs.joc.5b02229.

Das, M. *et al.* (2007) 'Auto-catalytic ceria nanoparticles offer neuroprotection to adult rat spinal cord neurons', *Biomaterials*, 28(10), pp. 1918–1925. doi: 10.1016/j.biomaterials.2006.11.036.

Denecker, G. *et al.* (2000) 'Phosphatidyl serine exposure during apoptosis precedes release of cytochrome c and decrease in mitochondrial transmembrane potential', *FEBS Letters*, 465(1), pp. 47–52. doi: 10.1016/S0014-5793(99)01702-0.

Dias, C. R., Portela, M. F. and Bond, G. C. (1997) 'Synthesis of Phthalic Anhydride: Catalysts, Kinetics, and Reaction Modeling', *Catalysis Reviews*, 39(3), pp. 169–207. doi: 10.1080/01614949709353776.

Dizaj, S. M. *et al.* (2014) 'Antimicrobial activity of the metals and metal oxide nanoparticles', *Materials Science and Engineering: C*, 44, pp. 278–284. doi: 10.1016/j.msec.2014.08.031.

Doshi, N. and Mitragotri, S. (2010) 'Needle-shaped polymeric particles induce transient disruption of cell membranes', *Journal of The Royal Society Interface*, 7(suppl_4). doi: 10.1098/rsif.2010.0134.focus.

Ďuračková, Z. and Gvozdjáková, A. (2008) 'Oxidants, Antioxidants and Oxidative Stress', in *Mitochondrial Medicine*. Dordrecht: Springer Netherlands, pp. 19–54. doi: 10.1007/978-1-4020-6714-3_2.

Ehring, G. R. *et al.* (2000) 'Vanadate Induces Calcium Signaling, Ca2+ Release-Activated Ca2+ Channel Activation, and Gene Expression in T Lymphocytes and RBL-2H3 Mast Cells Via Thiol Oxidation', *The Journal of Immunology*, 164(2), pp. 679–687. doi: 10.4049/jimmunol.164.2.679.

Evan, G. I. and Vousden, K. H. (2001) 'Proliferation, cell cycle and apoptosis in cancer', *Nature*, 411(6835), pp. 342–348. doi: 10.1038/35077213.

Evangelou, A. M. (2002) 'Vanadium in cancer treatment', *Critical Reviews in Oncology/Hematology*, 42(3), pp. 249–265. doi: 10.1016/S1040-8428(01)00221-9.

Exbrayat, J. M., Moudilou, E. N. and Lapied, E. (2015) 'Harmful Effects of Nanoparticles on Animals', *Journal of Nanotechnology*. doi: 10.1155/2015/861092.

Fatahian-Dehkordi, R. A. *et al.* (2017) 'Serum biochemical status and morphological changes in mice ovary associated with copper oxide nanoparticles after thiamine therapy', *Journal of HerbMed Pharmacology*, 6(1), pp. 21–26.

Feng, C. Q. *et al.* (2008) 'Synthesis of spherical porous vanadium pentoxide and its electrochemical properties', *Journal of Power Sources*, 184(2), pp. 485–488. doi: 10.1016/j.jpowsour.2008.04.049.

Fouani, L. *et al.* (2017) 'Metals and metastasis: Exploiting the role of metals in cancer metastasis to develop novel anti-metastatic agents', *Pharmacological Research*. Elsevier Ltd, 115, pp. 275–287. doi: 10.1016/j.phrs.2016.12.001.

Franken, N. A. P. *et al.* (2006) 'Clonogenic assay of cells in vitro', *Nature*

*Protocols*. doi: 10.1038/nprot.2006.339.

French, R. J. and Jones, P. J. H. (1993) ‘Role of vanadium in nutrition: Metabolism, essentiality and dietary considerations’, *Life Sciences*, 52(4), pp. 339–346. doi: 10.1016/0024-3205(93)90146-T.

Fumagalli, C. *et al.* (1994) ‘Production of Maleic and Phthalic Anhydrides by Selective Vapor Phase Oxidation with Vanadium Oxide Based Catalysts’, in *Studies in Surface Science and Catalysis*, pp. 221–231. doi: 10.1016/S0167-2991(08)63414

Geng, Y. *et al.* (2007) ‘Shape effects of filaments versus spherical particles in flow and drug delivery’, *Nature Nanotechnology*, 2(4), pp. 249–255. doi: 10.1038/nnano.2007.70.

Ghosh, S. *et al.* (2018) ‘Nanoisozymes: Crystal-Facet-Dependent Enzyme-Mimetic Activity of V 2 O 5 Nanomaterials’, *Angewandte Chemie International Edition*, 57(17), pp. 4510–4515. doi: 10.1002/anie.201800681.

Gimeno, M. P. *et al.* (2008) ‘Selective oxidation of o-xylene to phthalic anhydride over V2O5/TiO2: Kinetic study in a fluidized bed reactor’, *Chemical Engineering and Processing: Process Intensification*, 47(9–10), pp. 1844–1852. doi: 10.1016/j.cep.2007.10.010.

Golchin, J. *et al.* (2017) ‘Nanozyme applications in biology and medicine: an overview’, *Artificial Cells, Nanomedicine, and Biotechnology*, 45(6), pp. 1069–1076. doi: 10.1080/21691401.2017.1313268.

Hansen, T. V., Aaseth, J. and Alexander, J. (1982) ‘The effect of chelating agents on vanadium distribution in the rat body and on uptake by human erythrocytes’, *Archiv für Toxikologie*, 50(3–4), pp. 195–202. doi: 10.1007/BF00310851.

Hao, Q. *et al.* (2018) ‘VO 2 /TiN Plasmonic Thermochromic Smart Coatings for Room-Temperature Applications’, *Advanced Materials*. doi: 10.1002/adma.201705421.

Hryha, E., Rutqvist, E. and Nyborg, L. (2012) ‘Stoichiometric vanadium oxides studied by XPS’, *Surface and Interface Analysis*, 44(8), pp. 1022–1025. doi:

10.1002/sia.3844.

Huang, D., Zhou, H. and Gao, J. (2015) 'Nanoparticles modulate autophagic effect in a dispersity-dependent manner', *Scientific Reports*. Nature Publishing Group, 5(1), p. 14361. doi: 10.1038/srep14361.

Huang, X. *et al.* (2006) 'Cancer Cell Imaging and Photothermal Therapy in the Near-Infrared Region by Using Gold Nanorods', *Jacs*, 128(3), pp. 2115–2120. doi: 10.1021/ja057254a.

Huo, S. *et al.* (2016) 'Fully Zwitterionic Nanoparticle Antimicrobial Agents through Tuning of Core Size and Ligand Structure', *ACS Nano*, 10(9), pp. 8732–8737. doi: 10.1021/acsnano.6b04207.

Hussain, S. *et al.* (2012) 'Cerium Dioxide Nanoparticles Induce Apoptosis and Autophagy in Human Peripheral Blood Monocytes', *ACS Nano*, 6(7), pp. 5820–5829. doi: 10.1021/nn302235u.

Ingram, J. L. *et al.* (2007) 'Genomic analysis of human lung fibroblasts exposed to vanadium pentoxide to identify candidate genes for occupational bronchitis', *Respiratory Research*, 8(1), p. 34. doi: 10.1186/1465-9921-8-34.

Jang, H., Kang, K. and El-Sayed, M. A. (2018) 'Real-time tracking of the autophagy process in living cells using plasmonically enhanced Raman spectroscopy of fucoidan-coated gold nanoparticles', *Journal of Materials Chemistry B*, 6(34), pp. 5460–5465. doi: 10.1039/C8TB01402G.

Jin, A. *et al.* (2008) 'Electrical and electrochemical characterization of poly (ethylene oxide)/V2O5 xerogel electrochromic films', *Solid State Ionics*, 179(21–26), pp. 1256–1262. doi: 10.1016/j.ssi.2008.01.019.

Johansson, A.-C. *et al.* (2010) 'Regulation of apoptosis-associated lysosomal membrane permeabilization', *Apoptosis*, 15(5), pp. 527–540. doi: 10.1007/s10495-009-0452-5.

Joseph, J. *et al.* (2011) 'High Throughput Ratio Imaging to Profile Caspase Activity: Potential Application in Multiparameter High Content Apoptosis Analysis and Drug Screening', *PLoS ONE*. Edited by J. A. Bauer, 6(5), p. e20114. doi: 10.1371/journal.pone.0020114.

Kalyanaraman, B. *et al.* (2012) 'Measuring reactive oxygen and nitrogen species with fluorescent probes: challenges and limitations', *Free Radical Biology and Medicine*, 52(1), pp. 1–6. doi: 10.1016/j.freeradbiomed.2011.09.030.

Kawabe, K. *et al.* (2006) 'Possible mode of action for insulinomimetic activity of vanadyl(IV) compounds in adipocytes', *Life Sciences*, 78(24), pp. 2860–2866. doi: 10.1016/j.lfs.2005.11.008.

Keuleers, R. *et al.* (1999) 'Vibrational Analysis of Urea', *The Journal of Physical Chemistry A*, 103(24), pp. 4621–4630. doi: 10.1021/jp984180z.

Klionsky, D. J. *et al.* (2016) 'Guidelines for the use and interpretation of assays for monitoring autophagy (3rd edition)', *Autophagy*, 12(1), pp. 1–222. doi: 10.1080/15548627.2015.1100356.

Korbecki, J. *et al.* (2012) 'Biochemical and medical importance of vanadium compounds.', *Acta biochimica Polonica*, 59(2), pp. 195–200. Available at: http://www.ncbi.nlm.nih.gov/pubmed/22693688.

Koyuturk, M. *et al.* (2005) 'Effects of Vanadyl Sulfate on Liver of Streptozotocin-Induced Diabetic Rats', *Biological Trace Element Research*, 104(3), pp. 233–248. doi: 10.1385/BTER:104:3:233.

Lee, W. C. *et al.* (2011) 'Origin of Enhanced Stem Cell Growth and Differentiation on Graphene and Graphene Oxide', *ACS Nano*, 5(9), pp. 7334–7341. doi: 10.1021/nn202190c.

Li, G. *et al.* (2009) 'One-Dimensional V 2 O 5 @Polyaniline Core/Shell Nanobelts Synthesized by an In situ Polymerization Method', *Macromolecular Rapid Communications*, 30(21), pp. 1841–1845. doi: 10.1002/marc.200900322.

Li, X. (2012) 'Improved Pyrogallol Autoxidation Method: A Reliable and Cheap Superoxide-Scavenging Assay Suitable for All Antioxidants', *Journal of Agricultural and Food Chemistry*, 60(25), pp. 6418–6424. doi: 10.1021/jf204970r.

Lin, Y. *et al.* (2017) ‘An in Situ Intracellular Self-Assembly Strategy for Quantitatively and Temporally Monitoring Autophagy’. doi: 10.1021/acsnano.6b07843.

Liu, J. *et al.* (2005) ‘Vanadium Pentoxide Nanobelts: Highly Selective and Stable Ethanol Sensor Materials’, *Advanced Materials*, 17(6), pp. 764–767. doi: 10.1002/adma.200400993.

Liu, X. *et al.* (2016) ‘Stereoisomers of Astaxanthin Inhibit Human Colon Cancer Cell Growth by Inducing G2/M Cell Cycle Arrest and Apoptosis’, *Journal of Agricultural and Food Chemistry*, 64(41), pp. 7750–7759. doi: 10.1021/acs.jafc.6b03636.

Liu, X. *et al.* (2018) ‘V 2 O 5 -Based nanomaterials: synthesis and their applications’, *RSC Advances*. Royal Society of Chemistry, 8(8), pp. 4014–4031. doi: 10.1039/C7RA12523B.

Livage, J. (2010) ‘Hydrothermal Synthesis of Nanostructured Vanadium Oxides’, *Materials*, 3(8), pp. 4175–4195. doi: 10.3390/ma3084175.

Luzio, J. P. *et al.* (2014) ‘The Biogenesis of Lysosomes and Lysosome-Related Organelles’, *Cold Spring Harbor Perspectives in Biology*, 6(9), pp. a016840–a016840. doi: 10.1101/cshperspect.a016840.

Manke, A., Wang, L. and Rojanasakul, Y. (2013) ‘Mechanisms of Nanoparticle-Induced Oxidative Stress and Toxicity’, *BioMed Research International*, 2013(1), pp. 1–15. doi: 10.1155/2013/942916.

Mao, C. *et al.* (2006) ‘Sonochemical Route for Self-Assembled V 2 O 5 Bundles with Spindle-like Morphology and Their Novel Application in Serum Albumin Sensing’, *The Journal of Physical Chemistry B*, 110(30), pp. 14709–14713. doi: 10.1021/jp061809m.

Marklund, S. and Marklund, G. (1974) ‘Involvement of the Superoxide Anion Radical in the Autoxidation of Pyrogallol and a Convenient Assay for Superoxide Dismutase’, 474, pp. 469–474.

Mindell, J. A. (2012) ‘Lysosomal Acidification Mechanisms’, *Annual Review of Physiology*, 74(1), pp. 69–86. doi: 10.1146/annurev-physiol-012110-142317.

Moghimi, S. M., Hunter, A. C. and Murray, J. C. (2005) ‘Nanomedicine: current status and future prospects’, *The FASEB Journal*, 19(3), pp. 311–330. doi: 10.1096/fj.04-2747rev.

Mu, H. *et al.* (2016) ‘Potent Antibacterial Nanoparticles against Biofilm and Intracellular Bacteria’, *Scientific Reports*. Nature Publishing Group, 6(1), p. 18877. doi: 10.1038/srep18877.

Mukherjee, B. *et al.* (2004) ‘Vanadium—an element of atypical biological significance’, *Toxicology Letters*, 150(2), pp. 135–143. doi: 10.1016/j.toxlet.2004.01.009.

Nair, L. V *et al.* (2017) ‘Blood brain barrier permeable gold nanocluster for targeted brain imaging and therapy: an in vitro and in vivo study’, *Journal of Materials Chemistry B*. Royal Society of Chemistry, 5(42), pp. 8314–8321. doi: 10.1039/C7TB02247F.

Natalio, F. *et al.* (2012) ‘Vanadium pentoxide nanoparticles mimic vanadium haloperoxidases and thwart biofilm formation’, *Nature Nanotechnology*, 7(8), pp. 530–535. doi: 10.1038/nnano.2012.91.

Nimi, N. *et al.* (2018) ‘Multifunctional hybrid nanoconstruct of zerovalent iron and carbon dots for magnetic resonance angiography and optical imaging: An In vivo study’, *Biomaterials*, 171, pp. 46–56. doi: 10.1016/j.biomaterials.2018.04.012.

Ojea-Jiménez, I. *et al.* (2016) ‘Highly Flexible Platform for Tuning Surface Properties of Silica Nanoparticles and Monitoring Their Biological Interaction’, *ACS Applied Materials & Interfaces*, 8(7), pp. 4838–4850. doi: 10.1021/acsami.5b11216.

Osmolovskaya, O. M. *et al.* (2014) ‘Synthesis of vanadium dioxide thin films and nanopowders: A brief review’, *Reviews on Advanced Materials Science*, 36(1), pp. 70–74.

Pellegrin, S. and Mellor, H. (2007) ‘Actin stress fibres’, *Journal of Cell*

*Science*, 120(20), pp. 3491–3499. doi: 10.1242/jcs.018473.

Pereira, M. J. *et al.* (2009) ‘Effects of decavanadate and insulin enhancing vanadium compounds on glucose uptake in isolated rat adipocytes’, *Journal of Inorganic Biochemistry*, 103(12), pp. 1687–1692. doi: 10.1016/j.jinorgbio.2009.09.015.

Pessoa, J. C., Etcheverry, S. and Gambino, D. (2015) ‘Vanadium compounds in medicine’, *Coordination Chemistry Reviews*. Elsevier B.V., 301–302, pp. 24–48. doi: 10.1016/j.ccr.2014.12.002.

Pillai, S. I., Subramanian, S. P. and Kandaswamy, M. (2014) ‘Antidyslipidemic effect of a novel vanadium-3-hydroxy flavone complex in streptozotocin-induced experimental diabetes in rats’, *Biomedicine and Preventive Nutrition*. doi: 10.1016/j.bionut.2013.04.004.

Pinna, N. *et al.* (2003) ‘Local Structure of Nanoscopic Materials: V 2 O 5 Nanorods and Nanowires’, *Nano Letters*, 3(8), pp. 1131–1134. doi: 10.1021/nl034326s.

Prześniak-Welenc, M. *et al.* (2015) ‘The Influence of Thermal Conditions on V 2 O 5 Nanostructures Prepared by Sol-Gel Method’, *Journal of Nanomaterials*, 2015, pp. 1–8. doi: 10.1155/2015/418024.

Rainbolt, T. K. *et al.* (2013) ‘Stress-Regulated Translational Attenuation Adapts Mitochondrial Protein Import through Tim17A Degradation’, *Cell Metabolism*, 18(6), pp. 908–919. doi: 10.1016/j.cmet.2013.11.006.

Ray, R. S. *et al.* (2007) ‘Suppression of cell proliferation, induction of apoptosis and cell cycle arrest: Chemopreventive activity of vanadiumin vivo andin vitro’, *International Journal of Cancer*, 120(1), pp. 13–23. doi: 10.1002/ijc.22277.

Reddy, C. V. S. *et al.* (2008) ‘Simple Preparation of V 2 O 5 Nanostructures and Their Characterization’, *Bulletin of Korean Chemical Society*, 29(10), pp. 2061–2064. doi: 10.1016/j.jpowsour.2007.06.166.

Rehder, D. (2012) ‘The potentiality of vanadium in medicinal applications’, *Future Medicinal Chemistry*, 4(14), pp. 1823–1837. doi: 10.4155/fmc.12.103.

Riedl, S. J. and Shi, Y. (2004) ‘Molecular mechanisms of caspase regulation during apoptosis’, *Nature Reviews Molecular Cell Biology*, 5(11), pp. 897–907. doi: 10.1038/nrm1496.

Rojas, E. *et al.* (1999) ‘Are metals dietary carcinogens?’, *Mutation Research/Genetic Toxicology and Environmental Mutagenesis*, 443(1–2), pp. 157–181. doi: 10.1016/S1383-5742(99)00018-6.

Romero, G. *et al.* (2011) ‘Spontaneous confocal Raman microscopy--a tool to study the uptake of nanoparticles and carbon nanotubes into cells’, *Nanoscale Research Letters*, 6(1), p. 429. doi: 10.1186/1556-276X-6-429.

Saraswathy, A. *et al.* (2014) ‘Citrate coated iron oxide nanoparticles with enhanced relaxivity for in vivo magnetic resonance imaging of liver fibrosis’, *Colloids and Surfaces B: Biointerfaces*. Elsevier B.V., 117, pp. 216–224. doi: 10.1016/j.colsurfb.2014.02.034.

Scior, T. *et al.* (2010) ‘Chimeric design, synthesis, and biological assays of a new nonpeptide insulin-mimetic vanadium compound to inhibit protein tyrosine phosphatase 1B’, *Drug Design, Development and Therapy*, 4, pp. 231–242. doi: 10.2147/DDDT.S8445.

Serrano-Puebla, A. and Boya, P. (2016) ‘Lysosomal membrane permeabilization in cell death: new evidence and implications for health and disease’, *Annals of the New York Academy of Sciences*, 1371(1), pp. 30–44. doi: 10.1111/nyas.12966.

Sharma, N. *et al.* (2010) ‘Synthesis, characterization, and antibacterial activity of vanadium(IV) complexes of hydroxamic acids’, *Journal of Coordination Chemistry*, 63(1), pp. 176–184. doi: 10.1080/00958970903247712.

Singh, R. *et al.* (2015) ‘Differential cytotoxic and radiosensitizing effects of silver nanoparticles on triple-negative breast cancer and non-triple-negative breast cells’, *International Journal of Nanomedicine*, 10, p. 3937. doi: 10.2147/IJN.S80349.

Slavin, Y. N. *et al.* (2017) ‘Metal nanoparticles: understanding the mechanisms behind antibacterial activity’, *Journal of Nanobiotechnology*. BioMed Central, 15(1), p. 65. doi: 10.1186/s12951-017-0308-z.

Slomberg, D. L. *et al.* (2013) ‘Role of Size and Shape on Biofilm Eradication for Nitric Oxide-Releasing Silica Nanoparticles’, *ACS Applied Materials & Interfaces*, 5(19), pp. 9322–9329. doi: 10.1021/am402618w.

Smulders, S. *et al.* (2012) ‘Contamination of nanoparticles by endotoxin: Evaluation of different test methods’, *Particle and Fibre Toxicology*. doi: 10.1186/1743-8977-9-41.

Song, N. *et al.* (2006) ‘Oxidation of Butane to Maleic Anhydride using Vanadium Phosphate Catalysts: Comparison of Operation in Aerobic and Anaerobic Conditions using a Gas-gas Periodic Flow Reactor’, *Catalysis Letters*, 106(3–4), pp. 127–131. doi: 10.1007/s10562-005-9619-z.

Song, W. *et al.* (2015) ‘The autophagic response to polystyrene nanoparticles is mediated by transcription factor EB and depends on surface charge’, *Journal of Nanobiotechnology*. BioMed Central, 13(1), p. 87. doi: 10.1186/s12951-015-0149-6.

Stern, S. T., Adiseshaiah, P. P. and Crist, R. M. (2012) ‘Autophagy and lysosomal dysfunction as emerging mechanisms of nanomaterial toxicity’, *Particle and Fibre Toxicology*, 9(1), p. 20. doi: 10.1186/1743-8977-9-20.

Subba Reddy, C. V. *et al.* (2008) ‘Hydrothermal synthesis of hydrated vanadium oxide nanobelts using poly (ethylene oxide) as a template’, *Journal of Power Sources*, 179(2), pp. 854–857. doi: 10.1016/j.jpowsour.2008.01.014.

Šurca, A. and Orel, B. (1999) ‘IR spectroscopy of crystalline V2O5 films in different stages of lithiation’, *Electrochimica Acta*, 44(18), pp. 3051–3057. doi: 10.1016/S0013-4686(99)00019-5.

Susin, S. A. *et al.* (2000) ‘Two distinct pathways leading to nuclear apoptosis’, *Journal of Experimental Medicine*. doi: 10.1084/jem.192.4.571.

Takemoto, K. *et al.* (2003) ‘Spatio-temporal activation of caspase revealed by indicator that is insensitive to environmental effects’, *Journal of Cell Biology*. doi: 10.1083/jcb.200207111.

Tang, L. *et al.* (2012) ‘Urinary Titanium and Vanadium and Breast Cancer: A Case-Control Study’, *Nutrition and Cancer*, 64(3), pp. 368–376. doi: 10.1080/01635581.2012.654586.

Vance, M. E. *et al.* (2015) ‘Nanotechnology in the real world: Redeveloping the nanomaterial consumer products inventory’, *Beilstein Journal of Nanotechnology*. doi: 10.3762/bjnano.6.181.

Venkatesan, A. *et al.* (2013) ‘Structural, morphological and optical properties of highly monodispersed PEG capped V2O5 nanoparticles synthesized through a non-aqueous route’, *Materials Letters*. Elsevier, 91, pp. 228–231. doi: 10.1016/j.matlet.2012.09.117.

Vu, T. D. *et al.* (2019) ‘Physical vapour deposition of vanadium dioxide for thermochromic smart window applications’, *Journal of Materials Chemistry C*. Royal Society of Chemistry, 7(8), pp. 2121–2145. doi: 10.1039/C8TC05014G.

Wagner, V. *et al.* (2006) ‘The emerging nanomedicine landscape’, *Nature Biotechnology*, 24(10), pp. 1211–1217. doi: 10.1038/nbt1006-1211.

Wan, J. *et al.* (2015) ‘Surface chemistry but not aspect ratio mediates the biological toxicity of gold nanorods in vitro and in vivo’, *Scientific Reports*. Nature Publishing Group, 5(1), p. 11398. doi: 10.1038/srep11398.

Wang, Z. *et al.* (2016) ‘Biological and environmental interactions of emerging two-dimensional nanomaterials’, *Chemical Society Reviews*, 45(6), pp. 1750–1780. doi: 10.1039/C5CS00914F.

Xiao, N., Wang, C. and Yu, C. (2013) ‘A Self-referencing detection of microorganisms using surface enhanced Raman scattering nanoprobes in a test-in-a-tube platform’, *Biosensors*, 3(3), pp. 312–326. doi: 10.3390/bios3030312.

Yang, H. *et al.* (2016) ‘Mechanism for the Cellular Uptake of Targeted Gold Nanorods of Defined Aspect Ratios’, *Small*, 12(37), pp. 5178–5189. doi:

10.1002/smll.201601483.

Yang, X. *et al.* (2014) ‘Hepatic toxicity biomarkers’, in *Biomarkers in Toxicology*. doi: 10.1016/B978-0-12-404630-6.00013-0.

Yang, Y. *et al.* (2017) ‘Toxicity assessment of nanoparticles in various systems and organs’, *Nanotechnology Reviews*. doi: 10.1515/ntrev-2016-0047.

Ye, J. *et al.* (1999) ‘Induction of TNFα in macrophages by vanadate is dependent on activation of transcription factor NF-κB and free radical reactions’, *Molecular and Cellular Biochemistry*. doi: https://doi.org/10.1023/a:1006969008056.

Yildirimer, L. *et al.* (2011) ‘Toxicology and clinical potential of nanoparticles’, *Nano Today*, 6(6), pp. 585–607. doi: 10.1016/j.nantod.2011.10.001.

Yokota, J. (2000) ‘Tumor progression and metastasis’, *Carcinogenesis*, 21(3), pp. 497–503. doi: 10.1093/carcin/21.3.497.

Zhai, T. *et al.* (2010) ‘Centimeter-Long V2O5 Nanowires: From Synthesis to Field-Emission, Electrochemical, Electrical Transport, and Photoconductive Properties’, *Advanced Materials*, 22(23), pp. 2547–2552. doi: 10.1002/adma.200903586.

Zheng, X. T. *et al.* (2013) ‘Graphene Quantum Dots as Universal Fluorophores and Their Use in Revealing Regulated Trafficking of Insulin Receptors in Adipocytes’, *ACS Nano*, 7(7), pp. 6278–6286. doi: 10.1021/nn4023137.

Zhou, Y. *et al.* (2007) ‘Preparation and characterization of V2O5 macro-plates’, *Materials Letters*, 61(19–20), pp. 4073–4075. doi: 10.1016/j.matlet.2007.01.022.

Zolata, H., Abbasi Davani, F. and Afarideh, H. (2015) ‘Synthesis, characterization and theranostic evaluation of Indium-111 labeled multifunctional superparamagnetic iron oxide nanoparticles’, *Nuclear Medicine and Biology*. Elsevier Inc., 42(2), pp. 164–170. doi: 10.1016/j.nucmedbio.2014.09.007.

# ANNEXURE

## RESEARCH PUBLICATIONS

1. **Parvathy Radhakrishna Pillai Suma,** Ramapurath S Jayasree *et al*. "Vanadium pentoxide nanoplates: Synthesis, characterization and unveiling the intrinsic anti-bacterial activity". *Materials Letters* (2020): Vol: 269, 127673. **IF: 3.204**
2. **Parvathy Radhakrishna Pillai Suma**, Ramapurath S Jayasree *et al.* "Vanadium pentoxide nanoparticles mediate perturbations in cellular redox balance; the paradigm of metabolic reprograming from autophagy to apoptosis". Revision submitted to the *Journal of Free Radical Biology and Medicine* ( Ref no: FRBM-D-20-00275). **IF: 6.17**
3. Resmi V. Nair, **Parvathy Radhakrishna Pillai Suma**, Ramapurath S Jayasree, "An On-Off Fluorescent Nanosensor for the Simultaneous detection of Copper and Creatinine". *Materials Science & Engineering C* (2020): vol: 109, 110569. **IF: 5.88**
4. Saraswathy Ariya, Nazeer Shaiju S, N Nimi; Santhakumar Hema, **Parvathy Radhakrishna Pillai S** *et al.* "Asialoglycoprotein receptor mediated targeting of a dual function nanoprobe *for in vivo* Magnetic Resonance Imaging and Therapy of liver fibrosis" (submitted to *Colloids and Surfaces B: Biointerfaces*)

## PATENT

Jayasree R S, Resmi V Nair, **Parvathy R.S** - Multi functional fluorescent nanosensor for simultaneous detection of copper and creatinine and the process thereof (**Indian Patent Application** no. 201741031554).

## AWARD

Received the "**Endeavour Research Fellowship award**" – 2015 from the Commonwealth of Australia.

## CONFERENCES

1. **Parvathy.R. S**, Jayasree R. S. “A study on cellular interactions of Vanadia nanospheres using MDA-MB 231 breast cancer cell line”. The Satellite Meeting to the International Congress of Cell Biology (Cellular Processes in Homeostasis, Regeneration, and Disease), conducted by IISER Trivandrum, Trivandrum, from February 2-3, 2018.
2. **Parvathy.R. S**, Jayasree R. S. “Vanadia nanospheres prevent breast cancer cell growth – study using MDA-MB-231 breast cancer cell line”. The Materials for a Better Tomorrow, International Conference on Advanced Materials (SCICON ’16), Organized by Amrita Vishwa Vidyapeetham, Coimbatore, December 19 - 21, 2016.
3. **Parvathy.R. S**, Jayasree R. S. “Understanding the mechanistic action of Vanadia nanoparticles on MDAMB 231 cancer cell line”. The Fourth International Conference on Frontiers in Nanoscience and Technology (Cochin Nano-2016), Cochin University, Ernakulam from February 20 - 23, 2016.
4. **Parvathy.R. S**, Jayasree R. S “Grabbing Cancer control using a versatile nanoparticle Approach.” The Indo-Australian Conference on Biomaterials, Tissue Engineering, Drug Delivery System & Regenerative Medicine (BiTERM 2015), Chennai, from February 5-7, 2015.